Mathematical Modelling of Cellular Rearrangements during Embryonic Development

Khoren Ponsin, Department of Mathematics and Statistics
McGill University, Montreal
Supervisor: Anmar Khadra
August, 2021

A thesis submitted to McGill University in partial fulfillment of the requirements of the degree of

Master of Science

Abstract

Cell death by apoptosis plays a key role in several developmental processes such as tissue sculpting and homeostasis. During embryonic development of the urogenital system in mice, apoptosis plays a crucial role in removing a temporal structure called the Common Nephric Duct (CND), a necessary step to connect the ureter to the bladder epithelium. Evidence suggests that apoptotic cell removal generates pulling forces necessary for tissue rearrangement. Non-professional phagocytosis of apoptotic cells by neighbouring epithelial cells (referred to as non-professional efferocytosis) was observed during CND elimination. In this process, epithelial cells programmed to die are engulfed and subsequently phagocytosed by neighboring cells. This entire process involves five different stages of apoptosis, a cell drift and an apoptotic gradient along the CND. We develop a novel multiscale mathematical model that couples the different stages of efferocytosis and the cell types involved (e.g., apoptotic, phagocyte and engulfed) with the cellular drift equation system (advection) equation to provide spatiotemporal insights about this process. We use the apoptotic gradient along the CND, the stationary distribution of cells in the different stages and the maintenance of a uniform diameter of the duct to parameterize the model. Using experimental data and boundary conditions, we adapt the model to different physiological conditions, including in vivo wild types, ex vivo non-treated embryos and ex vivo treated embryos. The mathematical model is then employed to perform tasks that are difficult or not possible to be conducted experimentally. With this approach, we quantify the dwell time at each stage of efferocytosis and dissect the relative contribution of efferocytosis, cell extrusion and proliferation individually and in combination to CND shortening/elongation continuously over time. We finally examine the effects of Blebbistatin treatment on CND dynamics and determine the role of

actomyosin during CND elimination. Our results suggest that there is significant CND shortening forces in the absence of actomyosin activity, an interesting outcome of this modeling study in view of the generally recognized belief that morphogenetic forces are largely driven primarily by actomyosin activity. Indeed, this work provides an evidence that efferocytosis and actomyosin drive the CND elimination throughout time (i.e., not only at certain time points). It also provides a mathematical spatiotemporal framework for how cellular rearrangement could occur during embryonic development in the CND.

Abstract

La mort cellulaire programmée (apoptose) est essentielle dans plusieurs processus de développement tel que le remodelage de tissue et l'homéostasie. Pendant le développement embryonnaire du système urogénital de la souris, l'apoptose joue un rôle crucial dans l'élimination d'une structure temporaire nommée le Canal Mésonéphrique Commun (CMC), une étape nécessaire afin de connecter l'uretère à l'épithélium de la vessie. Plusieurs données suggèrent que l'apoptose génère des forces de traction nécessaires aux réarrangements de tissues. L'efferocytose par des cellules épithéliales (aussi surnommée la phagocytose non-professionnelle) a été osbervée pendant l'élimination du CMC. Durant ce processus, les cellules épithéliales programmées à mourir sont phagocytées et digérées par des cellules voisines. Ce processus au complet implique cinq étapes d'apoptose, un flux cellulaire et un gradient apoptotique le long du CMC. Nous developpons un nouveau modèle à multi-échelles qui associe les différentes étapes de l'efferocytose et les types de cellule impliqués (e.g. apoptotique, phagocyte et phagocytée) à un système d'équations de flux cellulaire (advection) afin de fournir des renseignements spatiotemporels concernant ce processus. Nous utilisons le gradient apoptotique le long du CMC, la distribution stationnaire des cellules dans les différentes étapes de l'efferocytose et la maintenance d'un diamètre constant du conduit pour paramétrer le modèle. En utilisant des données expérimentales et des conditions limites, nous adaptons le modèle à plusieurs conditions physiologiques, incluant des types sauvages in vivo, des embryos non-traités ex vivo et des embryos traités ex vivo. Le modèle mathématique est ensuite utilisé pour effectuer des tâches qui sont difficiles ou même impossible à faire expérimentalement. Avec cette approche, nous quantifions la durée de chaque étape de l'efferocytose et décortiquons la contribution de l'efferocytose, l'extrusion cellulaire et la

prolifération cellulaire individuellement et en combinaison dans le racourcissement/élongation du CMC au fil du temps. Finalement, nous examinons les effets d'un traitement Blebbistatin sur la dynamique du CMC et déterminons le rôle de l'actomyosine durant l'élimination du CMC. Nos résultats suggèrent qu'il y a un raccourcissement important malgré l'absence d'actomyosine, une conclusion intéressante de cette étude en vue de l'idée généralement reconnue que les forces morphogéniques sont majoritairement guidées principalement par l'activité de l'actomyosine. En effet, ce travail témoigne que l'efferocytose et l'actomyosine guident l'élimination du CND au fil du temps. Cela fournit également un potentiel cadre mathématique spatiotemporel de réarrangement cellulaire pendant le développement embryonnaire du CND.

Acknowledgements

I would like to thank first and foremost my supervisor Prof. Anmar Khadra for his guidance and commitment throughout my undergraduate studies and my masters, his confidence in my work, being a great mentor and introducing me passionately to the field of mathematical biology. I would also like to thank warmly our collaborators Prof. Maxime Bouchard and his PhD-candidate Emily Tang who provided the experimental data, initiated this project and with whom we have been working closely.

Moreover, I would like to thank all the members of the Khadra Lab for the insightful and useful discussions that were held during our lab meetings and even outside of them. Especially, I am very grateful to Dr. Laurent Mackay who helped me greatly when I joined the Khadra Lab and provided some key ideas and equations on which the mathematical model of this project is based.

I would like to thank my parents Myriam and Camille, for their unconditional and loving support, through every project I have undertaken. I would also like to express my gratitude to my brother Tigrane, for his everlasting complicity, and my grandparents for their support and faith in me. To Cecilia, for her invaluable company throughout my journey at McGill University and Montreal, and to my friends for their encouragement.

Finally, I would like to thank the Department of Mathematics and Statistics at McGill, the Natural Sciences and Engineering Research Council and the Center for Applied Mathematics in Bioscience and Medicine for providing the financial support that made the completion of this project possible.

Table of Contents

List of Figures

Nomenclature

Markov models for efferocytosis

$K_A(x,t)$	rate of efferocytosis at location x and time t	*days*$^{-1}$
K_{EI}	transition rate from early internalization to late internalization	*days*$^{-1}$
K_{LI}	transition rate from late internalization to debris	*days*$^{-1}$
K_G	rate of degradation	*days*$^{-1}$
K_D	rate of digestion	*days*$^{-1}$
c	slope of K_A with respect to space scaled by $-L^{-1}$	*days*$^{-1}$
d	y-intercept of K_A with respect to space	*days*$^{-1}$

Multistate Model of Cellular Interactions

N	volume fraction occupied by normal cells	*unitless*
P	volume fraction occupied by Phagocytes	*unitless*
$K_P(x,t)$	rate at which normal cells are turned into Phagocytes at location x and time t	*days*$^{-1}$
K_S	rate of proliferation	*days*$^{-1}$
$K_{BX}(x,t)$	rate of basal extrusion at location x and time t	*days*$^{-1}$
f_n	fraction of cells not undergoing proliferation	*unitless*
f_s	fraction of cell volume conserved after water release during apoptosis	*unitless*

Fluid Dynamics model for Cellular Drifting

$\rho_N(x,t)$	density of volume fraction of Normal cells at location x and time t	μm^{-1}
$\rho_P(x,t)$	density of volume fraction of Phagocytes at location x and time t	μm^{-1}
$\rho_A(x,t)$	density of volume fraction of Apoptotic cell bodies being extruded at location x and time t	μm^{-1}
$L(t)$	length of the CND at time t	μm

$v(x,t)$	cellular drifting velocity at location x and time t	$\mu m/days$

From experimental data to cell densities

g_R	apoptotic gradient value at the rostral end of the CND	*unitless*
g_C	apoptotic gradient value at the caudal end of the CND	*unitless*
p_i	percentage of cell in state i=A,E,EI,LI,D,N or P	*unitless*
v_i	volume fraction occupied by cells in state i=A,E,N or P	*unitless*
a	slope of $\frac{\rho_N}{\rho_T}$ with respect to space scaled by $-L^{-1}$	*unitless*
b	y-intercept of $\frac{\rho_N}{\rho_T}$ with respect to space	*unitless*
g	slope of $\frac{\rho_P}{\rho_T}$ with respect to space scaled by $-L^{-1}$	*unitless*
g	y-intercept of $\frac{\rho_P}{\rho_T}$ with respect to space	*unitless*

Blebbistatin model

K_{AX}	rate of apical extrusion	*days*$^{-1}$
f_{ax}	fraction of cells not being extruded on the apical side	*unitless*
d_i	experimentally measured Blebbistatin treated CND length at time t_i	*unitless*
c_i	predicted CND length at time t_{i+1} using Control model	*unitless*
p_i	elongation percentage caused by Blebbistatin between t_i and t_{i-1}	*unitless*
R_C	Control CND radius	*µm*
R_B	CND radius after 48 hours of Blebbistatin treatment	*µm*
r_C	Control lumen radius	*µm*
r_B	lumen radius after 48 hours of Blebbistatin treatment	*µm*
R_i	CND radius between t_i and t_{i+1}	*µm*
α	ratio of R_B to R_C	*unitless*
α_i	ratio of R_i to R_{i-1}	*unitless*
r_i	lumen radius between t_i and t_{i+1}	*µm*
β	ratio of r_B to r_C	*unitless*
β_i	ratio of r_i to r_{i-1}	*unitless*
γ	ratio of volume of a cell before Blebbistatin treatment to volume of cell after 48 hours of Blebbistatin treatment	*unitless*
γ_i	ratio of volume of a cell at t_i to volume of a cell at t_{i+1}	*unitless*

δ	fraction of cells not undergoing apical extrusion at 48h after the start of Blebbistatin treatment	*unitless*
δ_i	fraction of cells not undergoing apical extrusion at t_i	*unitless*
L_{e_i}	elongated length at t_i	μm
$B(L_{e_i})$	predicted length at t_{i+1} using Blebbi model	μm
ρ_{Ti}	density of the Blebbistatin treated CND between t_{i-1} and t_i	μm^{-1}

PDE model for Blebbistatin

$V(t)$	volume fraction of the CND at time t	*unitless*
$W(t)$	volume of the CND at time t	μm^3
V_0	volume fraction of the CND at time $t = 0$	*unitless*
τ	time constant of the Blebbistatin treatment	day^{-1}
$R_V(t)$	rate of CND volume fraction loss at time t	day^{-1}
$R(t)$	CND radius at time t	μm
$r(t)$	lumen radius at time t	μm
V_{WT1}	WT1 CND volume fraction at $t = 0$	*unitless*
W_{WT1}	WT1 CND volume at $t = 0$	μm^3

Different components of CND elimination

$V_{Tot}(T)$	total volume fraction eliminated between $t = 0$ and $t = T$	*unitless*
$V_i(T)$	volume fraction eliminated between $t = 0$ and $t = T$ through efferocytosis (i=E), basal extrusion (i=BX), apical extrusion (i=AX)	*unitless*
$V_P(T)$	volume fraction added between $t = 0$ and $t = T$ through proliferation	*unitless*
$L_i(t)$	length of the CND at time t when considering only proliferation (P) and apical extrusion(AX) (i=P+AX), proliferation (P), basal extrusion (BX) and efferocytosis(E) (i=P+BX+E)...	μm

Chapter 1

Introduction

1.1 Biological problem

The biological process by which a tissue or organ develops into its final form or shape is known as morphogenesis. Morphogenesis therefore lies at the core of the embryonic development (also named embryogenesis) during which primary layers of cells, called germ layers, are formed [1]. Three germ layers are formed during the embryonic development of vertebrates [2]. Each germ layer eventually develops into specific tissues and organs of the body. Cells derived from the mesoderm (one of the three germ layers) give rise to vital organs such as the heart, the urogenital system and the muscles system [3–5]. A narrow section of the mesoderm, the intermediate mesoderm, develops into the urogenital system which includes the kidney, the bladder, the ureter, the gonads, etc [5]. Development of complex systems, such as the urogenital system, involves the assembly of independently formed organs. In a healthy urogenital system, the ureter conducts urine from the kidney to the the bladder for storage and excretion. At the 11.5 days of embryonic development (denoted E11.5), the ureteric bud (which later develops into the ureter) is inserted into the nephric duct (also called the Wolffian duct), an epithelial structure running through the intermediate mesoderm and connected to the cloaca (the primordium of the bladder and urethra), as shown on Figure 1.1 [7,9]. Before the start of urine production at E15.5, the urinary tract has to become functional, which requires the displacement of the base of the ureteric bud from the nephric duct to the clocoa [9] as shown in the simplified schematic of Figure 1.2. Through this developmental process, the ureter eventually becomes separated from the Wolffian duct and connects the kidney to the bladder.

Using mouse models, studies have been conducted to determine the fate of the region of the Wolffian duct lying between the ureteric bud and the clocoa, called the Common Nephric Duct (CND). In 1975, it was hypothesized that the CND expands and differentiates into the trigone (the muscular region located at the base of the bladder) [6]. This theory was dismissed in [7] using lineage analysis by labeling the CND and its daughter cells: the labeled cells were visible in the CND up to about E13, after which, expression diminished and became undetectable by birth. This indicated that the CND is likely regressing during ureter maturation rather than differentiating into the trigone. In that same study and more recently in other studies [8, 9], it has been shown that the CND undergoes apoptosis, eventually leading to its elimination and subsequently separating the ureter from the Wolffian duct and inserting it into the clocoa (Figures 1.1 and 1.2). In this developmental process, progressive CND shortening depends on regulated cell death elimination that brings the ureteric bud in contact with the bladder epithelium. An irregular apoptosis rate in this system can lead to diseases such as vesicoureteral reflux in the case of excess apoptosis [9], and vesicoureteral junction obstruction in the case of decrease in apoptotic rate [10–15]. Vesicoureteral reflux is the most common urinary tract defect and affects 1-2% of newborns [16]. Such defects are collectively part of Congenital Anomalies of the Kidney and Urinary Tract (CAKUT), a disease group that is the primary cause of chronic kidney disease, urinary tract infection and renal transplant in children [17].

The above studies raise the possibility that the bladder epithelium could be a source of signals inducing programmed cell death in the CND. Programmed cell death is a crucial process during development [20]. Morphogenesis and organ sculpting during embryogenesis rely on successful clearing of apoptotic cells [21]. These processes can be performed by professional Phagocytes (e.g. macrophages) or non-professional Phagocytes (e.g. epithelial cells) [22]. The latter are essential when professional Phagocytes are not abundant

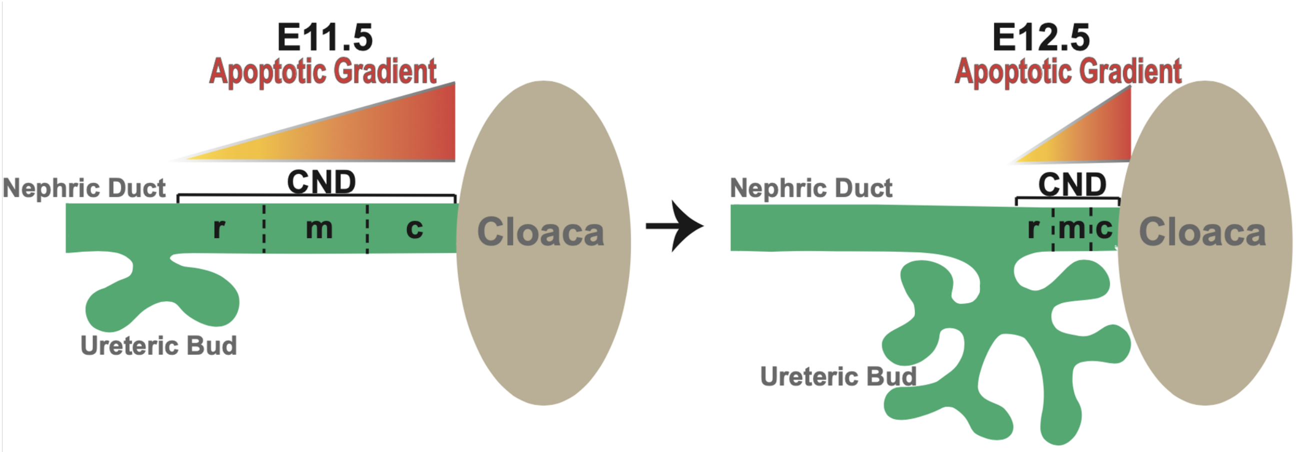

Figure 1.1: During the early stages of development, the Common Nephric Duct (CND) is the region of the Nephric Duct lying between the ureteric bud and the clocoa. The apoptotic gradient along the CND along with the maintenance of a uniform diameter causes the CND to progressively shorten and eventually leads the ureteric bud to be detached from the ND and connected to the clocoa, as depicted on Figure 1.2. This diagram was produced by Emily Tang, PhD candidate in the Bouchard Lab.

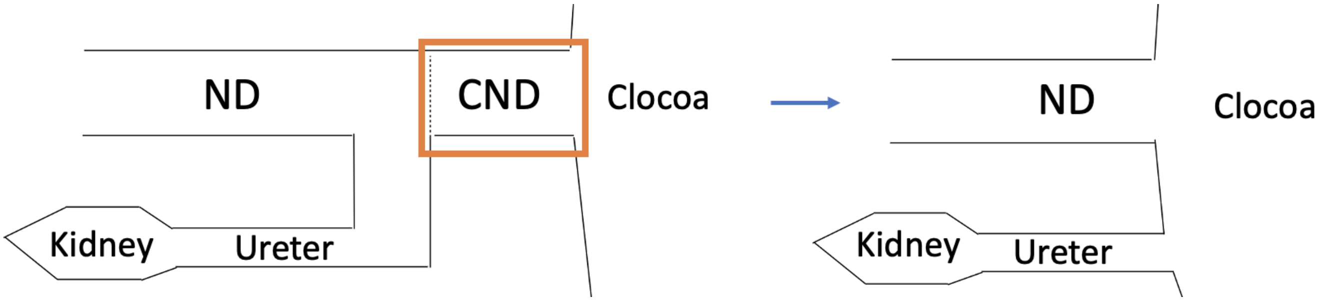

Figure 1.2: "ND" and "CND" stand for Nephric Duct and Common Nephric Duct. The time duration of the process leading to the ureter-bladder connection is around three days, from E11.5 to E14.5.

yet (e.g. during development) or when the site of the apoptosis is inaccessible [21].

Recent observations (unpublished data) made from high resolution confocal imaging in the Bouchard Lab (McGill University) showed that almost all apoptotic cells of the CND are engulfed by neighboring epithelial cells, with very few being extruded out of the CND. This suggests that the main clearance mechanism of the CND elimination is done through non-professional phagocytosis of apoptotic cells by neighbouring epithelial cells, a process referred to as non-professional efferocytosis. This epithelial-cell efferocytosis has been observed in a few other systems such as the lung and adult kidneys, but it occurred only upon injury to maintain tissue homeostasis [18,19]. It has also been observed in mammary glands, with involution after lactation [47]. Even though epithelial-cell efferocytosis occurs in adult systems, none of them are essential for tissue morphogenesis during normal development. In the CND, however, it is essential.

The shortening process of the CND involves a gradient of apoptotic cell death that is highest at the CND-cloaca junction and progressively declines along the CND [9, 10, 12, 13, 16, 31], as shown on Figure 1.1. Based on this data, one can deduce that cell death is not uniform across the CND; indeed, the closer cell nuclei are to the bladder, the more likely these nuclei will be in the apoptotic process. This is what we call the apoptotic gradient [9–11, 31], which plays an important role in cellular rearrangement in the CND. The work conducted in [7] indicates that the shape of the CND at its most caudal region changes in order to insert into the clocoa. This change in shape is even more pronounced around E13.5 when there is not much left of the CND. Unpublished data from the Bouchard Lab (McGill University) indicates, however, that when considering the whole duct at E11.5 and E13.5, the CND maintains its cylindrical with a uniform diameter. Since the CND maintains a uniform diameter along with an apoptotic gradient, we can infer that cells in the CND will gradually drift toward the bladder and cause the CND to shrink in length. Five stages of efferocytosishave been identified by the Bouchard Lab using biomarkers; these include : healthy (or "Normal"), Pre-Engulfed, Early Internalized, Late Internalized and Debris stages, as shown on Figure 1.3. To understand quantitatively the dynamics of the disappearance of the CND, one needs to measure cellular drift toward the bladder caused by the apoptotic gradient and determine the duration of each stage of efferocytosis described above. Due to technical difficulties, it is very hard or even impossible to do so in vivo. In this thesis, we develop a novel multiscale mathematical model, constrained by the unpublished data from the Bouchard lab, to accomplish this task. We estimate dwell time spent in each stage of the non-professional efferocytosis and characterize several spatiotemporal aspects of this system including the rate of efferocytosis and the cellular drift velocity. Moreover, we quantify the contribution of the different processes (proliferation, non-professional efferocyosis, extrusion) in the elimination/elongation of the CND. Even though the biological data provided by the Bouchard Lab suggest that the majority of apoptotic cells are being engulfed by neighboring cells rather than being extruded, we integrate time scales of both events (efferocytosis and extrusion) to determine the overall contribution of each process to the eventual shrinkage of the CND continuously over time.

Tissue morphogenesis is driven in large part by mechanical forces affecting the shape and behavior of individual or groups of cells [23–29]. Those mechanical forces are largely associated with an actin-myosin complex that forms within the cytoskeleton, where the myosin motor protein are able to pull on actin filaments. This property gives rise to contractile fibers that enable cell motility and force generation even in non-muscle cells such as epithelial tissues. However, a category of morphogenetic drivers not primarily based on actomyosin activity, has recently emerged [30]. By constraining our model with data from ex-vivo Blebbistatin (an inhibitor of actomyosin) treated CNDs, we provide further evidence for the presence of significant CND shortening forces in the absence of actomyosin activity. Our work also supports the hypothesis by the Bouchard Lab that apoptosis and efferocytosis drive the morphogenetic movement leading the ureter to connect to the bladder primordium.

1.2 Mathematical models of phagocytosis

We wish to design a mathematical model which describes, on one hand, cellular processes in the CND (efferocytosis and extrusion) and, on the other hand, CND shortening. Previous modelling work of phagocytosis in macrophages already exists in the context of Type 1 diabetes (T1D) [33–35] and using Markov models [48]. In these in vitro studies, the population of macrophages within a cell culture was divided into classes (M_i, $i = 1, \ldots, N$) with each class representing macrohopages that have a specific number of

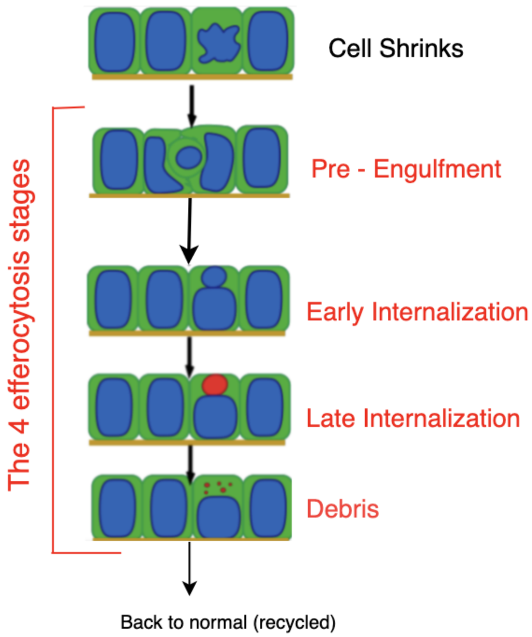

Figure 1.3: The four stages of efferocytosis. The diagram was produced by Emily Tang, PhD candidate in the Bouchard Lab.

apoptotic cells (i) inside them [49]. For example, M_0 represented the class of macrophages with zero apoptotic cells inside them, M_1 represented the class of macrophages with one apoptotic cell inside them and M_i represented the class of macrophages with i apoptotic cells inside them (i was determined experimentally to be at most $N = 7$). Engulfment of apoptotic cells by macrophages was assumed to be an irreversible process and mass action kinetics was used to represent the constant rate of engulfment (denoted by parameter k_e) of this process. Engulfed apoptotic bodies were then assumed to be digested at a roughly constant rate k_d. Since the study focuses on phagocytosis at a time scale of hours, death of macrophages (which happens at a time scale of days) was neglected [49]. In this modeling study, digestion was assumed to be either saturated or unsatured; saturated digestion represented the case when apoptotic cells are digested one at a time by macrophages, while unsaturated digestion represented the case when apoptotic cells are digested simultaneously by macrophages. An example of saturated digestion with N classes of macrophages can be visualized in Figure 1.4. The differential equations model associated with the diagram in Figure 1.4 is thus given by

$$\frac{dM_0}{dt} = -k_e M_0 A + k_d M_1 \tag{1.1}$$

$$\frac{dM_i}{dt} = k_e M_{i-1} A - (k_d + k_e A) M_i + k_d M_{i+1} \tag{1.2}$$

$$\frac{dM_N}{dt} = k_e M_{N-1} A - k_d A M_N, \tag{1.3}$$

where A is the density of the apoptotic cells whose decaying dynamics are described by the following differential equation

$$\frac{dA}{dt} = -k_e \sum_{i=0}^{N-1} M_i. \tag{1.4}$$

Notice how equations (1.1)-(1.3) include the source and sink terms associated with each state of the Markov model in Figure 1.4 (such approach in defining the source and sink terms will be similarly used when developing the multiscale model used in this thesis). The authors in [33] then used the Markov model to compare the values of k_e and k_d between wild-type and T1D-prone animals and thus determine which aspects of macrophage phagocytosis are affected by the disease. Although this model and its variants provided interesting insights about how defects are manifested in macrophage phagocytosis, they only focused on the temporal aspect of this system with no implications on tissue structure as this was not involved.

$$\boldsymbol{M}_0 \underset{k_d}{\overset{k_e}{\rightleftarrows}} \boldsymbol{M}_1 \underset{k_d}{\overset{k_e}{\rightleftarrows}} \boldsymbol{M}_2 \underset{k_d}{\overset{k_e}{\rightleftarrows}} \ldots \underset{k_d}{\overset{k_e}{\rightleftarrows}} \boldsymbol{M}_N$$

Figure 1.4: Kinetic model of saturated macrophage phagocytosis. M_i is the density of macrophages with i engulfed apoptotic cells and N is the maximal macrophage capacity. k_e is the rate at which macrophages engulf apoptotic cells and k_d is the rate at which apoptotic cells are digested. This diagram is taken from [33].

In our system of CND elimination, efferocytosis (i.e. phagocytosis by epithelial cells) takes a central role. The studies of macrophage phagocytosis cited above provided some insights into how to approach this problem using Markov state formalism to describe the different cellular processes involved in efferocytosis. As observed by the Bouchard Lab, the epithelial cells that become non-professional phagocytes can only engulf one apoptotic cell at a time. While this may simplify how to describe efferocytosis mathematically with one step Markov model (see Figure 1.4), the presence of different stages of efferocytosis and the significant implications this may have at the CND tissue level makes this problem all the more challenging. The feed-forward and feedback between phagocytosis and CND structure require the use of multiscale modeling approaches to decipher how they interact during CND elimination. The model developed is novel in nature, combining different biological processes: phagocytosis, extrusion and proliferation at the cellular level as well as cellular rearrangement (drift) at the tissue level.

1.3 Multiscale model of CND elimination

In this thesis, we will combine Markov models of cellular processes of efferocytosis with a submodel for cellular drifting through an advection; the latter is extended to include the source and sink terms representing engulfment, extrusion and proliferation. Using experimental data and boundary conditions to constrain the model (i.e. parameterize), we have been able to adapt it to different conditions, including in vivo wild types, ex vivo non-treated embryos and ex vivo treated embryos upon the application of Blebbistatin. The resulting multiscale model is then used to quantify/characterize certain aspects of this system that cannot not be conducted experimentally. Indeed, in this thesis, we will quantify the digestion time of efferocytosis, the dwell time in each stage of efferocytosis and dissect the relative role of efferocytosis, cell extrusion and proliferation in the process of CND shortening/elongation. The differences in time scale of each process, which could alter the contribution of each component, are integrated into the model and are shown to produce interesting outcomes. The conclusions generated provide insights into the role of each of these components over time independently of each other and in combination when integrated together. Finally, we will examine the effects of Blebbistatin treatment in order to determine the role of actomyosin during CND elimination over time. Even though actomyosin is crucial to the CND shortening (as suggested by the unpublished data from the Bouchard lab), our model shows that efferocytosis is also one of the main driver of the CND shortening and can act independently of actomyosin.

Chapter 2

In vivo model: Wild Type 1

2.1 Experimental data

We first present an in vivo wild type CND data provided by the Bouchard Lab (McGill University), a set of data that we refer to hereafter as Wild Type 1 (WT1). The CND is an epithelial tissue enclosed between an outer cylinder and an inner cylinder. The inner cylinder is called the lumen. A cross-section of the CND is shown on Figure 2.1. The "CND radius" refers to the radius of the outer cylinder. The lumen corresponds to the hollow tube in the center of the nephric duct. As suggested by experimental observations of the Bouchard Lab, the CND and lumen radii remain constant between E11.5 and E13.5. In our modeling efforts, we will take the CND and lumen radii to be constant between E11.5 and E13.5.

During urinary tract development, the displacement of the ureteric bud (i.e., ureter) to its final position in the bladder requires the elimination of the CND. To learn more about the way by which the CND gets eliminated, the Bouchard Lab measured the level of apoptosis in the CND at E11.5 and E12.5. The percentage of nuclei undergoing apoptosis was measured in cross-sections taken from six different regions of the CND ranging from the rostral-most region (rrCND) to the caudal-most region (ccCND). The measure-

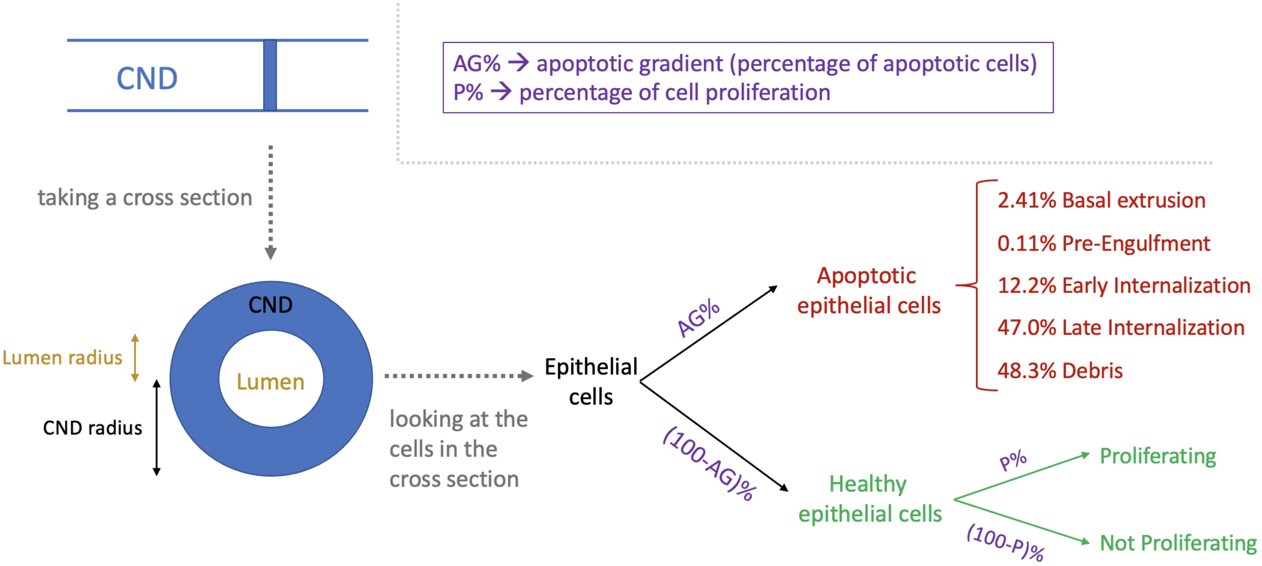

Figure 2.1: The CND is an epithelial tissue enclosed by an outer cylinder and an inner cylinder, called the lumen (a hollow tube). When taking a cross-section of the CND at a specific location and a given time point, the percentage of cells undergoing apoptosis is given by the apoptotic gradient at that specific location and given time point. The remaining cells are healthy epithelial cells. Cells within the pool of apoptotic epithelial cells, are distributed between the five apoptotic states according to the stable (or stationary) distribution given in Figure 2.5 . Within the pool of healthy epithelial cells, there is a small percentage of cells undergoing proliferation. This proliferation percentage is given in Figure 2.3.

ments revealed a gradient of apoptosis from low percentages at the rostral end to high percentages at the caudal end, as shown on Figure 2.2. This apoptotic gradient remained confined within the CND despite a 50% shortening from 306 μm at E11.5 to 153 μm at E12.5, as shown on Figure 2.3. By looking at the values of the apoptotic gradient at the rostral-most and caudal-most regions of the CND at those two time points (see Figure 2.2), we can infer that the end points of the gradient remain roughly unchanged, with the gradient getting steeper. These inferences were confirmed by the members of the Bouchard Lab.

Further experimental analysis was conducted in the Bouchard Lab to gain insights into

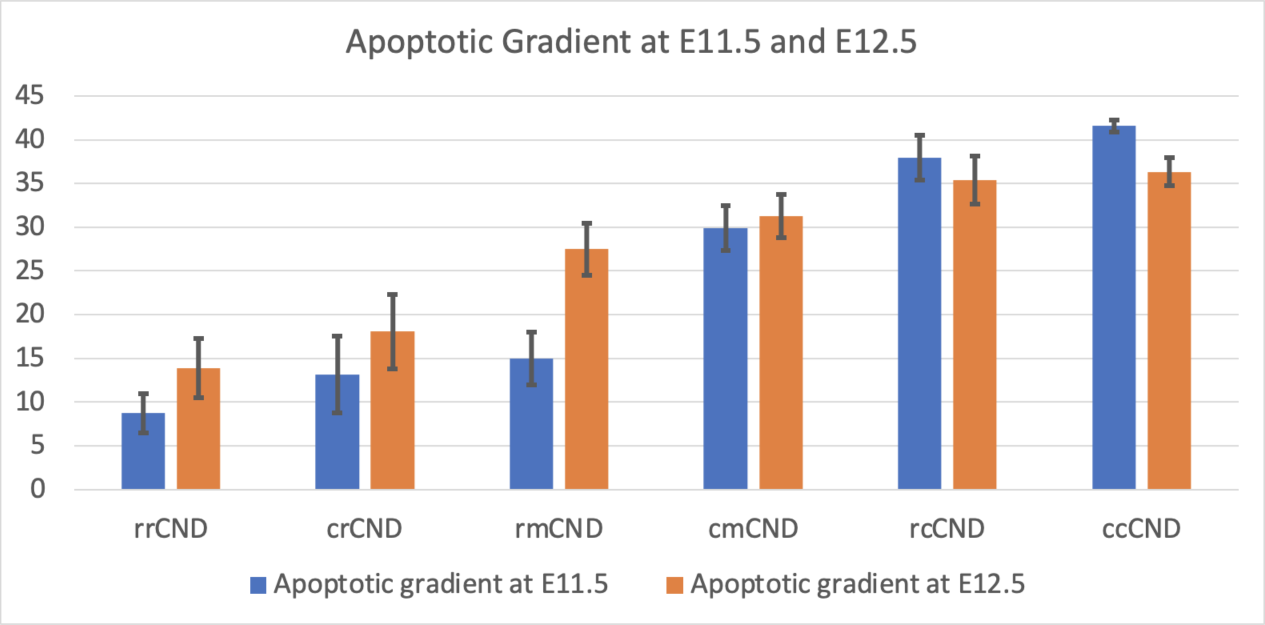

	rrCND	crCND	rmCND	cmCND	rcCND	ccCND
Apoptotic gradient at E11.5	8.71	13.2	15.0	29.9	37.9	41.6
Standard deviation	3.88	7.63	5.18	4.45	4.46	1.20
Standard error of the mean	2.24	4.40	2.99	2.57	2.58	0.694

	rrCND	crCND	rmCND	cmCND	rcCND	ccCND
Apoptotic gradient at E12.5	13.9	18.1	27.5	31.2	35.4	36.3
Standard deviation	7.60	9.50	6.63	5.55	6.16	3.59
Standard error of the mean	3.40	4.25	2.96	2.48	2.76	1.60

Figure 2.2: Unpublished data from the Bouchard Lab: The apoptotic gradient at E11.5 and E12.5. The measurements were averaged over three embryos at E11.5 and five embryos at E12.5. The regions from the most caudal one to the most rostral one are given in the following order: ccCND (caudal-caudal), rcCND (rostral-caudal), cmCND (caudal-middle), rmCND (rostral-middle), crCND (caudal-rostral) and finally rrCND (rostral-rostral CND). In each cross-section, the apoptotic gradient gives the percentage of nuclei undergoing apoptosis out of the total number of nuclei in this cross-section. The standard errors of the mean are shown as error bars on the diagram. The CND was sectioned and immuno-stained with Ecad (cell membrane), TUNEL (dying cells) and Dapi (nucleus) to quantify the number of apoptotic cells in each region. P-values were calculated using two-tailed t-tests between each pair of cell type and were all smaller than 0.05 (and most of them smaller than 0.001).

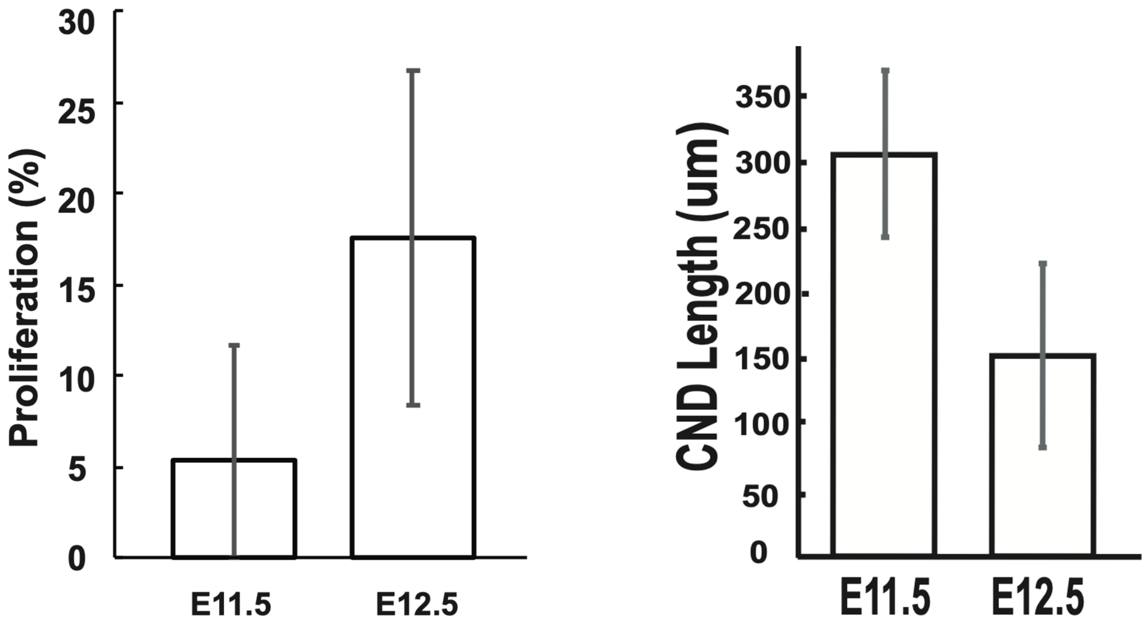

Figure 2.3: Unpublished data from the Bouchard Lab: length of the WT1 CND and proliferation at E11.5 and E12.5. Data presented as mean ± SD. The CND was sectioned and immuno-stained with Ecad (cell membrane), Ki67 (proliferating cells) and Dapi (nucleus) to quantify the number of proliferating cells. The proliferation percentage was obtained out of a total of 594 cells and 1057 cells at E11.5 and E12.5 respectively. E11.5 and E12.5 Urogenital System (UGS) from Pax2GFP (Pax2 is expressed in the UGS system that makes it positive for GFP (Green Fluorescent Protein)) embryos were dissected to measure CND lengths. The length was averaged over 25 CNDs for each of E11.5 and E12.5 and p-values were calculated using two-tailed t-tests and were found to be smaller than 0.0001. The figure was produced by Emily Tang, Phd candidate in the Bouchard Lab.

the cell elimination process. This analysis revealed that the vast majority of the apoptotic cells were engulfed by neighboring epithelial cells from the CND. Using immuno-staining with Ecad (cell membrane), TUNEL (dying cells) and Dapi (nucleus), the progression of non-professional efferocytosis (phagocytosis by epithelial cells) was broken down into four stages (see Figure 2.4): Pre-Engulfment, Early Internalization, Late internalization and Debris stages. In the Pre-Engulfment stage, apoptotic cells became round and lost about 80% of their volume. In the next stage, apoptotic bodies were found as TUNEL-negative condensed masses inside healthy epithelial cells (Early Internalization). These apoptotic bodies eventually acquired TUNEL-positive signal (Late Internalization) and subsequently appeared as debris (Debris stage; shown as fragmented TUNEL staining). A quantification of these different stages showed that the Pre-engulfment and Early Internalization stages are rarely found whereas the Late Internalization and Debris stages are far more dominant (see Figure 2.5). Finally, a small number of cells were found to be extruded from the duct through the basal side (periphery) of the duct, as shown in Figure 2.4. This process is referred to as basal extrusion. The percentage given by the apoptotic gradient is defined as the sum of the percentages of cells in the five different apoptotic states: the Pre-Engulfed, Early-Internalization, Late Internalization, Debris states of efferocytosis and cells undergoing basal extrusion. Even thought the percentage of apoptotic cells increases along the CND (as indicated by the apoptotic gradient), the Bouchard Lab noticed that the distribution of cells within the five apoptotic states remained relatively stable over the six different regions of the CND and over the E11.5 and the E12.5 time points (see Figure 2.5).

To further explore epithelial cell phagocytosis in the CND, the Bouchard Lab looked at the presence of macrophages (professional phagocytes) in and around the CND. While macrophages could be detected in the surroundings of the CND as previously reported [63], very few were in direct contact with the CND and none were found in the CND. To see how apoptotic bodies are processed in engulfing epithelial cells, the Bouchard Lab conducted further experimental works involving lysosome (vesicles containing enzyme capable of breaking down various biomolecules it engulfs) and phagosome (a vesicle formed around a particle engulfed by a phagocyte) markers. The results of these experiments were consistent with the processing of apoptotic bodies through the phagocytic pathways. From these results, they concluded that CND elimination involves non-professional phagocytosis of apoptotic cells by neighbouring epithelial cells, a process referred to as non-professional efferocytosis.

Finally, the Bouchard Lab also measured the percentage of cell proliferation in the CND at E11.5 and E12.5, as shown in Figure 2.3. The unpublished experimental data observations can be summarized in the diagram shown in Figure 2.1. It is important to point out

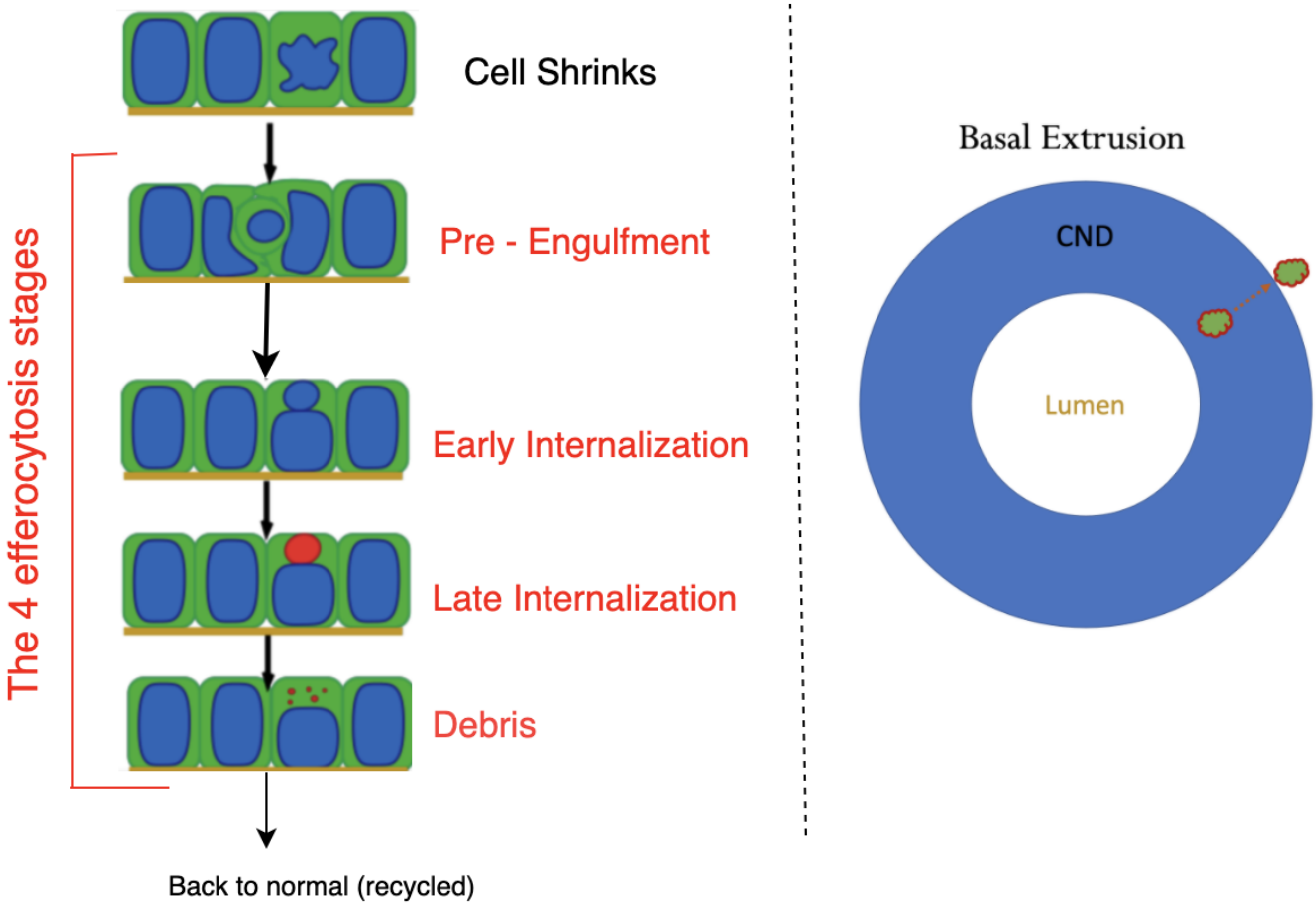

Figure 2.4: The four stages of efferocytosis labeled in red on the left and a cross-section of the process of basal extrusion on the right. During basal extrusion, an apoptotic cell is extruded on the basal side of the CND. The diagram and the image were produced by Emily Tang, PhD candidate in the Bouchard Lab.

that all the cells of the CND are of the same type; there are no cells that are more prone to enter apoptosis or to proliferate. The cells entering apoptosis are randomly selected according to the apoptotic gradient. None of the cells have a predetermined fate: there is no systematic way that a cell is pre-allocated into one pathway versus another (Bouchard Lab). Hereafter, we will refer to healthy epithelial cells with an engulfed apoptotic body inside of them as Phagocytes. All Phagocytes can proliferate and when they do, the engulfed apoptotic body does not get split. In other words, when a Phagocyte proliferate, it produces two different cells: a healthy epithelial cell with no engulfed apoptotic body and a Phagocyte, as shown on Figure 2.11

	Percentage with respect to number of apoptotic cells	**Standard deviation**	**Standard error of the mean**
Basal extrusion	2.41	2.61	0.615
Pre-Engulfment	0.111	0.357	0.0842
Early Internalization	12.2	8.38	1.97
Late Internalization	47.0	14.9	3.51
Debris	38.3	14.0	3.31

Figure 2.5: Unpublished data from the Bouchard Lab: The distribution of the nuclei in the five apoptotic states (including the four stages of efferocytosis identified). A total of eight embryos was used to generate this data: three taken at E11.5 and five taken at E12.5. For each embryo, a cross-section from each of the six regions of the CND (as shown on Figure 2.2) was taken. This makes a total of 48 cross-sections. For each cross-section, the distribution of nuclei between the five apoptotic states (Pre-Engulfed, Early Internalization, Late Internalization, Debris and Basal extrusion) was calculated. The average distribution is given in the above table. The CNDs were sectioned and immuno-stained with Ecad (cell membrane), TUNEL (dying cells) and Dapi (nucleus) to quantify the number of apoptotic cells. P-values were calculated using two-tailed t-tests between each pair of cell type and were all smaller than 0.05 (and most of them smaller than 0.001).

2.2 Mathematical Model and Derivations

In this section, we present the mathematical framework used to model Wild Type 1 (labeled WT1).

2.2.1 Markov model for efferocytosis

The shrinking and eventually the disappearance process of the CND takes place roughly between the E11.5 and E13.5. In a healthy duct, when a cell enters apoptosis, it can either be extruded on the basal side of the CND or it can be internalized by a neighboring cell through non-professional efferocytosis (also called non-professional phagocytosis). During efferocytosis, the cells in the CND undergo four different stages highlighted in Figure 2.4. To understand these four different stages, we introduce here the following list of definitions that will be used quite frequently hereafter:

- **Normal cell**: is a healthy cell maintaining its volume.
- **Pre-Engulfment** stage: is the stage associated with the shrinking process of Normal cells until they become ready for engulfment; we also call a cell in that stage an **apoptotic body**.
- **Early Internalization** stage: is the stage occuring right after the engulfment of apoptotic bodies.
- **Late Internalization** stage: is the stage in which the engulfed apoptotic bodies undergo active DNA fragmentation. The red dots of Figure 2.4 represents the accumulation of double stranded DNA breaks.
- **Debris** stage: is the stage in which the nucleus is degraded into non-detectable small pieces, but the DNA breaks remain detectable (red dots in Fig 2.4).
- **Phagocyte**: is a Normal cell that has engulfed an apoptotic body. When digestion is over, the Phagocyte returns to being a Normal cell.

The efferocytosis process can be described by an irreversible Markov model consisting of 5 states, as shown on Figure 2.6.

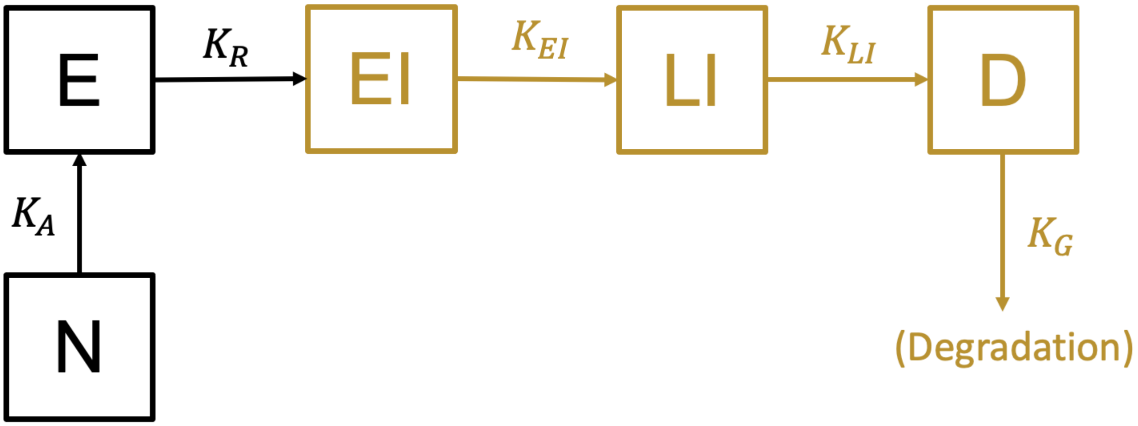

Figure 2.6: The irreversible 5-states Markov model consistent with that shown in Figure 2.4. "N" stands for "Normal", "E" for "Pre-Engulfment", "EI" for "Early Internalization", "LI" for "Late Internalization" and "D" for "Debris".

Let $N(t)$, $E(t)$, $Ei(t)$, $Li(t)$ and $D(t)$ denote the total number of cells in the Normal, Pre-engulfed, Early-internalized, Late-internalized and Debris stages, respectively, at time t (in days). At E11.5, we set $t = 0$ days, whereas at E13.5, we set $t = 2$ days. Let K_A, K_R, K_{EI} and K_{LI} be the forward rate constants for the transitions $N(t) \to E(t)$, $E(t) \to Ei(t)$, $Ei(t) \to Li(t)$ and $Li(t) \to D(t)$, respectively, while K_G be the degradation rate. We will refer to K_A as the **efferocytosis rate** and K_R as the **engulfment rate**.

Our immediate goal is to quantify the dwell time spent in the four stages of the efferocytosis process because each stage is associated with a biological process that is taking place within the cell. For example, the Late Internalization stage is associated with active DNA fragmentation, so determining the dwell time tells us the time constant of this process. Furthermore, determining the dwell time of the Debris stage tells us how long the DNA breaks remain detectable. Quantifying these parameters is thus quite important as it may provide some fundamental information about which one of these stages is altered in pathological conditions (e.g., during vesicoureteral reflux and junction obstruction) in a manner similar to what was done with macrophage phagocytosis [35]. We need to determine the values of K_A, K_R, K_{EI}, K_{LI} and K_G, and then compute the reciprocal of these parameters to determine the dwell time in the Normal, Pre-engulfed, Early-internalized, Late-internalized and Debris states, respectively.

To tackle this problem, we need to introduce the following types of cells.

- A **Dead** cell: is a cell in the E, EI, LI or D state of Figure 2.6.
- An **Engulfed** cell: is a cell in the EI, LI or D state of Figure 2.6.

Based on these definitions, we can simplify the 5-state Markov model of Figure 2.6 into a 3-state irreversible Markov model (shown in Figure 2.7).

K_D represents the **digestion rate** and its reciprocal gives the time an engulfed cell stays in the Phagocyte, i.e. the digestion time. The digestion rate K_D represent the combined rate of K_{EI}, K_{LI} and K_G.

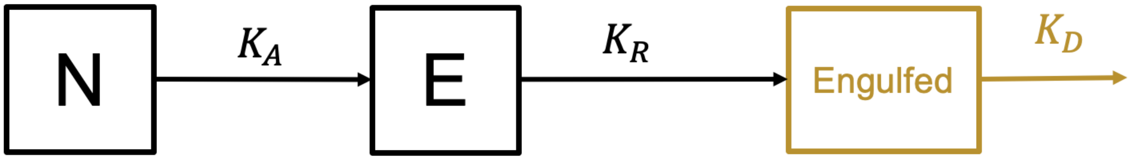

Figure 2.7: The irreversible 3-state Markov model whose Early Internalization, Late Internalization and Debris states have been merged into one called the Engulfed state. "N" stands for "Normal" and "E" for "Pre-Engulfment".

As shown on Figure 2.5, the percentage of cells in the Pre-Engulfment state is close to 0. Moreover, out of a total of 48 cross-sections that were analyzed (as mentioned in Figure 2.5), 43 cross-sections had 0% of cells in the Pre-Engulfment state. This means that the time spent in the Pre-Engulfment state is the shortest and cells in this state are the hardest to observe, and will therefore have the largest uncertainty. Based on this data, we assume that the engulfment process, represented by the K_R arrow, is instantaneous. Hence, the 5-state and 3-state Markov models of Figures 2.6 and 2.7, respectively, can be simplified into 4-state and 2-state Markov models, shown in Figure 2.8. To verify that this would not affect our results significantly, we have used the original 5-state and 3-state Markov models shown in 2.6 and 2.7, respectively, and obtained results that differed quantitatively by less than 0.4% compared to the 4-state and 2-state Markov models as shown below. We have found that the value of K_R is three orders of magnitude bigger than the other rates.

2.2.2 Stationary cellular distribution

Unpublished data from Bouchard Lab suggests that the distribution of apoptotic cells into the four efferocytosis stages and the basal extrusion between E11.5 and E12.5 is stable over time (non-changing, see Figure 2.5). This represents the stationary distribution of the system.

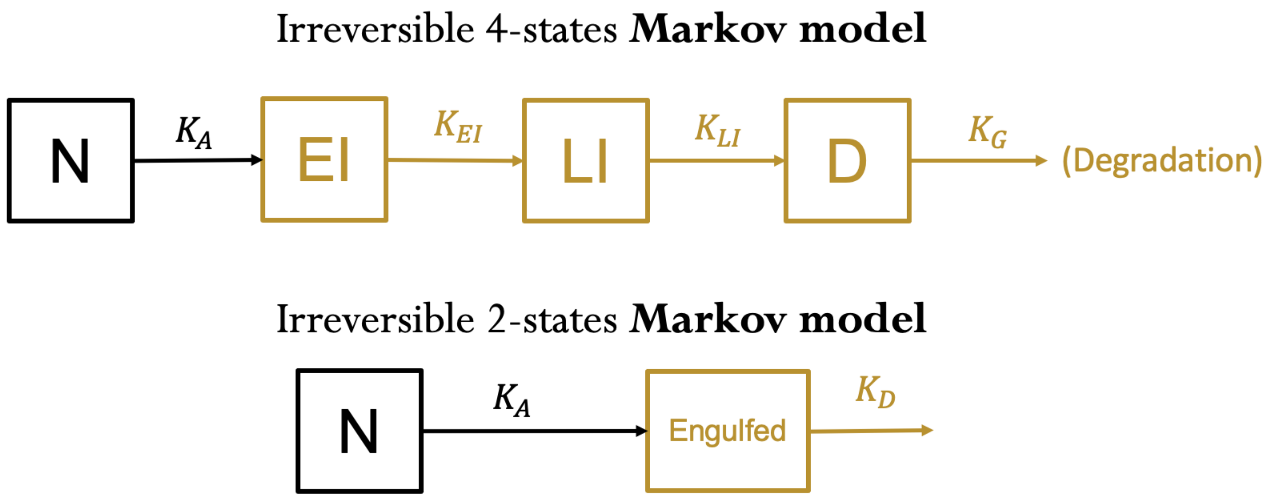

Figure 2.8: Top: The irreversible 4-states Markov model with the engulfment process assumed to be instantaneous. Bottom: The irreversible 2-state Markov model whose Early Internalization, Late Internalization and Debris states have been merged into one called the Engulfed state. "N" stands for "Normal", "EI" for "Early Internalization", "LI" for "Late Internalization" and "D" for "Debris".

2.2.3 Apoptotic gradient

The length of the CND decreases overtime but the diameter remains the same as confirmed by the Bouchard Lab. During this process, the CND remains directly connected to the bladder and shortens due to the apoptotic gradient. As suggested by the experimental data shown in Section 2.1, the endpoints of the apoptotic gradient remain roughly constant over time, which implies that the gradient is getting steeper. The average apoptotic gradient is calculated and is shown in Figure 2.9.

2.2.4 Multistate model of cellular interactions

To better understand the dynamics of CND shortening, we will further use a multistate model to describe the different cell pathways in the CND in terms of their volume fraction (see Figure 2.10). This alternate model description will allow us to account for Normal cells and Phagocytes. The cell states and rate constants used in this multistate model are described in the *Nomenclature*.

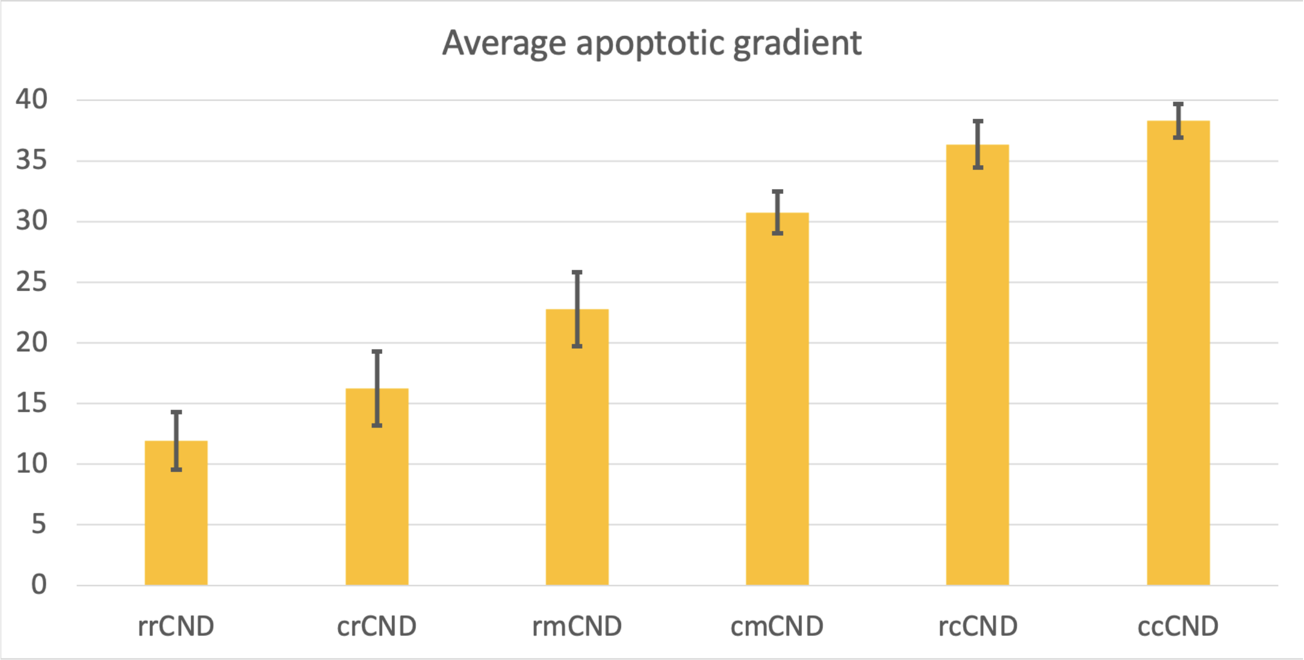

	rrCND	crCND	rmCND	cmCND	rcCND	ccCND
Average apoptotic gradient	11.9	16.3	22.8	30.7	36.4	38.3
Standard deviation	6.67	8.64	8.64	4.87	5.40	3.89
Standard error of the mean	2.36	3.05	3.05	1.72	1.91	1.37

Figure 2.9: Unpublished data from the Bouchard Lab. A total of eight embryos was used to generate this data: three taken at E11.5 and five taken at E12.5. For each embryo, a cross-section of the 6 regions ranging from the most rostral to the most caudal (rrCND, crCND, rmCND, cmCND, rcCND and ccCND) was taken. For each cross-section, the percentage of apoptotic cells with respect to the total number of cells in the cross-section was measured. The percentages of apoptotic cells in each region was averaged over the eight different embryos and are shown above. The standard errors of the mean are shown as error bars on the diagram.

The volume of a Pre-Engulfed cell is 20% of the volume of a Normal cell. Therefore, when a Normal cell engulfs a Pre-Engulfed cell, it becomes a Phagocyte that is 20% bigger than a Normal cell. It is important to recall that the engulfment process is assumed to be instantaneous. This is why it does not appear in the multistate model shown in Figure 2.10. We now introduce a unitless quantity that we call "volume fraction". The volume fraction of an entity is equal to the ratio of its volume over the volume of a Normal cell.

For example, since a Phagocyte is 20% bigger than a Normal cell, the volume fraction of a Phagocyte is equal to 1.2. In order to avoid any confusion when discussing volume fraction (unitless) versus number of cells, we make the following observations.

- A Normal cell occupies a volume fraction of 1. A Phagocyte occupies a volume fraction of 1.2.
- Based on the previous assumption, at a specific time point, the number of Normal cells is equal to the volume fraction of N.
- Based on the first assumption stated above, if the volume fraction of P is known, then the total number of Phagocytes is equal to this volume fraction divided by 1.2

When a cell enters apoptosis, it shrinks and loses 80% of its volume through water release ($1 - f_e = 0.8$) and gets engulfed by a neighboring Normal cell at a rate K_A or gets pushed out of the CND through basal extrusion at rate K_{BX}. The cells that are proliferating can not enter apoptosis or engulf a Pre-Engulfed cell; we therefore use f_n to denote the fraction of cells not proliferating. The Normal cells that engulf Pre-Engulfed cells are turned into Phagocytes at rate K_P. When a Normal cell is turned into a Phagocyte, it gains a 0.2 volume fraction ($f_e = 0.2$) corresponding to the engulfment of a Pre-Engulfed cell (through the $f_n f_e K_A$ transition). When the Phagocytes are done digesting, they revert back to being Normal cells again; this occurs at a rate identical to the digestion rate K_D (since digestion and reversion are the same processes). When a Phagocyte is turned back into a Normal cell, it loses the 0.2 volume fraction occupied by the Pre-Engulfed cell ($f_e/(f_e + 1)K_D$ transition) and the remaining 1 volume fraction is turned back into a Normal cell ($1/(f_e + 1)K_D$ transition). Details of these interactions are described by the scheme on Figure 2.10.

During development, cells proliferate. Unpublished data by the Bouchard Lab (McGill University) shown on Figure 2.3 suggests that there are, on average, 11.4$\%$ ($f_n = 0.886$) of Normal cells and Phagocytes that undergo proliferation. This mean that a Phagocyte can undergo cell division while digesting another cell. It was also estimated that the duration

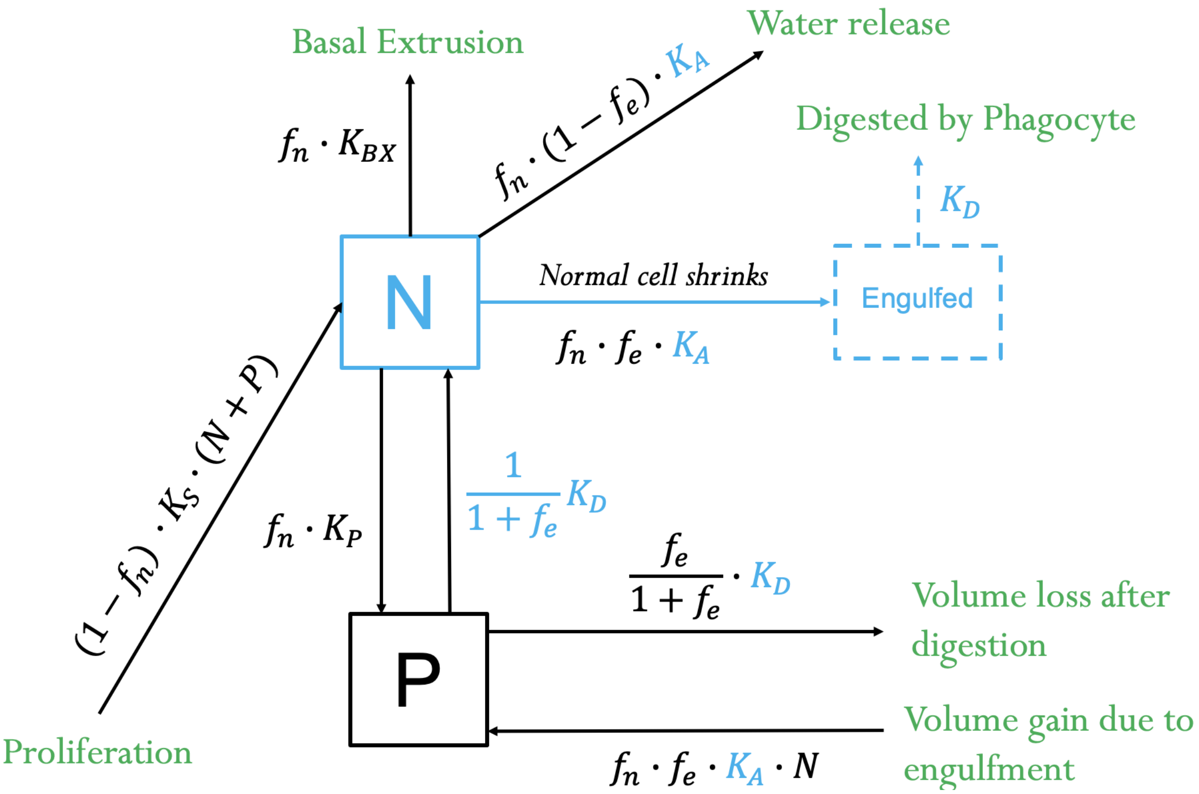

Figure 2.10: The multistate model, "MS1", describing the interactions between the different types of cells in terms of volume fraction. The efferocytosis pathway is colored in blue."N" stands for "Normal" and "P" stands for "Phagocytes". There is a $1 - f_n$ fraction of Normal cells that undergo proliferation. The rest of the Normal cells can either be extruded on the basal side of the CND at rate K_{BX} or enter efferocytosis (blue pathway) at a rate K_A. When a Normal cell undergoes efferocytosis, it first shrinks and loses 80% of its volume ($1 - f_e = 0.8$) and then gets engulfed by a neighboring cell. Normal cells that engulf Pre-Engulfed cells get turned into Phagocytes at a rate K_P. When a Normal cell is turned into a Phagocyte, it gains a 0.2 volume fraction ($f_e = 0.2$) corresponding to the engulfment of a Pre-Engulfed cell (through the $f_n f_e K_A$ transition). When the Phagocytes are done digesting, they revert back to being Normal cells again; this occurs at a rate identical to the digestion rate K_D (since digestion and reversion are the same processes). When a Phagocyte is turned back into a Normal cell, it loses the 0.2 volume fraction occupied by the Pre-Engulfed cell ($f_e/(f_e + 1)K_D$ transition) and the remaining 1 volume fraction is turned back into a Normal cell ($1/(f_e + 1)K_D$ transition).

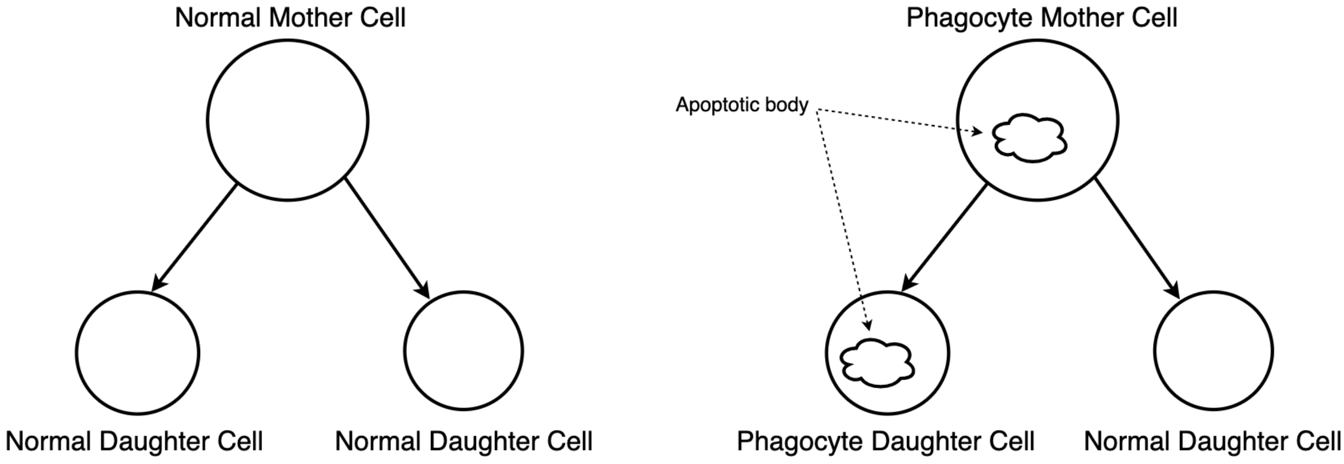

Figure 2.11: Cell proliferation: a mother Normal cell produces two daughter Normal cells but a mother Phagocyte produces one Normal cell and one Phagocyte.

of cell cycle is about 18 hours ($K_S = 18/24$ days^{-1}). When a Normal cell divides, it gives birth to two daughter cells that are Normal cells, whereas when a Phagocyte divides, it gives birth to one Phagocyte and one Normal cell (see Figure 2.11). Thus, according to both scenarios, the system gains one new Normal cell and the number of Phagocytes remains the same. It is important to note here that a Normal cell undergoing proliferation can not enter apoptosis or be turned into a Phagocyte.

The average percentage of cells proliferating between E11.5 and E12.5 is 11.4%. Therefore, the fraction of cells not proliferating (f_n) is set to be 0.886 (corresponding to 11.4%) in the model presented above. Given that the percentage of cells proliferating at E11.5 (5.3%) and at E12.5 (17.5%) are significantly different (Figure 2.3, we also set f_n to be 0.947 (5.3% proliferation) and 0.825 (17.5% proliferation) to see how these values affect the outcomes of the MS1 model. Our results revealed that there is around a 7% difference in the value of K_D when compared to the K_D obtained when $f_n = 0.886$ (Table 4 in the Appendix). As for the heatmaps of the rate of efferocytosis K_A, the qualitative behaviour remains the same, but the maximum value attained by K_A differs by around 20% when compared with model when $f_n = 0.886$ (Figures 2.14 and Figures 4.2 and 4.3 of the Appendix). The heatmaps of the drifting velocity v, on the other hand, remains almost identical in all cases (Figures 2.15 and Figures 4.2 and 4.3 of the Appendix). Because of these small differences, we have decided to use the average percentage of cell proliferation (11.4%) in the modeling analysis.

2.2.5 Fluid dynamics model for cellular drifting

As mentioned in the introduction, for the CND to maintain its uniform diameter and its apoptotic gradient, a flux of cells moving toward the bladder must occur. This follows from the fact that if more cells are dying in the caudal region of the CND (i.e., at the bladder side of Figure 2.12) than in the rostral region of the CND away from the bladder (as suggested by the apoptotic gradient), then the radius of the former will decrease quicker than that of the latter, causing the CND to have a non-uniform diameter. Since the CND maintains a uniform diameter, it follows that there is a cellular drift from the rostral region of the CND toward the caudal (see Figure 2.12). This cellular drift leads to the shortening of the CND.

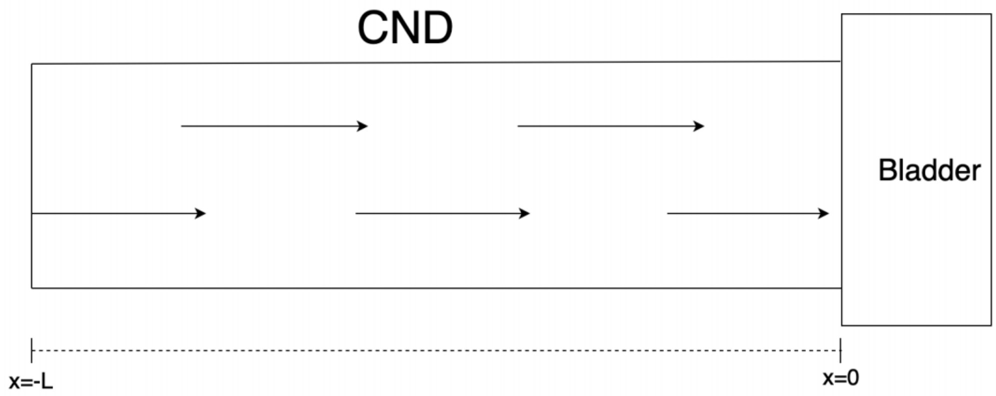

Figure 2.12: A longitudinal view of the CND with arrows indicating the direction of cellular drift from the rostral (away from the bladder) to the caudal (close to the bladder) regions. The rostral end $x = -L$ corresponds to the shrinking end of the CND and the caudal end $x = 0$ corresponds to the one connected to the bladder.

To study the dynamics of this system in the presence of a cellular drift, we need to introduce the variables ρ_N and ρ_P that represent the densities of Normal cells and Phagocytes, respectively, expressed as volume fraction per micrometers. Since volume fraction is unitless, the unit of ρ_N and ρ_P is μm^{-1}. For example, if there are 4 Normal cells in a 2 μm long segment of the CND, then ρ_N in that segment is

$$\rho_N = \frac{4 \times 1}{2} = 2 \quad \mu m^{-1}.$$

However, if there are 4 Phagocytes in a 2 μm long segment of the CND, then ρ_P in that segment is

$$\rho_E = \frac{4 \times 1.2}{2} = 2.4 \quad \mu m^{-1}.$$

Let $v(x,t)$ denote the velocity of cells drifting longitudinally along the CND at location x and time t. Using cell densities, we can describe the spatiotemporal dynamics of this system by extending the drift-diffusion (also called the diffusion-advection) equation to include the source and sink terms of Figure 2.10. This produces the following equations

$$\frac{\partial \rho_N}{\partial t} = -\frac{\partial}{\partial x}(v\rho_N) - f_n(K_A + K_{BX} + K_P)\rho_N + \frac{1}{1+f_e}K_D\rho_P \tag{2.1}$$

$$+ (1-f_n)K_S(\rho_N + \rho_P)$$

$$\frac{\partial \rho_P}{\partial t} = -\frac{\partial}{\partial x}(v\rho_P) + f_n\left(K_P + f_eK_A\right)\rho_N - K_D\rho_P \tag{2.2}$$

Since there is no diffusion is this system, it is not included in the model; instead, cell movement is described by a drift (advection) term, given by $\partial v\rho_i/\partial x$, for $i = N$ and P. To quantify the various parameters of the model, further analysis will be conducted.

2.2.6 Basal extrusion versus efferocytosis

Based on unpublished data by the Bouchard Lab (McGill University), we can determine a proportional relation between the rate of efferocytosis K_A and the rate of basal extrusion K_{BX}. Using biological markers, it was determined that the time it takes for a cell to be extruded out of the CND is the same as the time it takes for a cell to reach the middle of the Late Internalization stage. Let's suppose that the stationary distribution is given by

Basal Extrusion $\rightarrow A\%$
Early Internalized $\rightarrow E_I\%$
Late Internalized $\rightarrow L_I\%$
Debris $\rightarrow D\%.$

If we let K_T denote the rate of apoptosis (basal extrusion and efferocytosis), i.e. $K_T = K_A + K_{BX}$, we obtain

$$\begin{aligned} K_A &= \frac{E_I + L_I/2}{A + E_I + L_I/2} K_T \\ K_{BX} &= \frac{A}{A + E_I + L_I/2} K_T. \end{aligned}$$

This gives a proportional relation between K_A and K_{BX}, given by

$$K_{BX} = \frac{A}{E_I + L_I/2} K_A. \tag{2.3}$$

2.2.7 Important equations

In this section we set up boundary conditions and important equations that will be used in Section 2.3 to solve the model analytically.

Biological conditions and assumptions on rate constants (validated by the Bouchard Lab)

It is to be expected that the rate of efferocytosis K_A is closely correlated to the apoptotic gradient. By applying linear regression (Figure 2.13) on the apoptotic gradients at E11.5 and E12.5 (Figure 2.2) and on the averaged apoptotic gradient (Figure 2.9) along the length of the CND, we obtain R^2-values that are close enough to 1 (always bigger than

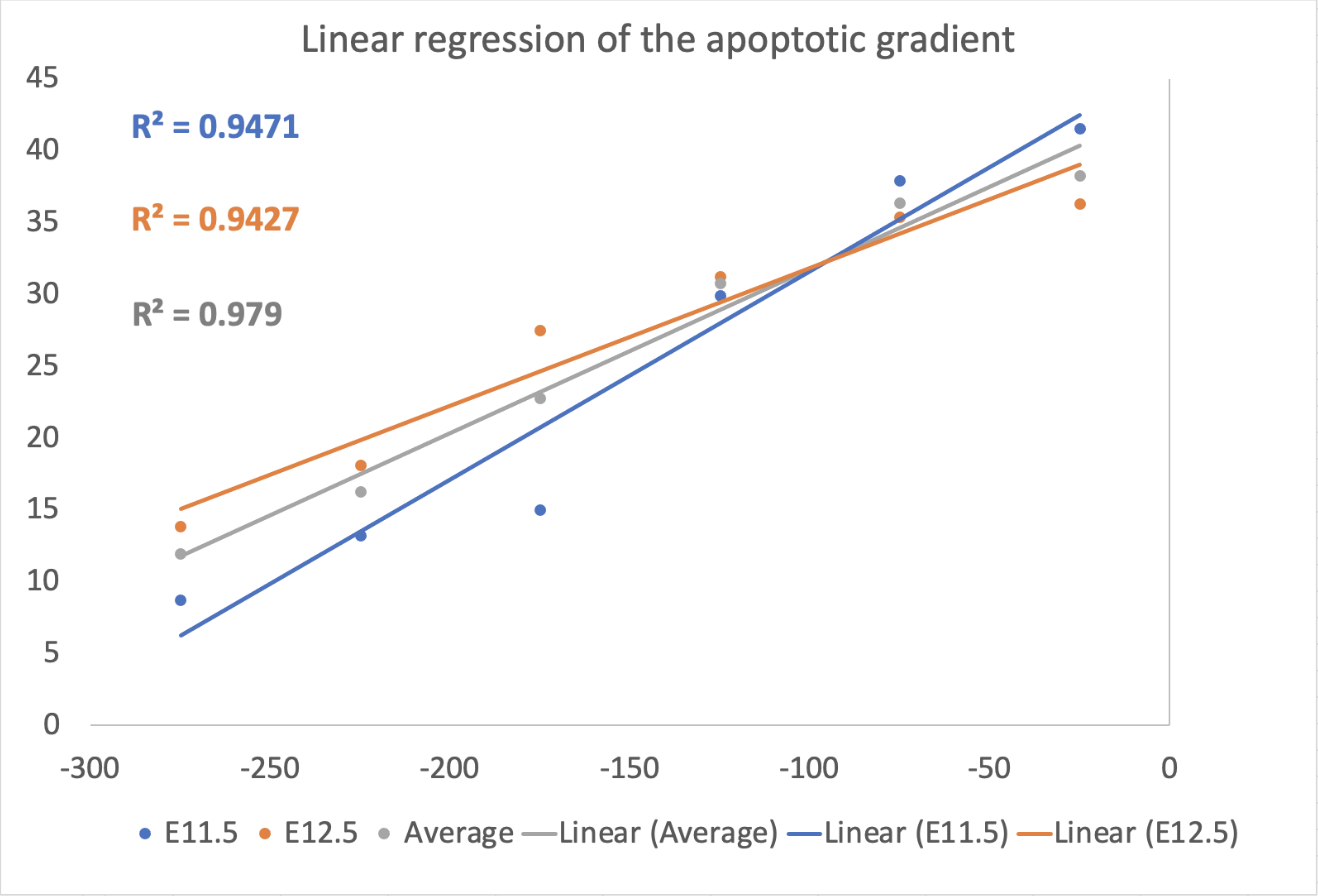

Figure 2.13: Linear regressions applied on the apoptotic gradients at E11.5 (blue) and at E12.5 (orange) and on the averaged apoptotic gradient (grey). The data points of each gradient are taken from Figures 2.2 and 2.9. For each gradient, the data points are taken at the regions ranging from the most rostral end to the most caudal end, as shown on Figure 2.9. To apply a linear regression, we set the length of the CND to $L = 300\ \mu m$, set the caudal and rostral ends to $x = 0$ and $x = -L\ \mu m$, respectively (as shown on Figure 2.12), and associate each data point to the middle point of the corresponding region. For example, in the case of the rrCND region extending from -300 to -250 μm, the data point is plotted at $-275\ \mu m$, the mid point of the rrCND region. The R^2-values are independent of the value of the length of the CND L.

0.94) to suggest that the rate of efferocytosis K_A varies linearly along the CND. Therefore, we approximate the rate of efferocytosis K_A to be a linear function of space (x) with end points (at $x = 0$ and $x = -L(t)$) that are independent of the length $L(t)$ of the CND (as suggested in Section 2.3.1), i.e.,

$$K_A(x) = \frac{c}{-L(t)}x + d, . \tag{2.4}$$

As mentioned earlier, the Engulfed state of Fig 2.7 incorporates the Early Internalized, Late Internalized and Debris states of Fig 2.6. Based on this, we have

$$\frac{1}{K_D} = \frac{1}{K_{EI}} + \frac{1}{K_{LI}} + \frac{1}{K_G}. \tag{2.5}$$

Using the stationary distribution associated with Early Internalized, Late Internalized and Debris states, given by

Early Internalization → $E_I\%$

Late Internalization → $L_I\%$

Debris → $D\%$,

we conclude that

$$\frac{1}{K_{L_I}} = \frac{L_I}{E_I}\left(\frac{1}{K_{E_I}}\right) \tag{2.6}$$

$$\frac{1}{K_G} = \frac{D}{E_I}\left(\frac{1}{K_{E_I}}\right). \tag{2.7}$$

Differential Equations

By letting ρ_T denote the total density of cells in the CND, we have

$$\rho_T := \rho_N + \rho_P + \rho_A,$$

and since the CND has a uniform diameter, ρ_T is constant in time and space. ρ_A has not been introduced yet, it is the density of the apoptotic cell bodies being extruded out of the CND to the basal side. Using the differential equations 2.1 and 2.2 and since ρ_T is constant, we obtain

$$\frac{\partial \rho_T}{\partial t} = \frac{\partial}{\partial t}(\rho_N + \rho_P + \rho_A), \text{ which implies that}$$

$$\begin{aligned}
0 =& \frac{\partial \rho_N}{\partial t} + \frac{\partial \rho_P}{\partial t} + \frac{\partial \rho_A}{\partial t} \qquad (2.8) \\
=& - f_n((1-f_e)K_A + K_{BX})\rho_N + (1-f_n)(\rho_N+\rho_P)K_S - \frac{f_e}{1+f_e}K_D\rho_P \\
& - (\frac{\partial}{\partial x}(v\rho_N) + \frac{\partial}{\partial x}(v\rho_P) + \frac{\partial}{\partial x}(v\rho_A)) \\
=& - f_n((1-f_e)K_A + K_{BX})\rho_N + (1-f_n)(\rho_N+\rho_P)K_S - \frac{f_e}{1+f_e}K_D\rho_P \\
& - (\rho_N\frac{\partial v}{\partial x} + v\frac{\partial \rho_N}{\partial x} + \rho_P\frac{\partial v}{\partial x} + v\frac{\partial \rho_P}{\partial x} + \rho_A\frac{\partial v}{\partial x} + v\frac{\partial \rho_A}{\partial x}) \\
=& - f_n((1-f_e)K_A + K_{BX})\rho_N + (1-f_n)(\rho_N+\rho_P)K_S - \frac{f_e}{1+f_e}K_D\rho_P \\
& - ((\rho_N+\rho_P+\rho_A)\frac{\partial v}{\partial x} + v\frac{\partial}{\partial x}(\rho_N+\rho_P+\rho_A)) \\
=& - f_n((1-f_e)K_A + K_{BX})\rho_N + (1-f_n)(\rho_N+\rho_P)K_S - \frac{f_e}{1+f_e}K_D\rho_P - (\rho_T\frac{\partial v}{\partial x} + v\frac{\partial \rho_T}{\partial x}) \\
=& - f_n((1-f_e)K_A + K_{BX})\rho_N + (1-f_n)(\rho_N+\rho_P)K_S - \frac{f_e}{1+f_e}K_D\rho_P - (\rho_T\frac{\partial v}{\partial x} + 0) \\
=& - f_n((1-f_e)K_A + K_{BX})\rho_N + (1-f_n)(\rho_N+\rho_P)K_S - \frac{f_e}{1+f_e}K_D\rho_P - \rho_T\frac{\partial v}{\partial x}.
\end{aligned}$$

Rearranging these terms, we obtain the following differential equation for the cellular velocity $v(x,t)$

$$\rho_T\frac{\partial v}{\partial x} = -f_n((1-f_e)K_A + K_{BX})\rho_N + (1-f_n)(\rho_N+\rho_P)K_S - \frac{f_e}{1+f_e}K_D\rho_P. \qquad (2.9)$$

As mentioned earlier, $x = -L$ corresponds to the rostral end of the CND and $x = 0$ corresponds to the caudal end of the CND. Since the caudal end of the CND does not move, we use the following boundary condition for $v(x,t)$:

$$v(0,t) = 0. \tag{2.10}$$

Note that the velocity at the shrinking end of the CND (rostral end) corresponds to the rate at which the length $L(t)$ of the CND decreases. We can thus set

$$\frac{\partial L(t)}{\partial t} = -v(x,t)\big|_{x=-L(t)}. \tag{2.11}$$

Boundary conditions on the dynamics of the system

To reduce the number of parameters of the model, we need to make the value of the rate of efferocytosis K_A at the rostral end of the CND a boundary condition for the model. Given the low percentage of the apoptosis in the most rostral region of the CND (Figure 2.9), one would expect K_A to be very close to 0 at that end. Based on this, We have set $K_A = 0$ (an assumption approved by the Bouchard Lab) because it is the minimal value that K_A can attain; by choosing a different value close to 0, the analysis would remain the exact same qualitatively and the results would quantitatively differ only slightly. For example, when setting K_A equal to 0.50 at the rostral end, the predicted value of K_D and the heatmap of the drifting velocity v remain the same, while the maximum value attained by K_A decreases by only 18%. Based on this, we have decided to make the assumption that at the shrinking rostral end of the CND, the rate of efferocytosis is zero. This gives

$$K_A(-L(t),t) = 0. \tag{2.12}$$

Since at any given time point, K_A increases linearly along the CND, this assumption does not mean that there exists a region along the CND with a rate of efferocytosis equal to zero; since $K_A(x,t) > 0$ for any $x > -L(t)$, then for all $l > -L(t)$, the average K_A is always strictly bigger than 0 on the region extending from $x = -L(t)$ to $x = l$.

As discussed earlier, when a cell is engulfed by a neighboring cell, one Normal cell is turned into a Phagocyte. If one Normal cell turns into a Phagocyte at time $t = \alpha$ days, then at time $t = \alpha + 1/K_D$ days, this cell will revert back to being a Normal cell because $1/K_D$ days corresponds to the digestion time. This means that the number of cells that have been engulfed between $t = 0$ and $t = T$ days (left hand side of equation 2.13) should be equal to the number of Phagocytes that have turned back into Normal cells between $t = 1/K_D$ and $t = T + 1/K_D$ days (right hand side of equation 2.13). The latter can be expressed as the number of cells that went from the P state to the N state to which we add the number of Phagocytes at $t = T$ days (because they will turn back to Normal cells before $t = T + 1/K_D$) and subtract the number of Phagocytes at $t = 0$ (because they will turn back to Normal cells before $t = 1/K_D$ days). Mathematically, this is equivalent to saying that

$$\underbrace{\int_0^T \int_{-L(t)}^0 f_n K_A \rho_N dx dt}_{\substack{\text{Number of Pre-Engulfed}\\ \text{cells engulfed by}\\ \text{Phagocytes}\\ \text{between } t\text{=}0 \text{ and } t\text{=}T \text{ days.}}} = \underbrace{\int_0^T \int_{-L(t)}^0 K_D \frac{\rho_P}{1+f_e} dx dt}_{\substack{\text{Number of Phagocytes}\\ \text{returning back to being}\\ \text{Normal cells between } t\text{=}0\\ \text{and } t\text{=}T \text{ days.}}} + \underbrace{\int_{-L(T)}^0 \frac{\rho_P(T,x)}{1+f_e} dx}_{\substack{\text{Number of}\\ \text{Phagocytes}\\ \text{at } t\text{=}T \text{ days.}}} - \underbrace{\int_{-L(0)}^0 \frac{\rho_P(0,x)}{1+f_e} dx}_{\substack{\text{Number of}\\ \text{Phagocytes}\\ \text{at } t\text{=}0 \text{ days.}}}, \tag{2.13}$$

where $(1 + f_e) = 1.2$ is a scaling factor that corresponds to the volume fraction occupied by a Phagocyte, $K_D \rho_P$ represents the volume fraction loss from the P state and $\frac{K_D \rho_P}{1+f_e}$ represents the number of cells transitioning from the P state to the N sate.

Quantifying cellular velocity

Integrating both sides of equation 2.9, we obtain

$$\int_{-L(t)}^0 \rho_T \frac{\partial v(x,t)}{\partial x} dx = \int_{-L(t)}^0 -f_n((1-f_e)K_A + K_{BX})\rho_N + (1-f_n)(\rho_N + \rho_P)K_S - \frac{f_e}{1+f_e} K_D \rho_P \, dx,$$

which implies that

$$\rho_T[v(0,t) - v(-L(t),t)] = \int_{-L(t)}^{0} -f_n((1-f_e)K_A + K_{BX})\rho_N + (1-f_n)(\rho_N + \rho_P)K_S - \frac{f_e}{1+f_e}K_D\rho_P \, dx.$$

Since the caudal end of the CND connecting to the bladder does not move, we have $v(0,t) = 0\ \mu m/days$ for all t. This means that

$$\rho_T[0 - v(-L(t),t)] = \int_{-L(t)}^{0} -f_n((1-f_e)K_A + K_{BX})\rho_N + (1-f_n)(\rho_N + \rho_P)K_S - \frac{f_e}{1+f_e}K_D\rho_P \, dx$$

which implies that

$$-\rho_T v(-L(t),t) = \int_{-L(t)}^{0} -f_n((1-f_e)K_A + K_{BX})\rho_N + (1-f_n)(\rho_N + \rho_P)K_S - \frac{f_e}{1+f_e}K_D\rho_P \, dx.$$

Let $R_V(t)$ denote the rate of CND volume loss at time t. It follows that

$$R_V(t) = \int_{-L(t)}^{0} f_n((1-f_e)K_A + K_{BX})\rho_N - (1-f_n)(\rho_N + \rho_P)K_S + \frac{f_e}{1+f_e}K_D\rho_P,$$

and therefore,

$$\rho_T v(-L(t),t) = R_V(t). \tag{2.14}$$

We will use the notation $R_V(t)$ in Section 3.2.5. We can subsequently conclude that

$$\int_0^T R_V(t)dt$$

provides a quantification for the total volume loss between $t = 0$ and $t = T$ days.

Substituting equation 2.11 into equation 2.14, we obtain

$$-\rho_T \frac{\partial L(t)}{\partial t} = R_V(t). \tag{2.15}$$

Note that $\frac{\partial L(t)}{\partial t}$ corresponds to the rate at which the length of CND decreases.

2.2.8 Quantifying the density of each type of cells using experimental data

Let ρ_T denote the total density of the duct in terms of volume fraction per micrometers (i.e., the unit of ρ_T is μm^{-1} because volume fraction is unitless). This means that

$$\rho_T := \rho_N + \rho_P + \rho_A.$$

Since the CND has a uniform diameter, it implies that ρ_T is constant in time and space. In WT1 (as well as in the ex-vivo Control model associated with the CND analyzed in the next chapter), we know from unpublished data from the Bouchard Lab (McGill University) that $\rho_T = \frac{2000}{300}\mu m^{-1}$. For Blebbistatin treated CND, the calculation of ρ_T is done in Section 3.2.4.

For any given time point, we assume that the apoptotic gradient is a linear function of space, as suggested by Figure 2.13. This means that:

$$\frac{\rho_N}{\rho_T}(x) = \frac{a}{-L(t)}x + b, \tag{2.16}$$

$$\frac{\rho_P}{\rho_T}(x) = \frac{g}{-L(t)}x + h. \tag{2.17}$$

Then, $\frac{\rho_A}{\rho_T}(x)$ can be determined simply by using the following equation

$$\frac{\rho_A}{\rho_T}(x) = 1 - \frac{\rho_N}{\rho_T}(x) - \frac{\rho_P}{\rho_T}(x).$$

From data provided by Bouchard Lab (McGill University), we can retrieve (see next subsection) the values of

$$\frac{\rho_N}{\rho_T}(-L(t)), \quad \frac{\rho_P}{\rho_T}(-L(t)), \tag{2.18}$$

$$\frac{\rho_N}{\rho_T}(0), \quad \frac{\rho_P}{\rho_T}(0). \tag{2.19}$$

Using equations 2.16, 2.17, 2.18 and 2.19, we obtain a system of two equations with two unknowns for each variable ρ_N and ρ_P, given by

$$\frac{\rho_N}{\rho_T}(-L(t)) = a + b, \quad \frac{\rho_P}{\rho_T}(-L(t)) = g + h \tag{2.20}$$

$$\frac{\rho_N}{\rho_T}(0) = b, \quad \frac{\rho_P}{\rho_T}(0) = h. \tag{2.21}$$

We can analytically solve the system of equations given by 2.20 and 2.21 and determine the values of a, b, g and h.

Quantifying the density of each cell type at the rostral end and caudal end of the CND of WT1

Let us now see how to quantify the expressions listed in 2.18 and 2.19 from experimental data.

Step 1: *Estimating the rostral and caudal ends of the apoptotic gradient.*
The values of the average apoptotic gradient are given in Figure 2.9. If the length of the CND is denoted by L, then the theoretical apoptotic gradient is the linear function obtained from the linear regression done on the average apoptotic gradient. This corresponds to the grey curve of Figure 2.13. Let $g(x)$ be this linear function (grey curve of Figure 2.13) and set $g_R := g(0)$ (if $g(0) < 0$, we set $g_R = 0$) and $g_C := g(L)$. The quantities g_R and g_C correspond to the values of the theoretical apoptotic gradient at the rostral and caudal ends of the CND, respectively. In the mathematical framework described in Section 2.2.5, g_R is the value of the gradient at $x = -L(t)$ and g_C is the value of the gradient at $x = 0$. The two values g_R and g_C are independent of the length of the CND L. From the grey curve of Figure 2.13, one can infer that $g_C = 43.2$ and $g_R = 8.9$

Step 2: *Determining a, b, g and h from g_R and g_C.*
As explained previously, to determine the values of a, b, g and h, it is sufficient to deter-

mine the values of

$$\frac{\rho_N}{\rho_T}(-L(t)), \quad \frac{\rho_P}{\rho_T}(-L(t)), \quad \frac{\rho_N}{\rho_T}(0), \quad \frac{\rho_P}{\rho_T}(0).$$

In order to understand the following calculation, one must keep in mind that the units of ρ_N, ρ_P and ρ_T are volume fraction per unit length.

We will initially show the detailed steps used to determine the values of

$$\frac{\rho_N}{\rho_T}(-L(t)) \qquad \text{and} \qquad \frac{\rho_P}{\rho_T}(-L(t)),$$

which represent the percentages of total volume fraction occupied by Normal cells and Phagocytes, respectively, at $x = -L(t)$.

To do so, we first recover the percentage of cells in each stage at $x = -L(t)$, denoted by p_A, p_{E_I}, p_{L_I} and p_D, using the following formula

$$p_i = [\% \text{ given by stationary distribution for state } i] \times g_R \times 0.01, \tag{2.22}$$

where the stationary distribution is shown in Figure 2.5, for i = A, E_I, L_I and D. One should keep in mind that each cell in one of the EI, LI or D state is in a Phagocyte. Also, Normal cells occupy a volume fraction of 1, Phagocytes occupy a volume fraction of 1.2 and apoptotic cell bodies being extruded occupy a volume fraction of 0.2. Let p_N and p_P denote the percentages of cells in the Normal and Phagocyte states respectively.

Let v_N, v_P and v_A denote the volume fraction of cells in the states of Normal, Phagocyte and Apoptotic cell body being extruded, respectively. It follows that

$$v_A = 0.01 \times p_A \times 0.2 \times T \tag{2.23}$$

$$v_P = 0.01 \times (p_{EI} + p_{LI} + p_D) \times 1.2 \times T. \tag{2.24}$$

where T is the total number of cells. Since $1 = p_A + p_{EI} + p_{LI} + p_D + p_N + p_P$, we conclude that the volume fraction occupied by the Normal cells is given by

$$v_N = 0.01 \times p_N \times T = [1 - (p_A + p_{EI} + p_{LI} + p_D + p_P)] \times T = 0.01 \times [1 - g_R - p_P] \times T. \tag{2.25}$$

It follows that

$$\frac{\rho_N}{\rho_T}(-L(t)) = \frac{v_N}{v_N + v_A + v_P} \tag{2.26}$$

$$\frac{\rho_P}{\rho_T}(-L(t)) = \frac{v_P}{v_N + v_A + v_P}. \tag{2.27}$$

By applying the same procedure with g_C instead of g_R, one can determine the values of $\frac{\rho_N}{\rho_T}(0)$ and $\frac{\rho_P}{\rho_T}(0)$.

As shown in Figure 2.9, the largest standard error of the mean of the apoptotic gradient is 3.05. To investigate the uncertainty due to the apoptotic gradient, we have also ran the model in two different set ups: one with an apoptotic gradient shifted by $+3.05$ (adding 3.05 to the values of g_C and g_R estimated in step 1 of Section 2.2.8), and one with an apoptotic gradient shifted by -3.05 (subtracting 3.05 from the values of g_C and g_R estimated in step 1 of section 2.2.8). Our results reveal that there is around a 10% increase and 13% decrease difference in the value of K_D when applying those two shifts, respectively (Table 5 in the Appendix). As for the heatmaps of the rate of efferocytosis K_A, the qualitative behaviour is kept the same, but the maximum value attained by K_A has increased by around 18% and decreased by around 12%, respectively (Figure 2.14 and Figures 4.4 and 4.5 of the Appendix). The heatmaps of the drifting velocity v, on the other hand, remained almost identical in all cases (Figure 2.15 and Figures 4.4 and 4.5 of the Appendix). Because of these small differences, we have decided to use the average apoptotic gradient (Figure 2.9) in the modeling analysis (an approach that has been also approved by the Bouchard Lab).

2.3 Results

2.3.1 Solving the model analytically using Mathematica

As demonstrated before, the apoptotic gradient is approximated by a linear function with respect to space (section 2.2.8). Since the endpoints of this apoptotic gradient are constants, the slope of the apoptotic gradient increases with time. The rostral endpoint is located at the position $x = -L(t)$ and the caudal endpoint at the position $x = 0$. This means that the values of the terms listed in 2.18 and 2.19 are constants and as explained in Section 2.2.8, those are sufficient to determine the parameters a, b, g and h, which characterize ρ_N and ρ_P.

Let g_R and g_C denote the values of the apoptotic gradient at $x = -L(t)$ and $x = 0$, respectively. The details of how we were able to determine the values of a, b, g and h from the values of g_R and g_c and the stationary distribution, were given in Section 2.2.8. The key thing to remember is that they are all functions of g_R and g_C,

$$\begin{aligned} &a = a(g_R, g_C), \qquad b = b(g_R, g_C), \qquad g = g(g_R, g_C) \\ &h = h(g_R, g_C) \end{aligned} \tag{2.28}$$

Below, we outline the different steps implemented to quantify each aspect of the model analytically.

Step 1: *The cellular drift (advection) velocity* $v(x, t)$

ρ_N and ρ_P are functions of a, b, g and h, the spatial variable x and the length of the CND L. So far, we know the values of a, b, g and h but we have not characterized $L(t)$ yet. Given that ρ_N and ρ_P are only functions of x and L, it follows that equation 2.9 is an ODE. By solving this ODE for v, we obtain an expression of v that depends on x, L, c, d and K_D of the form $v = f(x, L, c, d, K_D) + c_1$, where $f(0, L, c, d, K_D) = 0$ and c_1 is a constant. With the boundary condition $v(0) = 0$, we set $c_1 = 0$. This produces an expression for v that depends on x, L, c, d and K_D, given by

$$\begin{aligned}
v &= v(x, L, c, d, K_D). \\
&= \frac{x\left(\left(\left(-1.72 \times 10^{-1}\right) d - \left(1.29 \times 10^{-1}\right) K_D + 1.51 \times 10^{-1}\right) L^2\right)}{L^2} \\
&+ \frac{x\left(\left(\left(8.60 \times 10^{-2}\right) c + \left(2.56 \times 10^{-1}\right) d - \left(5.51 \times 10^{-2}\right) K_D - 2.02 \times 10^{-4}\right) xL - \left(1.71 \times 10^{-1}\right) cx^2\right)}{L^2}
\end{aligned} \tag{2.29}$$

Step 2: *The length of the CND $L(t)$*

By solving the ODE in equation 2.15 along with the initial condition $L(0) = 306\ \mu m$ (length obtained experimentally, Figure 2.3), we obtain an expression for $L(t)$ that depends on time t, c, d and K_D, as follows

$$\begin{aligned}
L &= L(t, c, d, K_D) \\
&= 3.06 \times 10^2 \exp\left[\left(\left(-2.57 \times 10^{-1}\right) c - \left(4.27 \times 10^{-1}\right) d - \left(7.38 \times 10^{-2}\right) K_D + 1.52 \times 10^{-1}\right) t\right]
\end{aligned} \tag{2.30}$$

Using equation 2.30 and applying the boundary condition $L(1) = 153\ \mu m$ (length obtained experimentally, Figure 2.3), we can find an expression for c that depends on d and K_D, as follows

$$\begin{aligned}
c &= c(d, K_D) \\
&= -1.67d - \left(2.88 \times 10^{-1}\right) K_D + 3.30
\end{aligned} \tag{2.31}$$

By substituting the value of c, given by equation 2.31, into 2.30, the expression for $L(t)$ simplifies to

$$L(t) = 306e^{-ln(2)t}. \tag{2.32}$$

Step 3: *The rate of efferocytosis* $K_A(x,t)$

Using equation 2.4 and solving the boundary condition $K_A(-L(t),t) = 0$, we obtain

$$d = -c. \tag{2.33}$$

Substituting d by $-c$ in equation 2.31 and isolating c, we obtain

$$c = \left(4.31 \times 10^{-1}\right) K_D - 4.93. \tag{2.34}$$

Using equations 2.34, 2.33 and 2.32, equations 2.29 and 2.4 become

$$\begin{aligned} v =& v(x,t,K_D) \\ =& x \left(e^{1.39t}\left(8.98 \times 10^{-6} - \left(7.85 \times 10^{-7}\right) K_D\right) x^2 + e^{ln(2)t}\left(2.74 \times 10^{-3}\right.\right. \\ & \left.\left. - \left(4.19 \times 10^{-4}\right) K_D\right)x - \left(5.48. \times 10^{-4}\right) K_D - 6.97 \times 10^{-1}\right) \end{aligned} \tag{2.35}$$

and

$$\begin{aligned} K_A &= K_A(x,t,K_D). \\ &= \left(\left(4.31 \times 10^{-1}\right) K_D - 4.93\right)\left(\left(-3.27 \times 10^{-3}\right) e^{ln(2)t} x - 1.\right) \end{aligned} \tag{2.36}$$

Step 4: *Quantifying* K_D*,* K_{EI}*,* K_{LI} *and* K_G

Substituting equations 2.36, 2.16, 2.17 and 2.32 into equation 2.13 and solving for K_D, we obtain

$$K_D = 2.70 \quad days^{-1}. \tag{2.37}$$

By substituting equations 2.6 and 2.7 into equation 2.5 and using the fact that $K_D = 2.70$, we can solve for K_{EI}. Once we know the value of K_{EI}, we can then plug its value back into equations 2.6 and 2.7 to determine the values of K_{LI} and K_G.

Step 5: *Determining the analytical expressions of* $v(c,t)$, $K_A(x,t)$, $K_P(x,t)$ *and* $K_{BX}(x,t)$
By substituting $K_D = 2.70$ into equations 2.35 and 2.36, we obtain the spatiotemporal analytical expressions of $v(x,t)$ and $K_A(x,t)$, given by

$$\begin{aligned} v &= v(x,t) \\ &= x\left(\left(6.86\times10^{-6}\right)e^{1.39t}x^2 + \left(1.60\times10^{-3}\right)e^{ln(2)t}x - 8.45\times10^{-1}\right) \end{aligned} \tag{2.38}$$

and

$$\begin{aligned} K_A &= K_A(x,t). \\ &= 3.77\left(\left(3.27\times10^{-3}\right)e^{ln(2)t}x + 1\right). \end{aligned} \tag{2.39}$$

As explained before, $K_P(x,t) = K_A(x,t)$. Substituting equation 2.39 into equation 2.3, we obtain an analytical expression for K_{BX}, given by

$$K_{BX}(x,t) = 2.62\times10^{-1}\left(\left(3.27\times10^{-3}\right)e^{ln(2)t}x + 1\right). \tag{2.40}$$

2.3.2 Spatiotemporal dynamics insights

By using the stationary cellular distribution of WT1 (Figure 2.5) , apoptotic gradient of WT1 (Figure 2.9), two time points of the length of the CND of WT1 (at E11.5 and E12.5, see Section 2.1), the rate of proliferation K_S (Section 2.1), the fraction of cells not undergoing proliferation f_n (Section 2.1), the fraction of volume lost by a cell through water release during apoptosis ($1-f_e$) as experimental data (Section 2.2.4) along with the derivations detailed in Sections 2.2.8 and 2.3.1, we were able to derive analytical expressions for the spatiotemporal variables $K_A(x,t)$, $K_P(x,t)$, $K_{BX}(x,t)$ and $v(x,t)$ (heatmaps plotted in Figure 4.1 of the Appendix), the temporal variable $L(t)$ and to determine the value of the rate constants K_D, K_{EI}, K_{LI} and K_G (values given in Table 1).

Dwell time of each stage of non-professional phagocytosis

Table 1: List of parameters and their estimated values of WT1.

Symbol	Description	Value	Unit	Duration of associated process per cell
K_D	Digestion rate	2.70	day^{-1}	8.89 hours
K_{EI}	Early internalization rate	32.5	day^{-1}	44.3 minutes
K_{LI}	Late internalization rate	5.12	day^{-1}	4.69 hours
K_G	Degradation rate	6.94	day^{-1}	3.46 hours
K_S	Proliferation rate	24/18	day^{-1}	18 hours

The value of K_S was known experimentally (see Section 2.1). The other rate constants were obtained using the model, as explained above. Once we have retrieved a rate constant, its reciprocal gives the duration of the associated process. For example, the digestion time is given by $1/K_D = 8.89$ hours (see Table 1). This argument also holds for K_{EI}, K_{LI}, K_G and K_S. We can thus conclude that the time it takes for one Phagocyte to digest an engulfed cell is 8.89 hours, which falls into a reasonable biological range (as confirmed by the Bouchard Lab that was expecting a value between 8h and 12h).

Consistent with the low number of experimental observations of these stages, the time of Early internalization has been found to be in a shorter time scale (44.3 min) (Figure 2.5). Conversely, the Late Internalization and Debris stages of efferocytosis were found to be slow processes, occurring in a time scale of hours (4.69 hours and 3.46 hours, respectively) (Figure 2.5). These dwell times, which could NOT be measured in vivo, provide an insight into the timeline of efferocytosis by CND epithelial cells and can assist in pinpointing where pathologies occur when comparing their values to disease conditions.

The role of efferocytosis and drifting velocity

For WT1, it was determined by the Bouchard Lab that the length of the CND at t=0 days (E11.5) is 306 μm and at t=1 days (E12.5) is 153 μm (Figure 2.3), which we used as boundary conditions to the model. By following the derivations outlined in Section 2.3.1, an analytical expression for $L(t)$ is obtained in the form of an exponential decay with a decay constant equal to $ln(2)$ (see Figure 2.16, orange plot). This means that the CND loses half of its length on a daily basis.

To understand how the rate of efferocytosis $K_A(x,t)$ and cellular velocity $v(x,t)$ vary spatially and temporarily during this progressive decay in the length of the CND, we plot in Figure 2.14 and Figure 2.15 the heatmaps of these variables with respect to time and length of the CND. The time variable (vertical axis) in these heat-maps represents the duration between $t = 0$ days (E11.5) until $t = 2$ days (E13.5), whereas the spatial variable (horizontal axis) corresponds to the length of the CND, extending from $x = -L$ (the rostral end of the CND at the ureter-nephric duct connection point) all the way to $x = 0$ (the caudal end where the CND connects to the bladder).

Figure 2.14 shows that, during the progressive decline of CND length, the rate of efferocytosis K_A increases along the CND toward the caudal region of the CND at each time point; this is an expected outcome in view of the assumptions we made on $K_A(x,t)$ in equation 2.4 and the profile of the apoptotic gradient (Figure 2.9). This profile suggests that apoptosis via efferocytosis is far more dominant in the region adjacent to the bladder than in the rostral region. It reflects the fact that the rate of efferocytosis follows a similar gradient as the apoptotic gradient.

In contrast, Figure 2.15 shows that the heatmap of the velocity along the shrinking CND exhibits a behavior opposite to that for K_A. In this case, the heatmap shows that, at each time point, the velocity of the cells decreases monotonically (it follows a cubic decrease as highlighted by equation 2.29) toward the bladder until reaching a velocity of zero when touching the bladder. Having $v = 0$ at the caudal end is to be expected since there is no cell movement beyond the bladder, which is why we used that condition to constrain the model. The higher velocity at the rostral end is also to be expected, given that the

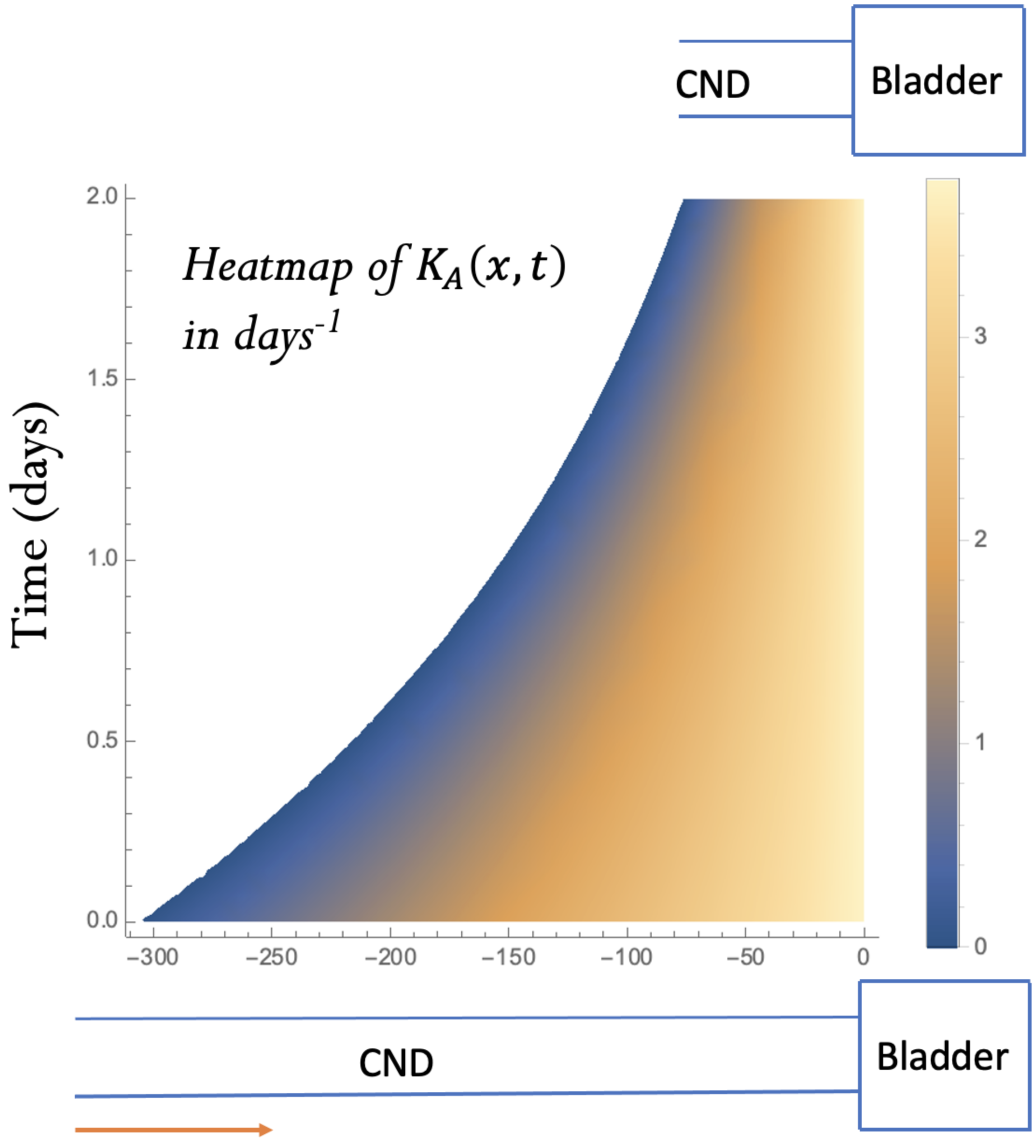

Figure 2.14: The heatmap of the rate of efferocytosis (K_A) in $days^{-1}$ along the CND with respect to time (horizontal axis) and length of the CND (vertical axis). The heat-maps is color-coded according to the color-bars to the right. Notice how the length of the CND gradually shrinks exponentially.

death rate in the caudal region is higher, forcing other cells of the CND to move toward the caudal region to compensate for the loss in volume. This means that if a cell is far away from the bladder, it has to travel faster to replace dead cells. This velocity gradually decreases at the caudal end as the CND shrinks and the number of apoptotic cells driving cell movement decreases (see Figure 2.15).

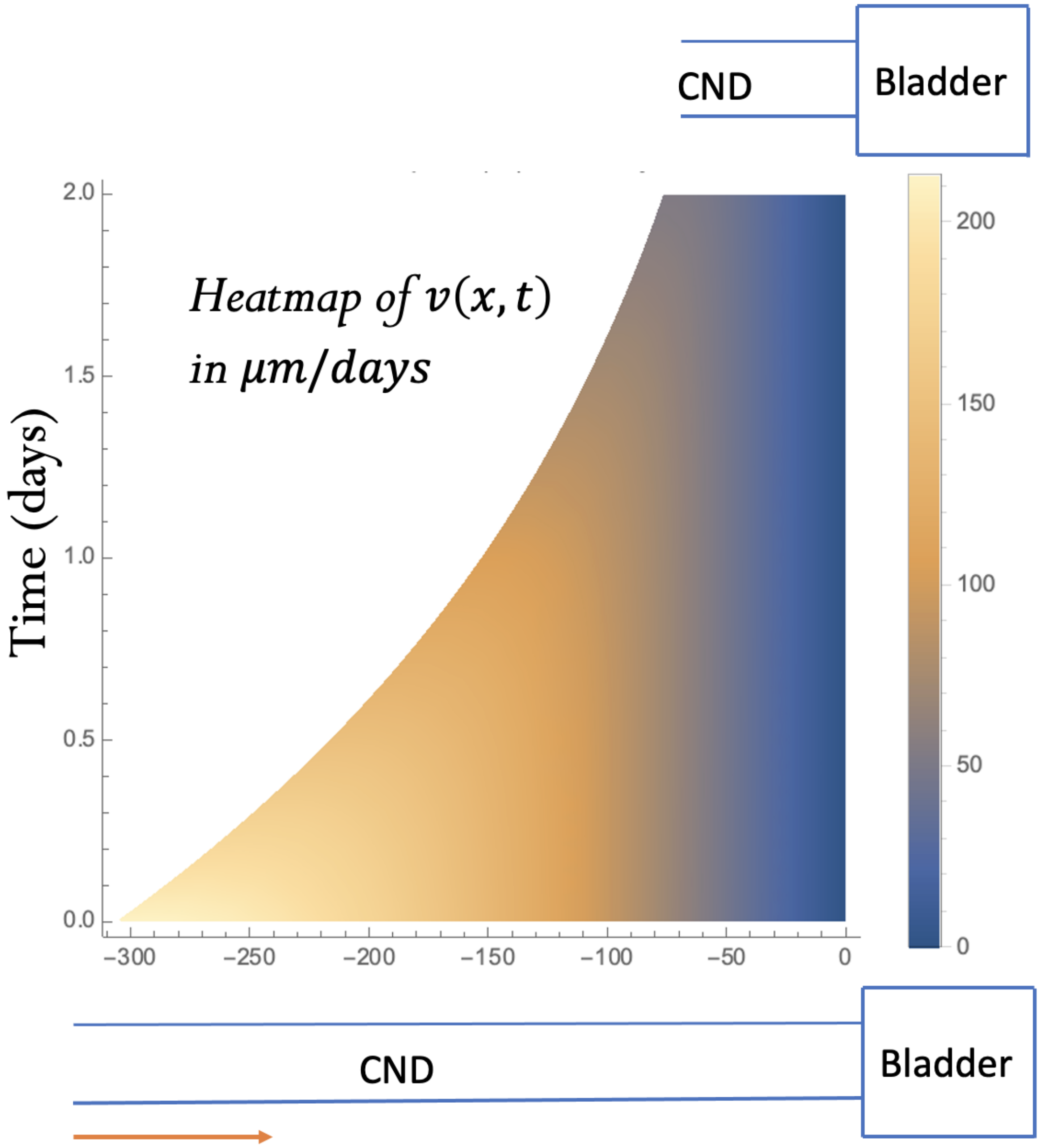

Figure 2.15: The heatmap of the cellular velocity v along the CND in $\mu m/days$ with respect to time (horizontal axis) and length of the CND (vertical axis). The heat-map is color-coded according to the color-bars to the right. Notice how the length of the CND gradually shrinks exponentially.

2.3.3 Contribution of efferocytosis and basal extrusion to CND shortening

We have previously analyzed the dynamics of the model when all the components involved in CND shortening/elongation are included (efferocytosis, basal extrusion and proliferation). Now that we have constrained our model with experimental data and that the model produced outcomes are consistent with those observed experimentally, we can now use it to perform tasks that CANNOT be done experimentally. Our goal is to explore how the system behaves when one single component is present versus when a combination of them is present (i.e., examine the contribution of these components individually and in combination). Let us use the model to quantify the role of each component (Proliferation (P), Efferocytosis (E) and Basal Extrusion (BX)) individually and in combination in the CND shrinkage/elongation. In the WT1 model, the total volume fraction eliminated between $t = 0$ and $t = T$ days is given by

$$V_{Tot}(T) = \int_0^T \int_{-L(t)}^0 f_n((1 - f_e)K_A + K_{BX})\rho_N + \frac{f_e}{1 + f_e} K_D \rho_P \, dxdt. \tag{2.41}$$

The volume fraction eliminated between $t = 0$ and $t = T$ days by efferocytosis (V_E) and by basal extrusion (V_{BX}) are given by, respectively,

$$V_E(T) = \int_0^T \int_{-L(t)}^0 f_n(1 - f_e)K_A \rho_N + \frac{f_e}{1 + f_e} K_D \rho_P \, dxdt \tag{2.42}$$

and

$$V_{BX}(T) = \int_0^T \int_{-L(t)}^0 f_n K_{BX} \rho_N \, dxdt \tag{2.43}$$

with $V_{Tot} = V_E + V_{BX}$. Therefore, the percentages of cell clearance through efferocytosis and basal extrusion are given by $\frac{V_E}{V_{Tot}}100$ and $\frac{V_{BX}}{V_{Tot}}100$, respectively. It is interesting to point out here that these ratios do not depend on T.

The data from the Bouchard Lab shows that much more cells are undergoing efferocytosis than basal extrusion (Figure 2.5). Since the measurements were done at two specific time points, they do not tell us anything about the time scales of these two processes (efferocytosis and extrusion) and how they interact collectively over extended periods of time. The multiscale model developed in this thesis allows us to quantify the overall contribution of each process to the CND shrinkage over time and account for the time scales of each process (the experimental data alone cannot do so). Using equations 2.41, 2.42 and 2.43, we can conclude that cell processing through efferocytosis and basal extrusion represent $\frac{V_E}{V_{Tot}}100 = 93.8\%$ and $\frac{V_{BX}}{V_{Tot}}100 = 6.2\%$ of the CND elimination, respectively. This suggests that efferocytosis is the main driver of the CND shortening.

To validate this further, we investigated the evolution of the length of the CND in different conditions in Figure 2.16 using the method developed below.

The WT1 model accounts three crucial components: Proliferation (P), Efferocytosis (E) and Basal Extrusion (BX). The volume fraction added by proliferation between $t = 0$ and $t = T$ days is given by

$$V_P(T) = \int_0^T \int_{-L(t)}^0 (1 - f_n) K_S(\rho_N + \rho_P)\, dxdt. \tag{2.44}$$

We can conclude that the overall volume fraction change between $t = 0$ and $t = T$ days is given by $V_P(T) - V_E(T) - V_{BX}(T)$. To convert this volume fraction change into a change in CND length, ℓ_c we simply have to divide the latter by ρ_T, i.e.

$$\ell_c = \frac{V_P - V_E - V_{BX}}{\rho_T} \tag{2.45}$$

which gives the change in CND length at $t = T$ days. If this quantity is positive (negative), it means that the CND length has decreased (increased). For WT1, if we substitute $T = 2$ days into equation 2.45, we find that $\ell_c = 229.5$, which is to be expected because the length of the CND decreased from $306\ \mu m$ at $t = 0$ days to $76.5\ \mu m$ at $t = 2$ days. Naturally, the expression the length of the CND at $t = T\ days$,$L(T)$, can be expressed as

$$L(T) = 306 - \frac{V_P(T) - V_E(T) - V_{BX}(T)}{\rho_T} \tag{2.46}$$

and this matches the expression given by equation 2.32.

Using this framework, we can predict the effect of inhibiting different components involved in determining the length of the CND. For example, the evolution of CND length without basal extrusion L_{P+E} is given by

$$L_{P+E}(t) = 306 - \frac{V_P(t) - V_E(t)}{\rho_T}. \tag{2.47}$$

Similarly, we can define the following temporal variables

$$L_{P+BX}(t) = 306 - \frac{V_P(t) - V_{BX}(t)}{\rho_T}, \tag{2.48}$$

$$L_{E+BX}(t) = 306 - \frac{-V_E(t) - V_{BX}(t)}{\rho_T}, \tag{2.49}$$

$$L_P(t) = 306 - \frac{V_P(t)}{\rho_T}, \tag{2.50}$$

to describe the combined contribution of proliferation and basal extrusion, of efferocytosis and basal extrusion, and finally of proliferation alone. $L_P(t)$, $L_{P+BX}(t)$, $L_{P+E}(t)$, $L(t)$ and $L_{E+BX}(t)$ are plotted in purple, brown, blue, orange and black, respectively, in Figure 2.16.

As expected, proliferation causes an elongation of the duct (purple curve) and basal extrusion is not strong enough to counter the elongation caused by proliferation (brown curve). When only basal extrusion is removed, the shrinkage of CND is almost identical to when all components of the model are included (the blue curve is very close to the orange curve). This once again shows that efferocytosis is the main driver of the CND shrinkage and that basal extrusion merely contributes to the shrinkage of the CND.

As highlighted by the Bouchard Lab, the insightful conclusions provided by the model are hard or even impossible to verify experimentally. This is the very reason why we have used multiscale mathematical modeling approaches (adopted from nonlinear dynamics and complex systems) to fill out the gaps left out by the experimental work, an approach used routinely in the field. At best, one could try to verify our predictions using cell culture experiments. However, this would require different cell types and conditions for

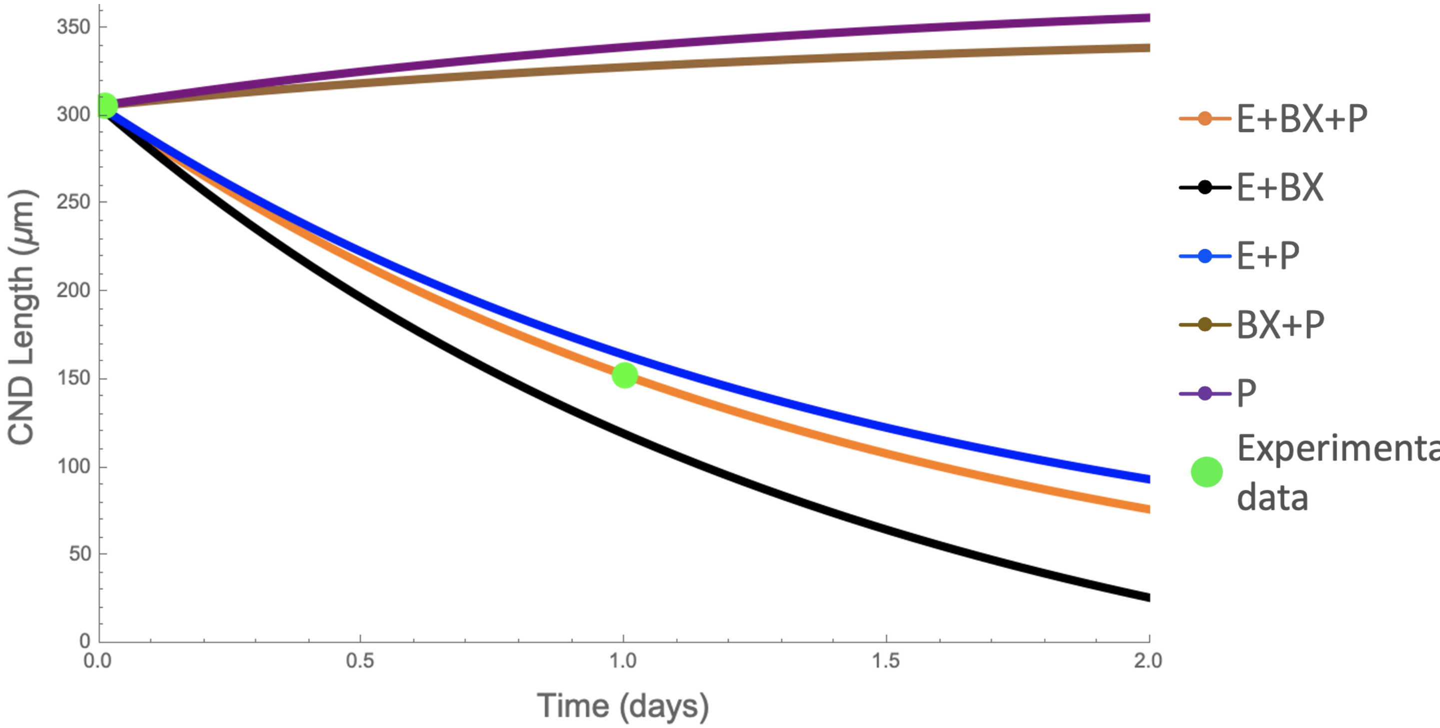

Figure 2.16: The time evolution of the length of the CND in different conditions as determined by model. These conditions include: the contribution of cell proliferation alone (purple curve), the contributions of both basal extrusion and cell proliferation only (brown curve), the contributions of both cell proliferation and efferocytosis only (blue curve), the contributions of both basal extrusion and efferocytosis only (black curve) and the contributions of proliferation, basal extrusion and efferocytosis combined (orange curve). Notice how similar the blue and orange curves.

cells to grow outside the embryos that are no longer consistent with the framework of the multiscale model.

2.3.4 How parameter perturbations affect model outcomes

Fixed values of f_e, L_0 (length of the CND at $t = 0$ day), L_1 (length of the CND at $t = 1$ day), g_C and g_R were previously used to constrain the WT1 model. Since the Bouchard Lab has been greatly interested in estimating the digestion time $1/K_D$ associated with the WT1 model (determined in Section 2.3.2), it would be interesting to investigate how perturbations in these former parameters affect the rate of digestion (K_D) in the model (while keeping data associated with CND shortening unchanged). For example, if the apoptotic gradient was different, then what value of K_D would be necessary to match the rest of the experimental data. Since from a biological point of view, there is no reason for K_D to change, we realize that this does not imply that digestion and apoptotic gradient are dependent on each other; it just implies that they are both at play.We still perform this analysis to test how this is manifested according to the model.

Varying L_0 and L_1

By applying the steps of Section 2.3.1 with L_0 and L_1 left as a non fixed parameters, we obtain the following expression for K_D

$$K_D = 1.54 + 1.67ln\left(\frac{L_0}{L_1}\right). \tag{2.51}$$

According to equation 2.51, we can conclude that K_D increases as L_0 increases or as L_1 decreases. Since $L_0 > L_1$, it follows that K_D increases as the difference $L_0 - L_1 > 0$ increases. This is to be expected since an increase in $L_0 - L_1 > 0$ implies that the CND length shrinks more in the same amount of time, which requires a faster efferocytosis process and hence a faster digestion.

Varying g_C and g_R

After following the steps of Section 2.3.1 with g_C or g_R left as non fixed parameters, we plot K_D against each of these parameters in Figure 2.17.

Based on Figure 2.17, we can conclude that K_D decreases as g_C or g_R increases. If either g_C or g_R increases, the apoptotic gradient becomes bigger, which means that more cells are undergoing apoptosis. If more cells are undergoing apoptosis, then the time required for digestion needs to increase in order to maintain the same shrinkage rate. Once again, this is an expected outcomes because if the digestion time were to stay the same, then the shrinkage rate would not remain fixed.

Varying f_e

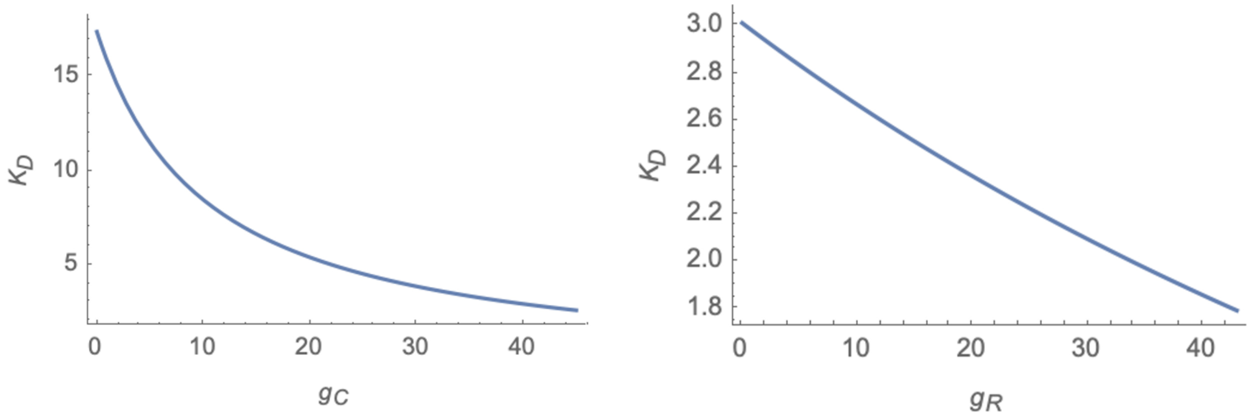

Figure 2.17: On the left: K_D as a function of g_C with $g_R = 8.9$ (as used in the WT1 model). On the right: K_D as a function of g_R with $g_C = 43.2$ (as used in the WT1 model).

Recall that $f_e \in [0, 1]$ corresponds to the remaining volume fraction of a Normal cell after it has shrunk due to apoptosis. In the WT1 model, when a Normal cell enters apoptosis, 80% of its volume is lost through water release, implying that $f_e = 0.20$. After applying the steps of Section 2.3.1 allowing f_e to vary as a parameter, we can plot K_D against f_e, (see Figure 2.18).

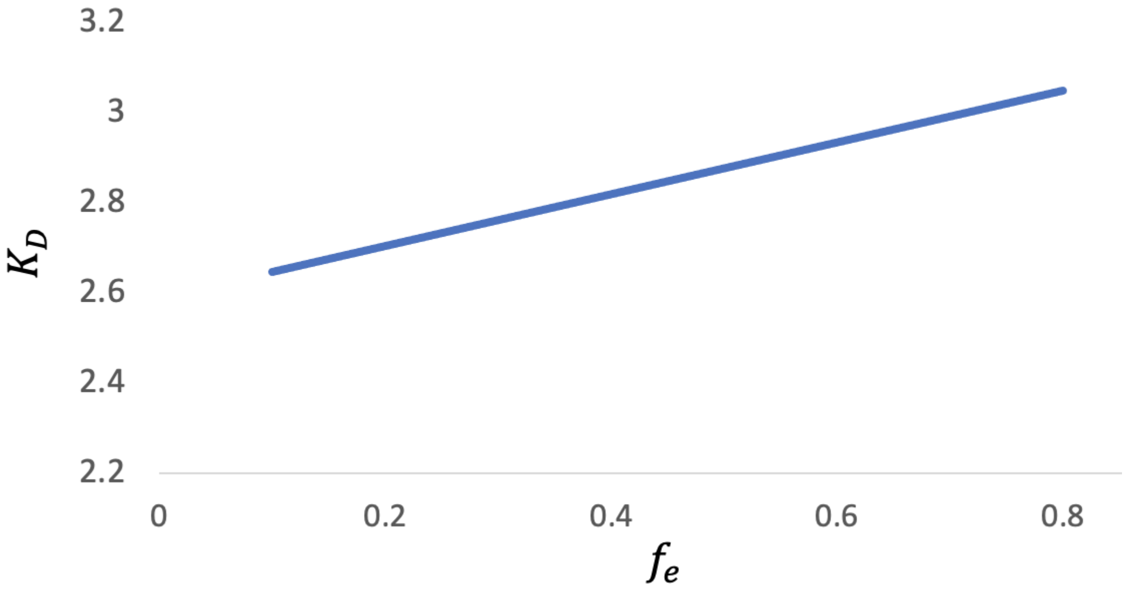

Figure 2.18: K_D as a function of f_e.

The resulting graph reveals that if all the other parameters are held fixed, then increasing

f_e causes K_D to increase. This implies that, as f_e increases, the digestion process becomes slower. This makes sense because as f_e increases, the volume of a Pre-Engulfed cell gets bigger, requiring the system to compensate by getting rid of them at a faster rate to maintain the same rate of CND shrinkage as before. In order to get rid of them faster, the Phagocyte needs to digest them at a faster rate. The latter is made possible by having a higher digestion rate.

As described above, changes in L_0, L_1, f_e, g_C and g_R affect the digestion rate K_D in a physiologically understandable and consistent manner suggested by the model. As mentioned in the Introduction, some studies raised the possibility that the bladder epithelium could be a source of signals inducing the apoptotic gradient along the CND. One could modify experimentally the apoptotic gradient without affecting the digestion time (given by $1/K_D$ in our model) by playing with this signal. Intuitively, a higher apoptotic gradient should accelerate the shortening of the CND and a lower apoptotic gradient should slow down the shortening of the CND. We can investigate this using our model with K_D and L_0 left as fixed parameters and shifting the apoptotic gradient up or down by a percentage Δ (adding Δ to the values of g_C and g_R estimated in Step 1 of Section 2.2.8). The effect on the predicted length at E12.5 (L_1) is plotted in Figure 2.19, and as expected, L_1 shortens as Δ increases. Therefore, according to our model, a higher apoptotic gradient accelerates the shortening of the CND and a lower one slows it down.

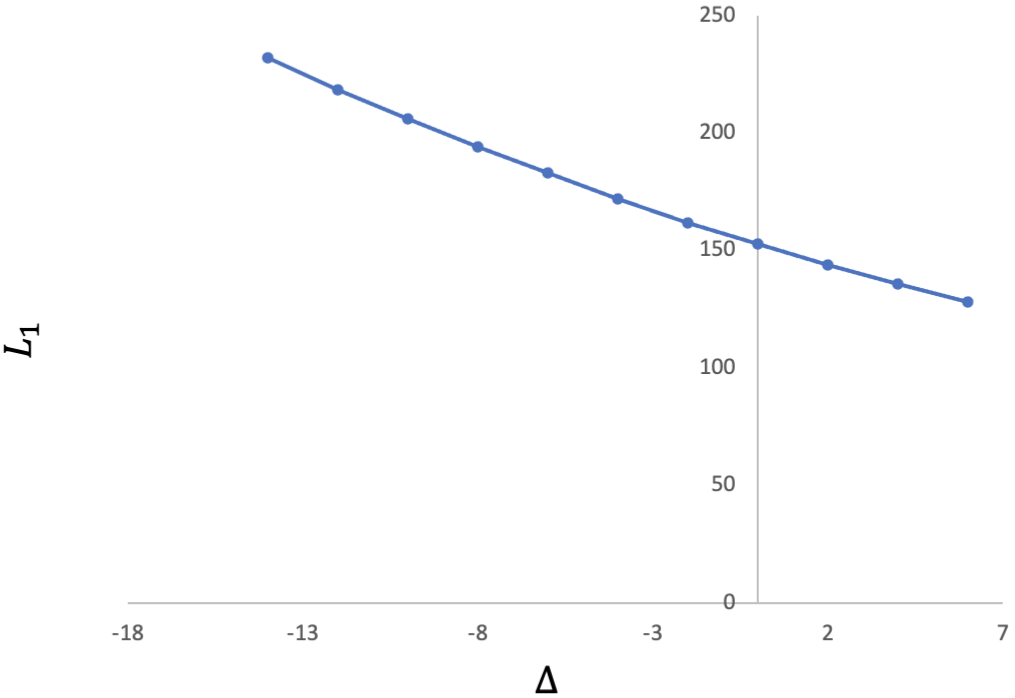

Figure 2.19: L_1 as a function of Δ.

Chapter 3

Ex vivo model: Blebbistatin treatment

3.1 Experimental data

To assess the role of actomyosin in the shortening of the CND, ex vivo experiments in the Bouchard Lab (McGill University) were conducted. These included CNDs that were treated with Blebbistatin (an actomyosin inhibitor) as well as those that were not. The latter will be called "Control CND" hereafter. We cannot use the experimentally observed apoptotic gradient and stationary distribution of the ex vivo CNDs in both conditions because the data was not solid enough to be included. The length of the Control and Blebbi-treated CNDs was measured at six different time points as shown in Table 2. For the Blebbi-treated CNDs, Blebbistatin treatment was initiated at E11.5 ($t = 0\ h$); such treatment caused several changes to CND dynamics compared to those observed in WT1 CNDs, including a decrease in CND radius and lumen radius, an increase in cell volume and an enhancement of apical extrusion (see Figure 3.1). It is important to point out here that the extrusion observed in WT1 (Section 2.1) happens only on the basal side whereas in Blebbi-treated CNDs, extrusion happens on the basal side and on the apical side simultaneously. Basal extrusion follows a gradient but apical extrusion in Blebbi-treated CND is constant along the CND and affects 4.2% of the cells 48 h after the start of the Blebbistatin treatment (E13.5). The radii of the Blebbi-treated CND and lumen were measured at $t = 48$ h and compared to that of Control CND and lumen; the results were as follows: CND radius of $37.35\ \mu m$ for Control vs $27.20\ \mu m$ for Blebbi-treated and lumen radius of $13.7\ \mu m$ for Control vs $12.4\ \mu m$ for Blebbi-treated (see Figure 3.2). Finally, it was also revealed experimentally that cell volume increased by 32% on average at $t = 48\ h$ in the Blebbi-treated CND compared to Control CND (see Figure 3.3).

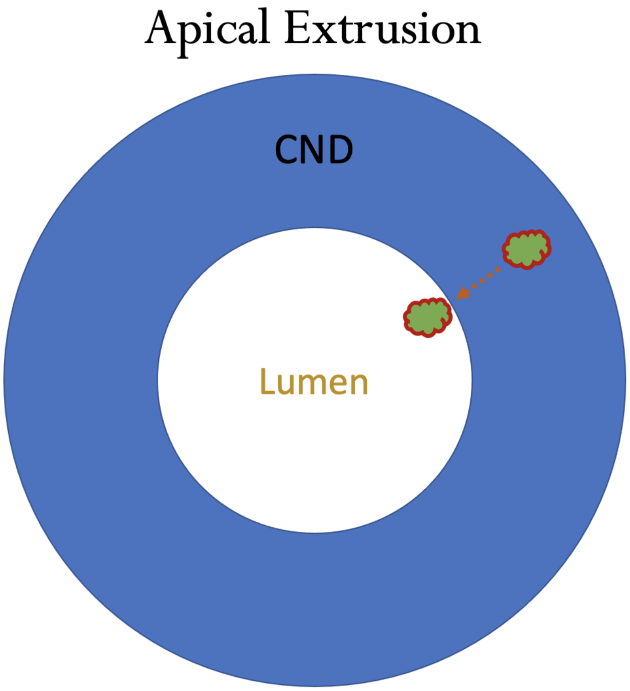

Figure 3.1: A cross-section of the process of apical extrusion, during which apoptotic cells are being pushed toward the lumen of the CND. Unpublished data from the Bouchard Lab indicate that an average of 4.2% (SEM of 1.5%) of cells in Blebbistatin-treated CND and an average of 0.4% (SEM of 0.5%) of cells in Control CND undergo apical extrusion (data obtained with n=3 embryos for each condition). The p-value was calculated using two tailed t-tests and was found to be smaller than 0.05.

3.2 Mathematical Model and Derivations

3.2.1 Ex vivo Control CND

As explained in Section 3.1, we cannot use the experimentally observed apoptotic gradient and stationary distribution of the ex vivo CNDs. Larger cell volume in Blebbi-treated CNDs may affect a bit the phagocytic process, but all in all it should be in the same range as in the Control CND. This follows from the fact that the phagocytic vesicle fuses with

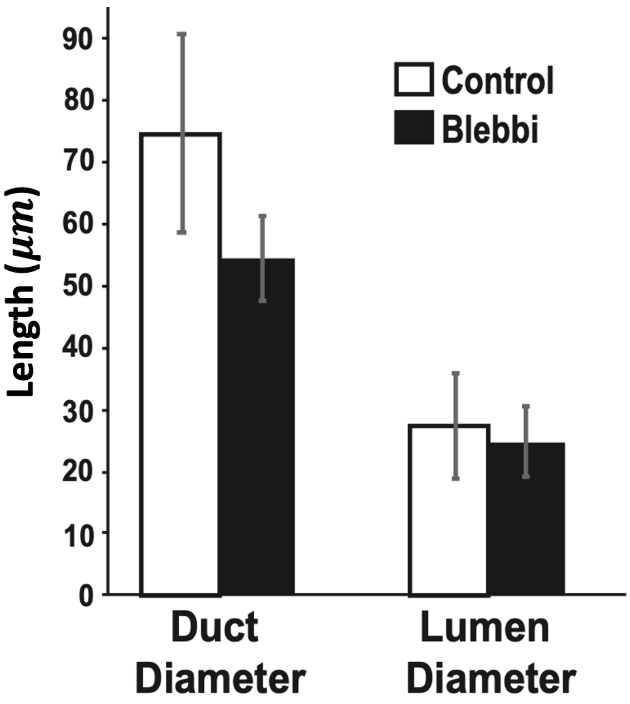

Figure 3.2: Unpublished data from the Bouchard: duct diameter and lumen diameter. Data presented as mean ± SEM. N= 3 embryos, 15-20 sections for each embryo for control and Blebbistatin treatment. P-values were calculated using two-tailed t-tests for each of the CND radius and lumen radius and were found to be smaller than 0.01 for the former and non significant for the latter. The figure was produced by Emily Tang, Phd candidate in the Bouchard Lab.

lysosomes (vesicles containing enzyme capable of breaking down various biomolecules it engulfs) which digests the content independently of phagocytic vesicle size. Furthermore, the Bouchard Lab has obtained some quantification of the stationary distribution of Blebbi-treated ducts but the data were too few to be meaningful for solid enough interpretations of the results. The only conclusion that could be made is that the Late Internalization was not affected at all in Blebbi-treated CNDs while the Debris was reduced but not significantly (statistically speaking). This final outcome was consistent with the expectation of the Bouchard Lab, as they saw no reason for the time duration of the Debris stage to be affected, given that actomyosin plays no role in lysosome function. Based on this and the recommendation made by the Bouchard Lab, we have decided to assume here that the Blebbi-treated CND and the Control CND have the same stationary distri-

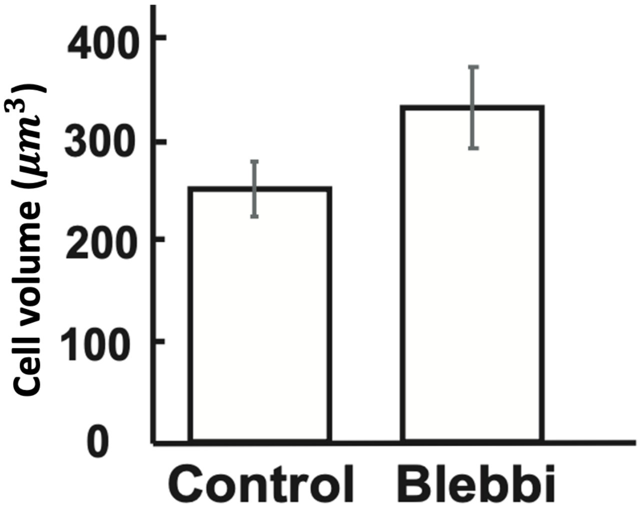

Figure 3.3: Unpublished data from the Bouchard: cell volume of Blebbistatin treated CND cultures. Data presented as mean ± SD. N=103 cells for control and n=149 cells for Blebbistatin treatment. The p-value was calculated using two-tailed t-test and was found to be smaller than 0.05. The figure was produced by Emily Tang, Phd candidate in the Bouchard Lab.

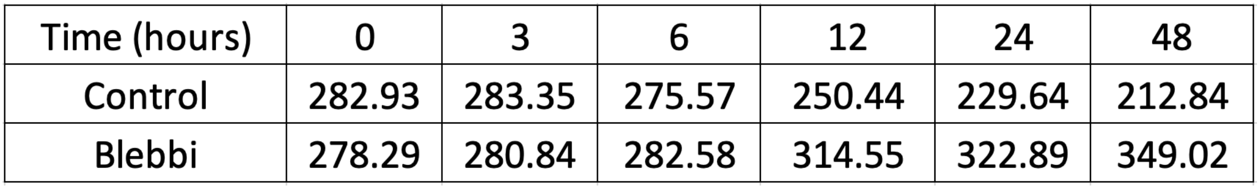

Time (hours)	0	3	6	12	24	48
Control	282.93	283.35	275.57	250.44	229.64	212.84
Blebbi	278.29	280.84	282.58	314.55	322.89	349.02

Table 2: Control CND and Blebbi-treated CND length (in μm) measured at 6 time points. $t = 0\ h$ corresponds to E11.5. For each of Control and Blebbi-treated CND, the data was averaged over 65, 10, 12, 23, 34 and 20 CNDs at 0 h, 3 h, 6 h, 12 h, 24 h and 48 h, respectively. E11.5 UGS from Pax2GFP embryos was dissected and ex vivo cultured to measure CND lengths for each time points. For the Blebbi-treated conditions, 100uM Blebbistatin is added to the DMEM medium in the culture.

bution as WT1.

As mentioned in the previous section, the apoptotic gradient can be used to constrain the model and estimate the unknown parameters (including the digestion rate K_D) in the in vivo WT case, but for the ex vivo CNDs, we cannot do so as no evidence suggests that the apoptotic gradient is maintained in this latter case. On the other hand, as mentioned in the above paragraph, it is physiologically reasonable to assume that the ex vivo rate of digestion K_D is in the same range as that for the in vivo case because Late Internalization and Debris, the two main stages of digestion (see Figure 2.5), do not seem to be affected by actomysoin. Since we do not have experimental data to estimate the ex-vivo apoptotic gradient, we will generate a "theoretical ex vivo apoptotic gradient" by using the assumption that the in-vivo and ex-vivo digestion times and stationary distributions are the same to constrain the model. The details of how this is done can be found in the next subsection. To help facilitate understanding of the computational steps detailed here in later sections, we will use the word "input" to describe those experimental data that are employed to constrain (i.e., parameterize) the model and use the word "output" to describe the parameters that are estimated by the model.

Based on this terminology, it follows that with the theoretical ex vivo apoptotic gradient along with the other usual input data (described in chapter 2), we obtain the "Control model".

Predicting the theoretical ex vivo apoptotic gradient

As explained earlier, we wish to take the length of the Control CND at E11.5 and E12.5 and the stationary distribution of WT1 as inputs to parameterize the model, and then determine what values g_R and g_C must attain to obtain the same K_D as in WT1.

In our WT1 model, the analytical expression obtained for the CND length was an exponential decaying curve (see Step 2 of Section 2.3.1). As described in Section 3.1, the length of the Control CND was measured at 6 different time points: 0 h, 3 h, 6h, 12 h, 24 h and 48 h. To parameterize the model according to this Control CND data, we need two specific times points to do so, namely, E11.5 ($t = 0$ h) and E12.5 ($t = 24$ h) (just like we did in the WT1 model); by taking advantage of data available at the the six time points, one can generate better estimates of the control CND length at E11.5 and E12.5. To do so, we first fit an exponential curve to CND length at these six times points (blue curve of

Figure 3.4, with an R-value bigger than 0.92). This is followed by using the blue curve to determine the length of the CND at $t = 0$ h (E11.5) and $t = 24$ h (E12.5). This produces the lengths: $280.68\ \mu m$ and $240.86\ \mu m$, respectively. These values are then used as inputs to parameterize the Control model. Obviously any other two time points along the experiential curve could have been used for model parameterization, but the former two time points, $t = 0$ h and $t = 24$ h, have been picked for the sake of consistency with WT1 model.

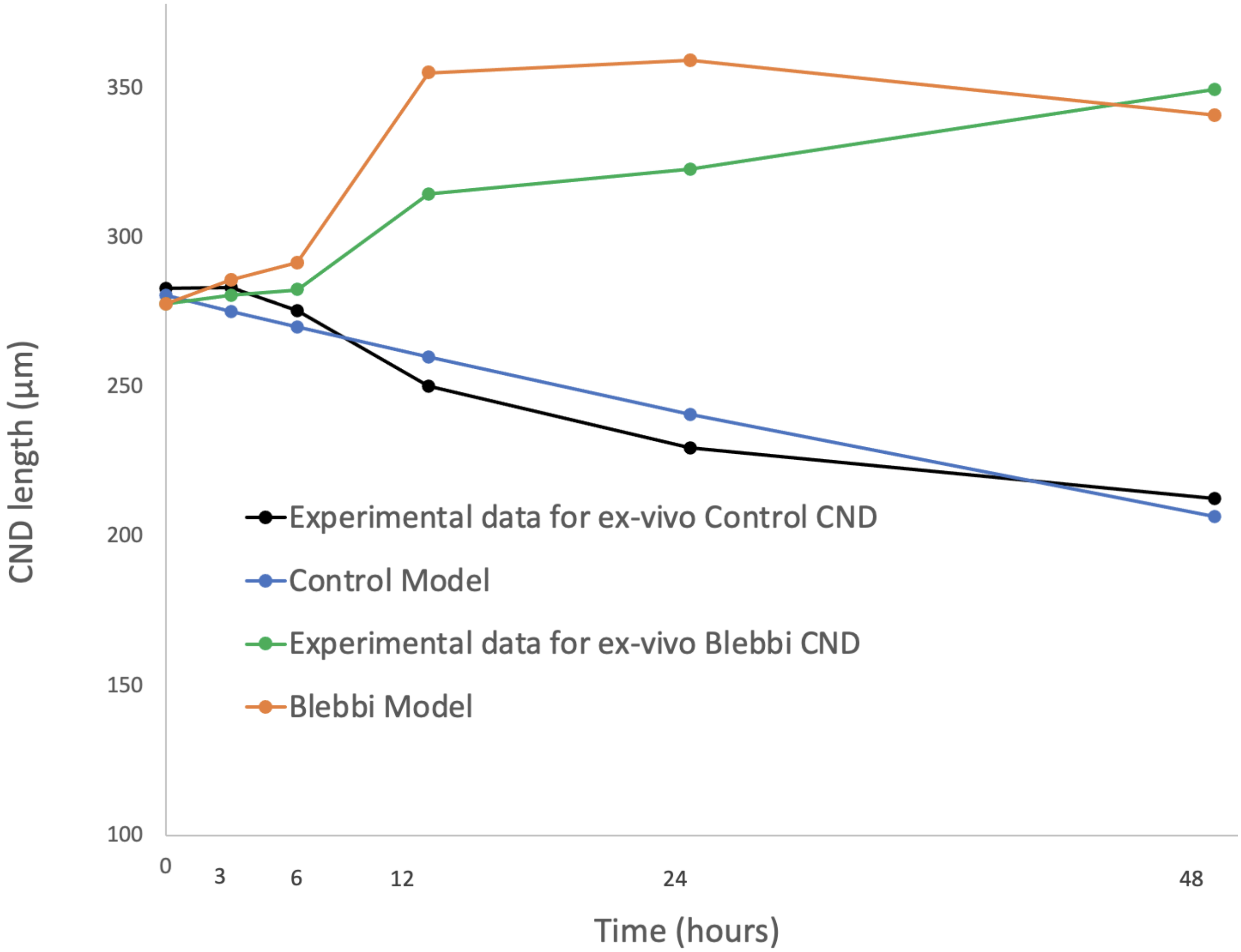

Figure 3.4: The experimental data points for Control CND and Blebbistatin treated CND are plotted in black and green, respectively. The evolution of the length of the CND according to the Control model and Blebbi model are plotted in blue and orange, respectively, and are relatively close to their corresponding experimental data.

Since g_C and g_R are unknowns, we express a, b, g and h as functions of g_C and g_R (equations 2.28). We then follow the steps described in Section 2.3.1. At Step 4, we obtain (unlike before) a relation between K_D, on one hand, and g_C and g_R, on the other, given by

$$K_D = f(g_C, g_R), \tag{3.1}$$

where $f(g_C, g_R)$ is the function shown in Figure 4.7 of the Appendix. For any fixed values of K_D and g_R (or g_C) in $\mathbb{R}$ there exists $g_C \in \mathbb{R}$ (or $g_R \in \mathbb{R}$) such that $f(g_C, g_R) = K_D$. Recall that in the WT1 model, $K_D = 2.70$ and that there exist infinitely many 2-tuples (g_C, g_R) such that $K_D = f(g_C, g_R) = 2.70$. This being said, we still need to determine what g_C and g_R should be to characterize the theoretical ex vivo apoptotic gradient. In order to get a unique pair, we need to fix either g_C or g_R. With recommendations from the Bouchard Lab, we set $g_R = 0$. By doing so, we obtain $g_C = 19.2$. This, as a result, produces a theoretical ex vivo gradient that is linear with 0% apoptosis at $x = -L(t)$ and 19.2% apoptosis at $x = 0$.

3.2.2 Blebbistatin treated CND

We know that Blebbistatin treatment acts in the following ways:

- It reduces CND radius.
- It reduces lumen radius.
- It increases cell volume.
- It enhances apical extrusion.

According to the protocol used in Bouchard Lab, Blebbistatin treatment starts at $t = 0\ h$ and the final effects (mentioned above) are measured at $t = 48\ h$.

In order to add apical extrusion rigorously to our model, we need to employ the multistate model (labeled MS2) shown on Figure 3.5; the framework of this new model is similar to the MS1 model, except for the addition of the rate of apical extrusion K_{AX} and $(1 - f_{ax})$, the fraction of cells being extruded on the apical side. The value of f_{ax} is known experimentally (see Section 3.1) and the value of K_{AX} can be determined from the values of K_{EI} and K_{LI} obtained with the Control model (see the details in next section). The Bouchard Lab recommended that we consider basal and apical extrusion as two independent pathways due to differences in dynamics. Indeed, at any given time point, the rate of basal extrusion increases along the CND toward the bladder while apical extrusion is constant along the CND. To help explain the various transitions of the multistate model of Figure 3.5, the fate of the different cell types have been further elucidated in Figure 3.6. Using this framework, the two extrusion processes, the theoretical ex vivo apoptotic gradient and MS2 model along with the other usual input data, we obtain the "intermediate Blebbi model" (IBM).

Reductions in both CND and lumen radii and an increase in cells' volume must imply that there is an increase in the length of the CND to account for the extra volume generated, provided that there is no volume leak in the CND (i.e. that all the extra cell volume caused by the Blebbistatin treatment stays in the CND). The latter was suggested by the Bouchard Lab. On the other hand, we would expect efferocytosis and cellular extrusion to cause a decrease in the length of the CND. Therefore, in Blebbi-treated CNDs, elongation and shortening of the CND are happening simultaneously but our fluid dynamics framework (see Section 2.2.5) only takes into account shortening of the CND. To account for elongation, one can either formulate a PDE model (described in Section 3.2.5) or use the experimentally measured CND length by the Bouchard Lab (McGill University) at discrete time points to approximately quantify the contribution of both shortening and elongation. The former would require solving the PDE model numerically by doing parameter fitting in MATLAB; this would have required the use of complex numerical fitting techniques that would have produced results that are similar to those produced by using the latter method.

Given that we have opted to choose the discrete time model, we have used the measured

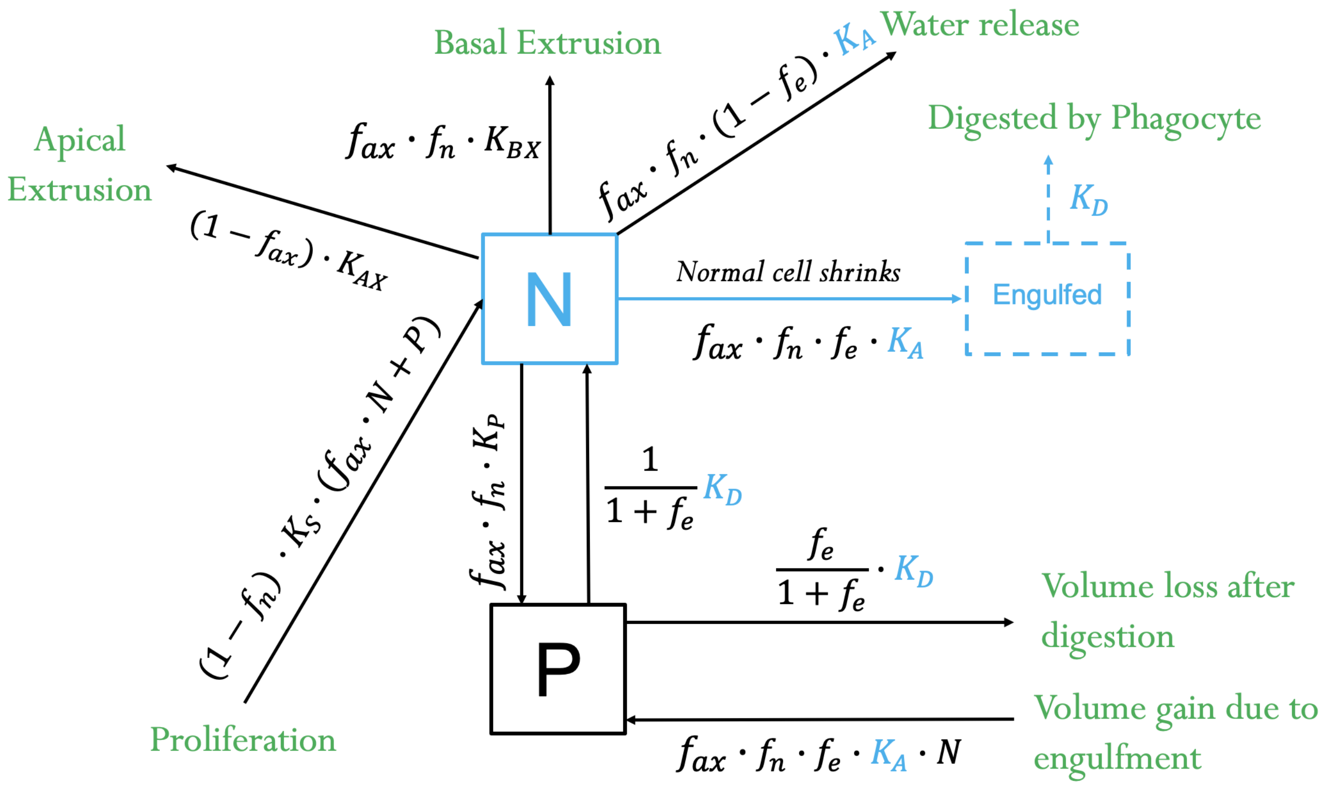

Figure 3.5: The multistate model, "MS2", describing the interactions between the different types of cells in terms of volume fraction in a Blebbi-treated CND. The efferocytosis pathway is colored in blue."N" stands for "Normal" and "P" stands for "Phagocytes". The MS2 model accounts for both apical and basal extrusion whereas only basal extrusion is present in the MS1 model.

length of the Blebbi-treated CND at 6 time points: 0 h, 3 h, 6 h, 12 h, 24 h and 48 h (see Section 3.1). Using the Control (untreated) model, we quantified the elongation caused by Blebbistatin between each time point (see Figure 3.7). This is done by comparing the predicted length of the CND using the Control model (labeled in blue in Figure 3.7) and the measured length of the Blebbistatin treated CND (labeled in green in Figure 3.7) at each time point. The difference between those two lengths is assumed to be an elongation caused by Blebbistatin (labeled in red Figure 3.7). Each of these elongations are then converted into an instantaneous elongation at each previous time point (in purple in Figure 3.8). The calculations of each of these instantaneous elongations (detailed in the next section) are based on the percentages colored in red on Figure 3.7 and take into account

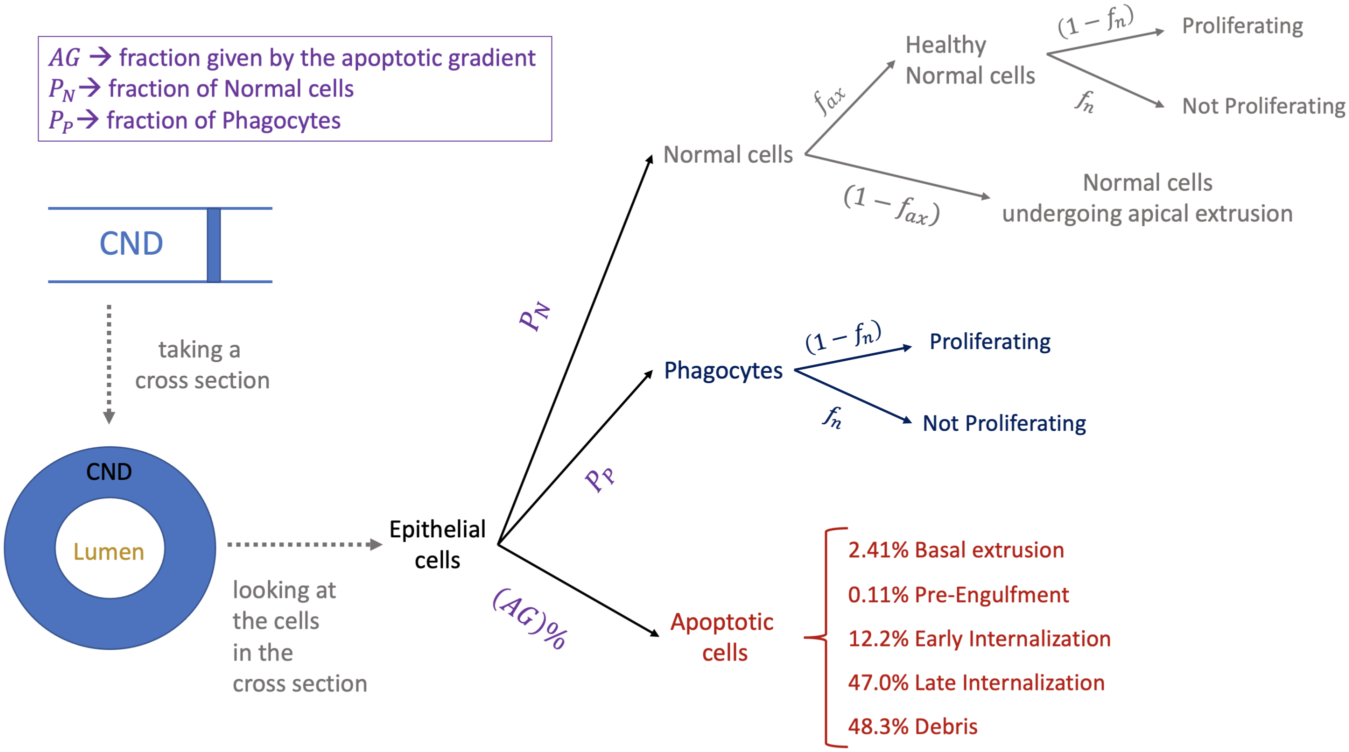

Figure 3.6: When taking a cross-section of the Blebbistatin treated CND at a specific spatiotemporal time point, the percentage of cells undergoing apoptosis either through basal extrusion or efferocytosis is given by the apoptotic gradient at that specific location and time point. The remaining cells are either Normal cells or Phagocytes. Within the pool of Normal cells, a fraction $(1 - f_{ax})$ of them undergo apical extrusion and the rest are healthy Normal cells. Within the pool of healthy Normal cells or Phagocytes, a fraction $(1 - f_n)$ of them are proliferating. The fraction of Normal cells and Phagocytes with respect to the total amount of cells in the cross-section, P_N and P_P, respectively, are calculated from the experimental data, using the method described in Section 2.2.8.

the reduction in both CND and lumen radii and the increase in cell volume. This method allows us to incorporate the effects of Blebbistatin treatment in a stepwise manner based on experimental data.

Time t (in hours)	Experimental Data
0h	278
3h	281
6h	283
12h	315
24h	323
36h	333
48h	350

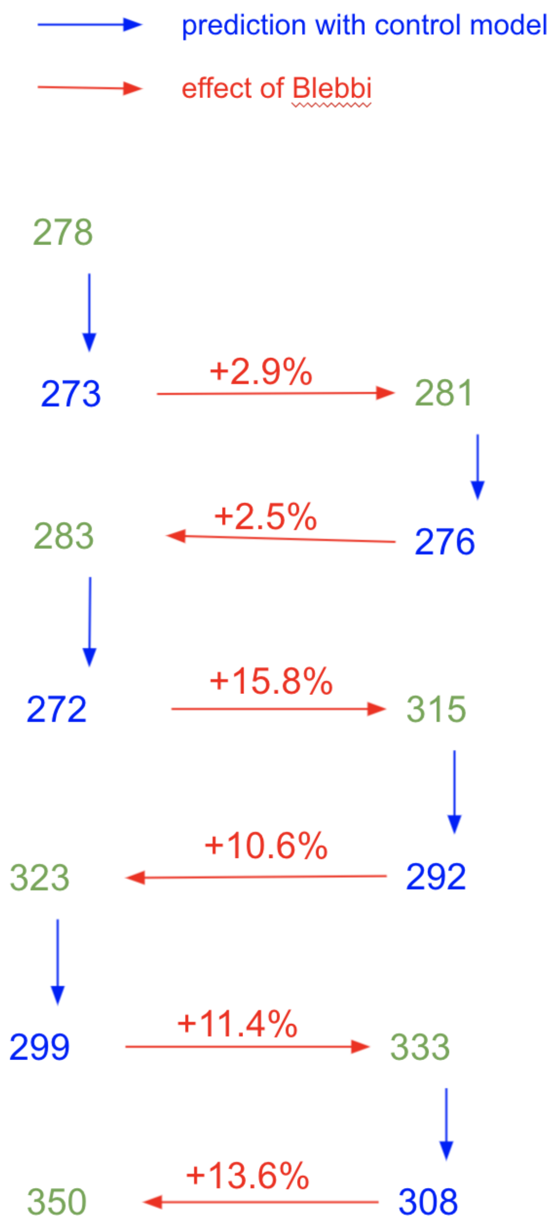

Figure 3.7: The length of the Blebbistatin treated CND has been measured at 6 time points: 0 h, 3 h, 6 h, 12 h, 24 h and 48 h (green). Between each time point, using the Control model, we predicted the length of the CND (blue). By comparing the predicted length (blue) with the experimental data (green) at each time point (except for the first one), we can quantify the percentage of elongation caused by Blebbistatin (red). The length unit is μm.

To model Blebbi-treated CND shortening we perform some parameter fitting by solving the IBM analytically within each time interval (see Figure 3.8), as follows:

1. We initially apply an instantaneous elongation at $t = 0\ h$ on the experimental data (purple arrow at $t = 0\ h$ in Figure 3.8), we then run the IBM from $t = 0\ h$ to $t = 3\ h$, which includes shortening only, (diagonal yellow arrow between $t = 0\ h$ and $t = 3\ h$ in Figure 3.8). This is then followed by applying an instantaneous elongation on the predicted length at $t = 3\ h$ (purple arrow at $t = 3\ h$ in Figure 3.8) .
2. Using the instantaneous elongated length at $t = 3\ h$, we run the IBM from $t = 3\ h$ to $t = 6\ h$, which includes shortening only, (diagonal yellow arrow between $t = 3\ h$ and $t = 6\ h$ in Figure 3.8). This is then followed by applying an instantaneous elongation on the predicted length at $t = 6\ h$ (purple arrow at $t = 6\ h$ in Figure 3.8).
3. Using the instantaneous elongated length at $t = 6\ h$, we run the IBM from $t = 6\ h$ to $t = 12\ h$ (diagonal yellow arrow between $t = 6\ h$ and $t = 12\ h$ in Figure 3.8). This is then followed by applying an instantaneous elongation on the predicted length at $t = 12\ h$ (purple arrow at $t = 12\ h$ in Figure 3.8).
4. Using the instantaneous elongated length at $t = 12\ h$, we run the IBM from $t = 12\ h$ to $t = 24\ h$ (diagonal yellow arrow between $t = 12\ h$ and $t = 24\ h$ in Figure 3.8). This is then followed by applying an instantaneous elongation on the predicted length at $t = 24\ h$ (purple arrow at $t = 24\ h$ in Figure 3.8).
5. Using the instantaneous elongated length at $t = 24\ h$, we run the IBM from $t = 24\ h$ to $t = 48\ h$ (diagonal yellow arrow between $t = 24\ h$ and $t = 48\ h$ in Figure 3.8).

Incorporation of these discrete steps with the IBM produces what we call the "Blebbi model". The details of the mathematical model are given in the next section. It is important to point out here that we are only working with six time points but the general method (described in the next section) is designed for any number of n steps. As n gets bigger, this method approaches a continuous PDE model discussed earlier.

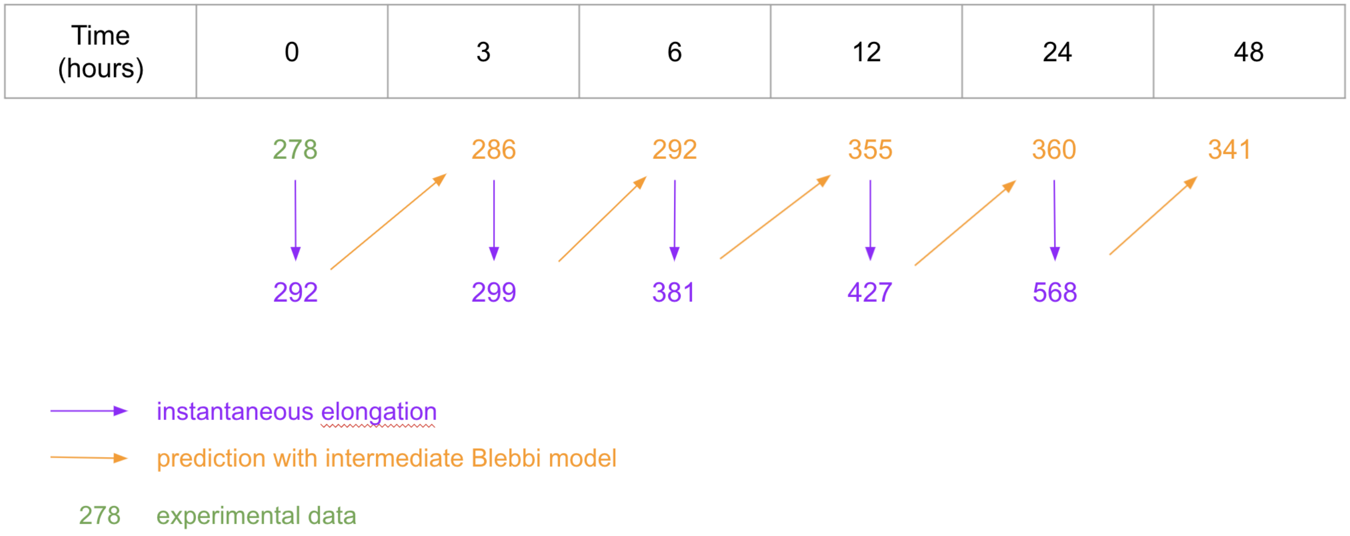

Figure 3.8: The Blebbi model consists of applying instantaneous elongations and using the intermediate Blebbi model (IBM). The length unit is μm.

3.2.3 Algorithm of Blebbi model

In this section, we generalize the Steps 1 to 5 of Section 3.2.2 to any number of n time points.

We know that Blebbistatin treatment acts in the following ways:

1. It reduces the CND radius from 37.35 μm to 27.2 μm.
2. It reduces the lumen radius from 13.7 μm to 12.4 μm.
3. It increases cell volume by 32 %.
4. It increases apical extrusion from 0% to 4.2% of CND cells..

According to the protocol used in Bouchard Lab, Blebbistatin treatment starts at $t = 0\ h$ and the final effects (mentioned above) are measured at $t = 48\ h$. Since we know that the time it takes for a cell to be extruded out of the CND is the same as the time it takes for a cell to reach the middle of the Late Internalization stage, we can infer that

$$\frac{1}{K_{AX}} = \frac{1}{K_{EI}} + \frac{1}{2K_{LI}},$$

where K_{EI} and K_{LI} values are taken from the Control model (see Table 7 in the Appendix) since, as discussed previously, these rates are assumed to be the same in Control and Blebbi-treated CNDs.

Suppose that at n time points $t_1 < t_2 < t_3 ... < t_{n-1} < t_n$, the experimentally measured length of the CND are denoted by $d_1, d_2, ..., d_n$, respectively, and that $t_1 = 0\ h$ and $t_n = 48\ h$ (see Figure 3.9).

For each $i = 1, ..., n-1$, let's run the Control model from $t = 0$ to $t = t_{i+1} - t_i$ and let c_i denote the predicted length at $t = t_{i+1}$. Then, by defining

$$p_i = \frac{d_{i+1} - c_i}{c_i} 100 \qquad \forall i = 1, ..., n-1, \tag{3.2}$$

we can conclude that the Blebbistatin treatment causes an elongation of $p_i\%$ between t_i and t_{i+1} for all $i = 1, ..., n-1$. Let us now introduce the generalized Blebbi model. At each time point t_i with $i = 1, ..., n-1$, we apply an instantaneous elongation to the CND length and then run the IBM from t_i to t_{i+1}. For every t_i (except t_n), we need to characterize the instantaneous elongation. We will do so rigorously in a general framework and then apply it to our data.

Instantaneous Elongation

Let's suppose that the CND has length L, and that instantaneously the radius of the CND and of the lumen reduces from R_1 to R_2 and from r_1 to r_2 respectively and that the volume of each cell increases by $a\%$. We then calculate the length of the Blebbi-treated CND needed to fit this new total volume in the CND, we will call this new length the elongated length, denoted by L_e. Let V_1 and V_2 denote the volume of the CND before and after the instantaneous changes. It follows that

$$\frac{100 + a}{100} V_1 = V_2 \tag{3.3}$$

Time t (in hours)	Experimental Data
t_1	d_1
t_2	d_2
t_3	d_3
...	...
t_{n-1}	d_{n-1}
t_n	d_n

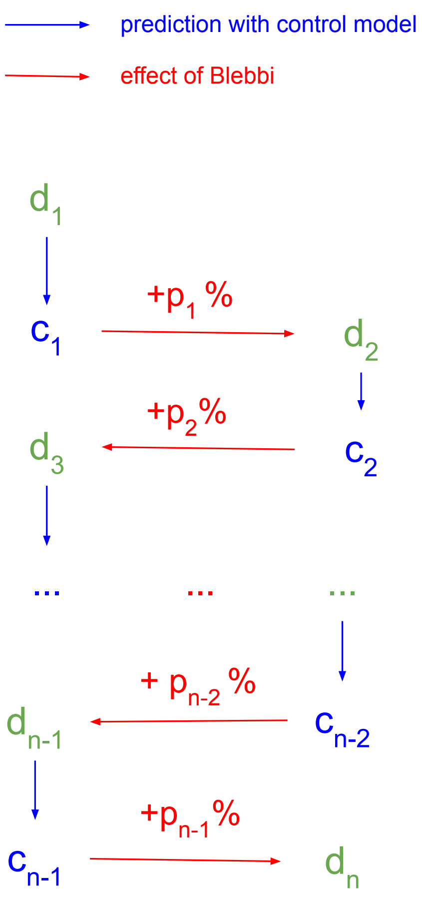

Figure 3.9: The length of the Blebbistatin treated CND has been measured at n time points: t_1, t_2, ..., t_n (green). Between two time points, the Control model, is used to predict the length of the CND (blue). By comparing the predicted length (blue) with the experimental data (green) at each time point (except for the first one), we can quantify the percentage of elongation caused by Blebbistatin (red). The length unit is μm.

Using the volume formula for a cylinder, we obtain

$$\frac{100 + a}{100} L_\pi (R_1^2 - r_1^2) = L_e \pi (R_2^2 - r_2^2), \tag{3.4}$$

and solving for L_e, we obtain

$$L_e = \frac{L(R_1^2 - r_1^2)}{(R_2^2 - r_2^2)} \frac{100 + a}{100}. \tag{3.5}$$

Generalized Blebbi model

Let R_C and R_B be the radii of the CND in Control CND and at $t = 48$ h in Blebbi-treated CND respectively. Similarly, let r_C and r_B be the radii of the lumen in Control CND and at $t = 48$ h in Blebbi-treated CND, respectively. Let γ denote the factor by which the volume of each cell at $t = 0$ h is multiplied to reach its final volume at $t = 48$ h in Blebbi-treated CND; experimentally, we know that $\gamma = 1.32$. Let X_C and X_B be the extrusion percentages, with respect to the total number of cells, in control and at $t = 48$ h in Blebbi-treated CND, respectively.

Let us define the following parameters

$$\alpha = \frac{R_B}{R_C}, \tag{3.6}$$

$$\beta = \frac{r_B}{r_C}, \tag{3.7}$$

$$\delta = X_B - X_C, \tag{3.8}$$

$$p = \sum_{i=1}^{n-1} p_i. \tag{3.9}$$

Based on this, we have for each $i = 1, ..., n - 1$,

$$\alpha_i = \alpha^{\frac{p_i}{p}}, \tag{3.10}$$

$$\beta_i = \beta^{\frac{p_i}{p}}, \tag{3.11}$$

$$\gamma_i = \gamma^{\frac{p_i}{p}}, \tag{3.12}$$

$$\delta_i = X_C + \delta \frac{\sum_{k=1}^{i} p_k}{p}. \tag{3.13}$$

Notice that

$$\prod_{i=1}^{n-1} \alpha_i = \alpha, \tag{3.14}$$

$$\prod_{i=1}^{n-1} \beta_i = \beta, \tag{3.15}$$

$$\prod_{i=1}^{n-1} \gamma_i = \gamma, \tag{3.16}$$

$$\delta_{n-1} = X_B. \tag{3.17}$$

By applying an instantaneous elongation at t_1 on the CND with $L = d_1$, $R_1 = R_c$, $r_1 = r_c$, $R_2 = \alpha_1 R_c$, $r_2 = \beta_1 r_c$, and $a = (\gamma_1 - 1)100$, we obtain an elongated length L_{e_1} given by

$$L_{e_1} = d_1 \frac{(R_c^2 - r_c^2)}{((\alpha_1 R_c)^2 - (\beta_1 r_c)^2)} \gamma_1. \tag{3.18}$$

Then using the elongated length L_{e_1} as our initial length at $t = 0$, we run the IBM until $t = t_2 - t_1$ in Blebbi conditions with a fraction of apical extrusion f_{ax} equal to $\delta_1\%$. Let $B(L_{e_1})$ denote the length at $t = t_2$ predicted by the IBM in order for the digestion time to be the same as in the Control model. The rate of digestion of Control is given by $K_{D_{Control}} = 2.40$. Let K_{D_1} denote the digestion rate of the IBM run between $t = 0$ and $t = t_1$. $K_{D_1}^{-1}$ gives the digestion time associated to a Phagocyte of one volume fraction but since the volume of each cell has been multiplied by γ_1 due to the Blebbistatin treatment, the digestion time of one entire Phagocyte is given by $\gamma_1 K_{D_1}^{-1}$. Therefore, in order for the digestion time to be the same in both model, we need

$$\frac{1}{K_{D_{Control}}} = \frac{\gamma_1}{K_{D_1}}, \tag{3.19}$$

which is equivalent to

$$K_{D_1} = \gamma_1 K_{D_{Control}}, \tag{3.20}$$

see Tables 7 and 8 of the Appendix.

Then, we apply an instantaneous elongation at t_2 on the CND with $L = B(L_{e_1})$, $R_1 = \alpha_1 R_c$, $r_1 = \beta_1 r_c$, $R_2 = \alpha_1 \alpha_2 R_c$, $r_2 = \beta_1 \beta_2 r_c$, and $a = (\gamma_2 - 1)100$, which leads to the elongated length L_{e_2} given by

$$L_{e_2} = B(L_{e1}) \frac{((\alpha_1 R_c)^2 - (\beta_1 r_c)^2)}{((\alpha_1 \alpha_2 R_c)^2 - (\beta_1 \beta_2 r_c)^2)} \gamma_2. \tag{3.21}$$

Then using the elongated length L_{e_2} as our initial length at $t = 0$, we run the IBM until $t = t_3 - t_2$ in Blebbi conditions with a fraction of apical extrusion f_{ax} equal to $\delta_2\%$. Let $B(L_{e_2})$ denote the length at $t = t_3$ predicted by the model in order for the digestion time to be the same as in Control. Following the same logic as earlier, in order for the digestion time to be the same in the Control model and in the IBM ran between $t = t_2$ and $t = t_3$, we need

$$K_{D_2} = \gamma_2 K_{D_{Control}}, \tag{3.22}$$

where K_{D_2} is the digestion rate associated to the IBM run between $t = t_2$ and $t = t_3$.

We repeat this process until we reach $B(L_{e_{n-1}})$. The heatmaps of the spatiotemporal quantities K_A, v and K_{BX} of the IBMs used in each step are plotted in Figure 4.8, 4.9, 4.10, 4.11 and 4.12 of the Appendix.

If we define

$$R_0 = R_c, \tag{3.23}$$

$$R_i = \alpha_i R_{i-1}, \qquad \forall i = 1, ..., n-1 \tag{3.24}$$

$$r_0 = r_c, \tag{3.25}$$

$$r_i = \beta_i r_{i-1}, \qquad \forall i = 1, ..., n-1, \tag{3.26}$$

it follows that the elongated length L_{e_i} at each time point t_i, for $i = 1, ..., n-1$ is given by

$$L_{e_1} = d_1 \frac{(R_c^2 - r_c^2)}{(R_1^2 - r_1^2)} \gamma_1 \tag{3.27}$$

and

$$L_{e_i} = B(L_{e_{i-1}}) \frac{(R_{i-1}^2 - r_{i-1}^2)}{(R_i^2 - r_i^2)} \gamma_i. \qquad \forall i = 2, ..., n-1, \tag{3.28}$$

where each length $B(L_{e_i})$, $i = 1, ..., n-1$, is obtained by using the elongated length L_{e_i} at $t = 0$ and running the IBM until $t = t_i - t_{i-1}$ in Blebbi conditions (while incorporating the same apoptotic gradient and stationary distribution as in control, an extrusion rate of $\delta_i\%$, with the same digestion time as in Control, see Tables 7, 8, 9, 10, 11 and 12 of the Appendix).

For $i = 2, ..., n$, the generalized Blebbi model can quantify a theoretical CND length of $B(L_{e_i})$ at t_i, plotted in orange on Figure 3.4 and 3.10.

3.2.4 Quantifying the total density ρ_T of the CND during Blebbistatin treatment

Unpublished data from Bouchard Lab (McGill University) for volume fraction (2000) and length of the CND (300 μm) in healthy ducts indicate that $\rho_T = 2000/300\ \mu m^{-1}$ in a healthy duct. The CND and lumen radii of a healthy CND are equal to $R = 37.35\mu m^{-1}$ and $r = 27.2\mu m^{-1}$, respectively. This means that a volume of $V = \pi(R^2 - r^2)L$ (volume of the CND) corresponds to a volume fraction of 2000. Now let's suppose that we have a duct with the same number of cells, but with the volume of each cell multiplied by a factor of Γ, a CND and a lumen radii equal to $\tilde{R}$ and $\tilde{r}$, respectively. As explained in Section 3.2.3, in order for the volume to be kept in the CND, this new duct must have a length of

$$L_n = \frac{L(R^2 - r^2)}{(\tilde{R}^2 - \tilde{r}^2)} \Gamma;$$

and the volume of the new duct is equal to

$$V_n = \pi(\tilde{R}^2 - \tilde{r}^2)L_n,$$

so the volume fraction occupied by the new duct is given by $\frac{V_n}{V} \times 2000$. This means that the density of the new duct is given by

$$\begin{aligned}
\rho_{T_n} &= \frac{V_n}{V}\frac{2000}{L_n} \\
&= \frac{(\tilde{R}^2 - \tilde{r}^2)L_n}{(R^2 - r^2)L}\frac{2000}{L_n} \\
&= \frac{(\tilde{R}^2 - \tilde{r}^2)2000}{(R^2 - r^2)L}\ \mu m^{-1}.
\end{aligned}$$

Using the above method and the notation from Section 3.2.3 (in which $\rho_{T_i},\ R_0,\ R_i,\ r_0$ and r_i are defined), we can conclude that the total density used in the IBM between t_{i-1} and t_i (for $i = 1, ..., n-1$) is equal to

$$\rho_{T_i} = \frac{(R_i^2 - r_i^2)2000}{(R_0^2 - r_0^2)300}\ \mu m^{-1}.$$

3.2.5 PDE model for Blebbistatin treated CND

If we were to formulate a PDE model to account the Blebbistatin effects, the equations 2.8, 2.10 and 2.11 would not be valid anymore. Since the radius of the CND is decreasing and the cell volume is increasing, the direction of the cellular drifting is not necessarily always heading toward the bladder as suggested by Figure 2.12. Let's investigate the best way to formulate a PDE model that takes into account shortening due to efferocytosis and extrusion, as well as elongation due to Blebbistatin (which also includes decrease in both CND and lumen radii and the increase in cell volume by 32%).

Differential equation for Elongation only

Let $V(t)$ denote the volume fraction of the CND at time t and V_0 denote the volume fraction of the CND at $t = 0$ when Blebbistatin treatment starts. Unpublished data from

Bouchard Lab (McGill University) suggest that Blebbistatin increases cell volume by 32%. By approximating the effect of the treatment as an exponential growth, (an assumption consistent with other modeling studies of tissue growth, e,g, cancer, [60]), we obtain

$$V(t) = V_0(1.32 - 0.32e^{-\frac{t}{\tau}}), \tag{3.29}$$

where τ is a time constant, that can be described by the following initial value problem,

$$\frac{\partial V(t)}{\partial t} = V_0 \frac{0.32}{\tau} e^{-\frac{t}{\tau}} \tag{3.30}$$

$$V(0) = V_0. \tag{3.31}$$

Differential equation for Shortening only

Using the same notation as above, and recalling the rate of CND volume fraction loss at time t, denoted by $R_V(t)$ (introduced in Section 2.2.7), we have

$$R_V(t) = \int_{-L(t)}^{0} f_{ax} f_n((1-f_e)K_A + K_{BX})\rho_N - (1-f_n)(f_{ax}\rho_N + \rho_P)K_S + \frac{f_e}{1+f_e} K_D \rho_P$$
$$+ (1-f_{ax})K_{AX}\rho_N \, dx.$$

The initial value problem for volume fraction of the CND is thus given by

$$\frac{\partial V(t)}{\partial t} = -R_V(t) \tag{3.32}$$

$$V(0) = V_0. \tag{3.33}$$

Merging shortening and elongation

Since the volume of the CND is not only subject to gain but also to loss, V_0 needs to be replaced by V in equation 3.30 , producing the following initial value problem

$$\frac{\partial V(t)}{\partial t} = V(t) \frac{0.32}{\tau} e^{-\frac{t}{\tau}} - R_V(t) \tag{3.34}$$

$$V(0) = V_0. \tag{3.35}$$

The difference between this model and the previous one is that ρ_T is not constant and the expression for $L(t)$ is not an exponential decay anymore but a more complicated function. Their exact expression are described below.

Let $R(t)$ and $r(t)$ denote the radii of the CND and the lumen, respectively. Let $R_C = 37.35\mu m$ and $r_C = 13.7\mu m$ be the radii of the Control CND and the Control lumen, respectively. Let $R_B = 27.2\mu m$ and $r_B = 12.4\mu m$ be the radii of the CND and the lumen after 48 hours of Blebbi treatment. $R(t)$ and $r(t)$ are given by

$$R(t) = R_C - (R_C - R_B)(1 - e^{-t/\tau}) \tag{3.36}$$

and

$$r(t) = r_C - (r_C - r_B)(1 - e^{-t/\tau}). \tag{3.37}$$

A WT1 CND occupies a volume fraction of $V_{WT1} = 2000$ at $t = 0$ and its real volume at $t = 0$ is given by

$$W_{WT1} = 300\pi(R_C^2 - r_C^2). \tag{3.38}$$

Let $W(t)$ denote the volume of the CND at time t. It is clear that

$$W(t) = L(t)\pi(R(t)^2 - r(t)^2)$$

and that

$$\frac{W(t)}{V(t)} = \frac{W_{WT1}}{V_{WT1}}.$$

Using the above formulas, the length of the CND $L(t)$, is given by

$$L(t) = \frac{W_{WT1}}{V_{WT1}} \frac{V(t)}{\pi(R(t)^2 - r(t)^2)}. \tag{3.39}$$

According to Section 3.2.4,

$$\rho_T = \frac{(R(t)^2 - r(t)^2)2000}{(R_C^2 - r_C^2)L(t)} \mu m^{-1}. \tag{3.40}$$

Substituting equations 3.39 and 3.40 into equation 3.34 leads to a PDE model that is not solvable analytically on Mathematica and hence needs to be solved numerically by doing some parameter fitting in MATLAB.

3.2.6 Contribution of different components to CND elimination

As explained in Section 3.2.3, we have used the IBM to compute the length of the Blebbi-treated CND between two time points. What differentiates each step when applying the IBM is the fraction of cells undergoing apical extrusion $(1 - f_{ax})$ and the total density ρ_T (see Section 3.2.4). Using this information, we can use the the model and these steps to compute the volume fraction eliminated by efferocytosis (V_E), apical extrusion (V_{AX}) and basal extrusion (V_{BX}) and the total volume fraction eliminated (V_{Tot}) individually or in combination. This can be done by taking advantage of the percentage of cell clearance done through efferocytosis, apical extrusion and basal extrusion are given by $\frac{V_E}{V_{Tot}}100$, $\frac{V_{AX}}{V_{Tot}}100$ and $\frac{V_{BX}}{V_{Tot}}100$, respectively. Using this approach, we obtain the values listed in Table 3.

3.2.7 Effects of selective removal of different components on CND length

As stated earlier, the IBM accounts for four crucial components: Proliferation (P), Efferocytosis (E) Apical Extrusion (AE) and Basal Extrusion (BE). The volume fraction added by proliferation between $t = 0$ and $t = T$ is given by

$$V_P(r) = \int_0^T \int_{-L(t)}^0 (1 - f_n) f_s K_S (f_{ax}\rho_N + \rho_P) \, dx dt. \tag{3.41}$$

Now, we will explain how to predict the length of the CND when the contribution of apical extrusion is removed (blue curve of Figure 3.10). We will use the same notation as Section 3.2.3. The first point of the blue curve is $(0, d_1)$.

By applying an instantaneous elongation at t_1 on the CND with $L = d_1$, $R_1 = R_c$, $r_1 = r_c$, $R_2 = \alpha_1 R_c$, $r_2 = \beta_1 r_c$, and $a = (\gamma_1 - 1)100$, we obtain the elongated length L_{e_1} given by

$$L_{e_1} = d_1 \frac{(R_c^2 - r_c^2)}{((\alpha_1 R_c)^2 - (\beta_1 r_c)^2)} \gamma_1. \tag{3.42}$$

Then using the elongated length L_{e_1} as our initial length at $t = 0$, we can run the IBM until $t = t_2 - t_1$ in Blebbi conditions with a fraction of apical extrusion f_{ax} equal to $\delta_1\%$. Let $B(L_{e_1})$ denote the length at $t = t_2$ predicted by the IBM when the digestion time is the same as in Control. Using the same method as Section 2.3.4, we can compute the volume fraction eliminated by efferocytosis (V_E^1), apical extrusion (V_{AX}^1), basal extrusion (V_{BX}^1) and the volume added by proliferation (V_P^1). Now, similar to the logic explained in Section 2.3.4, let us define

$$L_{P+E+BX}^1(t) = B(L_{e_1}) - \frac{V_P^1(t) - V_E^1(t) - V_{BE}^1(t)}{\rho_T}. \tag{3.43}$$

The quantity $L_{P+E+BX}^1(t_2 - t_1)$ gives the length of the CND at $t = t_2$ when removing the contribution of apical extrusion. We add the point $(t_2, L_{P+E+BX}^1(t_2 - t_1))$ to the blue plot. Then, we apply an instantaneous elongation at t_2 on the CND with $L = L_{P+E+BX}^1(t_2 - t_1)$, $R_1 = \alpha_1 R_c$, $r_1 = \beta_1 r_c$, $R_2 = \alpha_1 \alpha_2 R_c$, $r_2 = \beta_1 \beta_2 r_c$, and $a = (\gamma_2 - 1)100$, which leads to the elongated length L_{e_2} given by

$$L_{e_2} = L_{P+E+BX}^1(t_2 - t_1) \frac{((\alpha_1 R_c)^2 - (\beta_1 r_c)^2)}{((\alpha_1 \alpha_2 R_c)^2 - (\beta_1 \beta_2 r_c)^2)} \gamma_2. \tag{3.44}$$

Then using the elongated length L_{e_2} as our initial length at $t = 0$, we run the IBM until $t = t_3 - t_2$ in Blebbi conditions with a fraction of apical extrusion f_{ax} equal to $\delta_2\%$. As before, we let $B(L_{e_2})$ denote the length at $t = t_3 - t_2$ predicted by the IBM when the digestion time is the same as in Control. Using the same method as in Section 2.3.4, we compute the volume fraction eliminated by efferocytosis (V_E^2), apical extrusion (V_{AX}^2), basal extrusion (V_{BX}^2) and the volume added by proliferation (V_P^2). Now let us define

$$L_{P+E+BX}^2(t) = B(L_{e_2}^2) - \frac{V_P^2(t) - V_E^2(t) - V_{BX}^2(t)}{\rho_T} \tag{3.45}$$

which gives the length of the CND at $t = t_3$ when removing the contribution of apical extrusion. We add the point $(t_3, L_{P+E+BX}^2(t_3 - t_2))$ to the blue plot. We continue this process for every time point along the blue curve.

The purple and grey curves of Figure 3.10 are obtained by following the same procedure, but by using $L_{P+AX+BX}$ and L_{P+BX}, respectively. The green plot is the experimental data given in Figure 3.7. The orange plot of Figure 3.4 and 3.10 corresponds to the Blebbi model described in Section 3.2.3 (i.e. with all the component included).

3.3 Results

The Control model (Section 3.2.1) and the Blebbi model (Sections 3.2.2 and 3.2.3) quantify CND lengths that are very close to the experimental data (see Figure 3.4). This indicates that they capture well the key parameters of CND elimination ex vivo with and without Blebbistatin treatment. One can argue that this is a circular argument because we designed the Blebbi model using experimental data that already incorporates elongation effects (see Section 3.2.2 and 3.2.3). Still, this is useful to us for two reasons: it shows that the core of the model describing the dynamics of the duct shortening adapts well to ex vivo conditions, and now that we have a Blebbi model that is physiologically close to the experimental observation, we can use it to produce insightful conclusions that are hard to deduce experimentally; that includes dissecting the contribution of each component: proliferation, efferocytosis, apical extrusion etc (like we did for WT1).

We have already seen in Section 2.3 that Basal Extrusion contributes little to the CND shortening. Now, let us use the Blebbi model to quantify the role of Efferocytosis (E), Apical Extrusion (AX) and Basal Extrusion (BX) in the shrinkage of Blebbi-treated CND.

Using the method developed in Section 3.2.6, we generate Table 3 demonstrating that Efferocytosis is always the main driver of cell clearance throughout time. To validate this further, we have plotted the evolution of the length of the CND in different conditions in Figure 3.10 using the method developed in Section 3.2.7. As expected, the overall effects of Blebbistatin (B), basal extrusion (BE) and cell proliferation (Prol) cause a CND elongation (purple plot). However, when apical extrusion (grey curve) or efferocytosis (blue curve) are added, the elongation is no longer apparent at all time points. We can see that efferocytosis is more efficient than apical extrusion at reducing the elongation of the CND (blue plot is under the grey plot). This once again shows that efferocytosis is a crucial driver of the CND clearance over time.

As mentioned in the Introduction, the reason why the Blebbistatin experiment was conducted is because actomyosin is most of the time crucial to morphogenesis. First of all, let us determine if there is shrinkage happening in Blebbi-treated CND. By looking at the experimental data (green plot of Figure 3.4), the length of the CND has increased between t=0 h and t=48 h. This is because Blebbistatin causes an elongation of the CND. To isolate the effect of this elongation, we have removed the contribution of Apical Extrusion and Efferocytosis and plotted the evolution of the CND length in Figure 3.10 (purple plot). This plot predicts a much longer CND length than when all the components are activated (orange plot of Figure 3.10). This shows that even though the overall evolution of the CND is an elongation, there is still active cell elimination done through efferocytosis and apical extrusion; this is demonstrated in the $\sim$600 μm difference in CND length between the purple and orange curves at $t = 24$ h in Figure 3.10. As explained earlier, apical extrusion appears in Blebbi-treated CNDs and is almost non existent in non treated CNDs (Figure 3.1). Efferocytosis, on the other hand, is present in both conditions. To isolate the contribution of the CND shrinkage, independent of actomyosin and Blebbistatin, we investigate the contribution of efferocytosis alone by looking at the grey curve of Figure 3.10. From this curve, we can see that efferocytosis is responsible for a CND shrinkage of around 350 μm (the difference between the grey and orange plots at $t = 48$ h). Therefore, our model suggests that shrinkage is still efficient throughout time in the absence of actomyosin primarily through non-professional efferocytosis and secondly through apical extrusion and that the efficiency of efferocytosis is independent of actomyosin.

Table 3: The percentages of cell clearance of each component.

Time period	Efferocytosis	Apical Extrusion	Basal Extrusion
from $t = 0\ h$ to $t = 3\ h$	89.5	4.3	6.2
from $t = 3\ h$ to $t = 6\ h$	86.2	7.9	5.9
from $t = 6\ h$ to $t = 12\ h$	71.1	24.0	4.9
from $t = 12\ h$ to $t = 24\ h$	64.2	31.4	4.4
from $t = 24\ h$ to $t = 48\ h$	53.2	43.2	3.6

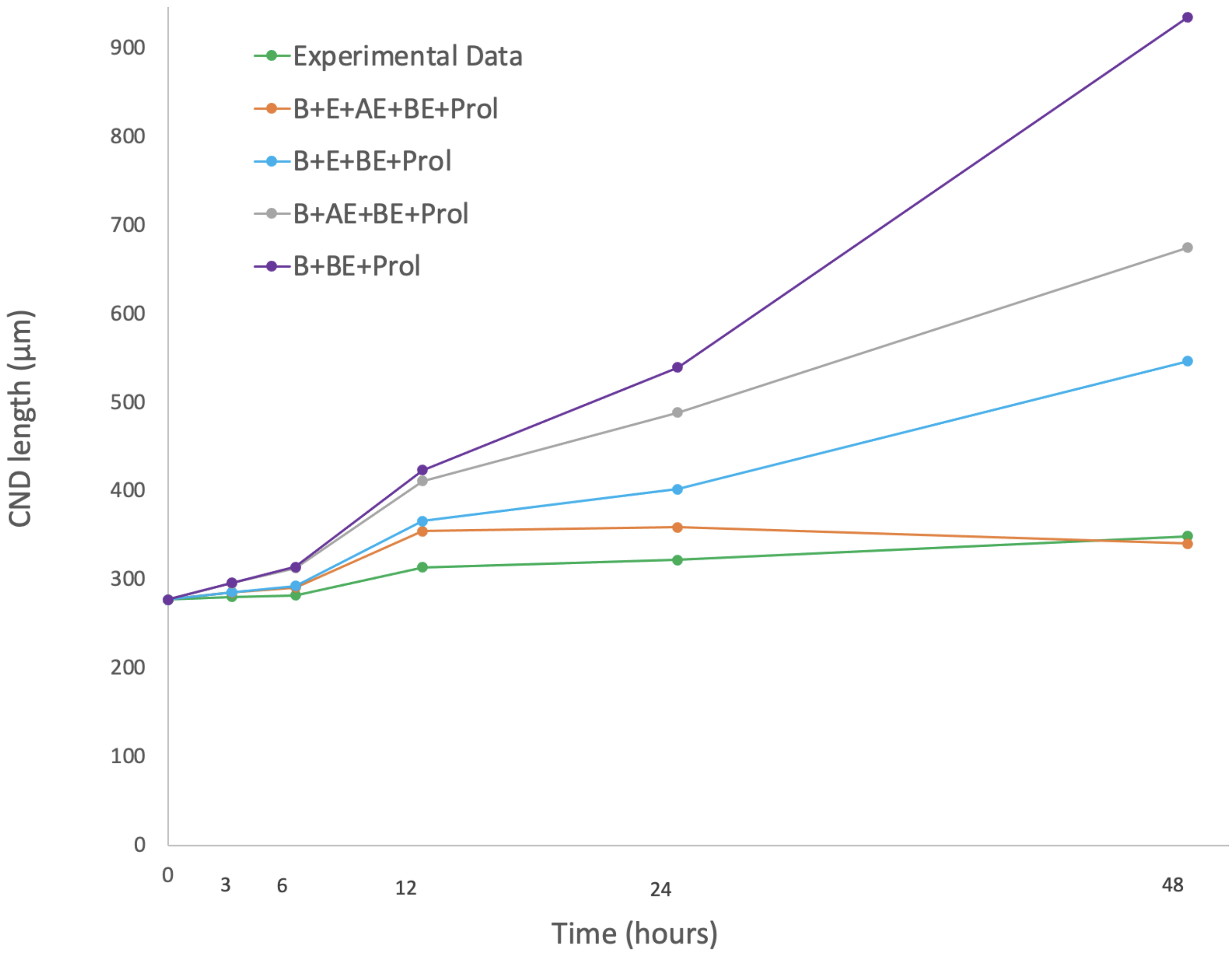

Figure 3.10: The time evolution of the length of the CND in different conditions as determined by Blebbi model. These conditions include: the contribution of Blebbi effect, basal extrusion and cell proliferation (purple curve), the contributions of Blebbi effects, basal extrusion, cell proliferation and apical extrusion (gray curve), the contributions of Blebbi effects, basal extrusion, cell proliferation and efferocytosis (blue curve) and the contributions of all components, including Blebbi effects, basal extrusion, cell proliferation, apical extrusion and efferocytosis (orange curve). Experimental data of Blebbi-treated CND is in green.

Chapter 4

Conclusion and discussions

4.1 In vivo models

The initial purpose of this study was to estimate the dwell time spent in each stage of the non-professional efferocytosis happening in the CND. This task proved to be non-trivial, as we quickly realised that we needed to employ spatiotemporal modeling techniques to describe the dynamics of the CND; that involved integrating the non-professional efferocytosis, shortening of the CND and the apoptotic gradient into one spatiotemporal model. In order to study all of these processes simultaneously, we combined two submodels: a multistate model that describes the cellular interactions happening in the CND (including efferocytosis and extrusion) and another that describes the shortening of the CND as a flux of cells drifing toward the bladder. The two submodels are coupled together through a set of advection equations describing cellular drifting that incorporate source and sink terms representing cellular interactions (e.g., efferocytosis described as sink and proliferation described as source). This way, we managed to model the spatiotemporal dynamics of the CND at both the cellular and tissue levels.

Using an in vivo wild type CND data set provided by the Bouchard Lab (McGill University), referred to as WT1, we constrained the set of parameters of the model and derived boundary conditions to the dynamics of the system, allowing us to solve the model analytically using Mathematica. We generated analytical expressions for all the spatiotemporal variables (including the rate of efferocytosis K_A and the cellular drifting velocity v) and provided the dwell time in each stage of the non-professional efferocytosis. Our results fell in the range of physiologically realistic estimates. How these estimates get altered in pathological conditions, such as during vesicoureteral reflux and junction obstruction, remains to be seen. Our model also enabled us to quantify the contribution of each component (proliferation, basal extrusion and non-professional efferocytosis) to the CND shrinkage over time (as opposed to two discrete times as was done experimentally). This showed that CND shrinkage is mainly driven by efferocytosis and that basal extrusion plays a minor role in this process. These tasks performed by our model could not be done experimentally and provided information that our collaborators from the Bouchard Lab were interested in.

4.2 Ex vivo models

Actomyosin plays crucial role in several developmental processes. To study its impact on the elimination of the CND, ex vivo experiments in the Bouchard Lab (McGill University) were conducted. These included CNDs that were treated with Blebbistatin (an actomyosin inhibitor) as well as those that were not. Inhibition of actomyosin affected cell volume (increasing it by 32%), duct architecture (decreasing the CND and lumen radii) and enhanced apical extrusion, which cause an elongation of the CND. We adapted our in vivo framework to ex vivo conditions to model simultaneously the elongation of the CND due to Blebbistatin treatment and the shortening of the CND due to non-professional efferocytosis and cellular extrusion. Using this new model, we generated results showing that even when actomyosin is inhibited, shrinkage is still happening in the CND primarily through non-professional efferocytosis but also through apical extrusion. Even though the overall shrinkage of the CND is not as efficient as in the ex vivo Control CND, this suggests that the motor force of the CND shrinkage (non-professional efferocytosis) can work in the absence of actomyosin and that actomyosin is crucial to achieve the amount of shrinkage necessary during normal development.

This study thus provided spatiotemporal insights into the dynamics of the CND elimination and answered fundamental questions that cannot be tackled experimentally ; that include

1. quantifying
    (a) the digestion time of non-professional efferocytosis,
    (b) the timeline of the different stages of non-professional efferocytosis, and
    (c) the contribution of each component of the system to the CND shrinkage over time;
2. determining the efficiency of the CND shrinkage in the absence of actomyosin;
3. identifying efferocytosis as a key component responsible for this shrinkage over time.

More generally, our study suggests a mechanism for how cellular rearrangement could occur during embryonic development. The predictions made by our model are hard or even impossible to verify experimentally. Determining the timeline of non-professional efferocytosis in vivo is not doable because the CND can only be observed at given time points. As explained in Section 2.3.3, inhibiting certain cellular pathways to isolate the effect of some specific components is also hard because it would require cell culture experiments using different cell types with conditions for cells to grow outside the embryos that are very different from those used in vivo and control conditions highlighted in this study. This, as a result, would make the model not applicable to such culture conditions. Furthermore, it is important to emphasize here that the multiscale model used here was meant to deepen our understanding of this system in a manner similar to many other mathematical modeling studies done in this field.

4.3 Limitations and Future directions

A primary limitation in our study is the experimental data that defined the model framework. Indeed, this framework was purely based on experimental data coming from only two time points (E11.5 and E12.5). The length was averaged over 25 CNDs for both time points but the stationary distribution and apoptotic gradient were averaged over just three and five different embryos at E11.5 an E12.5, respectively. This limited data might moderately affect the accuracy of the quantitative predictions made by the model (e.g. digestion time and the dwell times in each stage of the efferocytosis) but should not affect too much our qualitative predictions (e.g. dissecting the main components of the CND shrinkage). We assumed instantaneous engulfment for both in-vivo and ex-vivo models. However, it is possible for Blebbistatin to slow down the engulfment process; since we had no significant experimental data to support this, we could not incorporate such effects in the model. This thus may impact the quantitative accuracy of our results but since the engulfment process is orders of magnitude faster than the other processes, it should not discredit our qualitative predictions (efficiency of the shrinkage in the absence of actomyosin through efferocytosis).

As mentioned before, one of the specificity of this mathematical model is that it was solved completely analytically. The advantage of producing analytical expressions is that they can be used to conduct analysis on the system that are otherwise not possible to perform. A shortcoming of this approach, however, is that the complexity of the involved differential equations is relatively limited because otherwise it would not be solvable analytically. We encountered this issue when we derived the PDE model for the Blebbi-treated CND (taking into account elongation and shortening of the CND); with such model formulation it was not possible to solve the model analytically on Mathematica. To implement the PDE model of Blebbi-treated CND, one needs to parameterize the model using fitting techniques such Markov Chain Monte Carlo methods. It would also be interesting to see if the results obtained analytically match with the ones obtained numerically. Discrepancies between the two models would then raise some interesting questions about our modeling of the CND elimination. Solving the model numerically could also allow us to investigate how the fluidity of the epithelial layer accounts for the shortening of the CND. The advection equation in our model considers the CND as a flux of cells without any phase transition. However, cell jamming within the CND can occur and generate a phase transition between liquid to solid states [46] which implies that the viscoelastic properties of the CND should be considered. Another limitation of our model is that we approximated the CND as a 1-D structure whereas the CND is a 3-D tissue enclosed between an outer cylinder and an inner cylinder (as explained in the Introduction). This geometrical aspect of the system could be further incorporated into the model in a more precise manner. Finally, our model does not take into account Phagocytes availability when modeling non-professional efferocytosis. In the caudal regions of the CND, where there are a lot of apoptosis, it is likely that an apoptotic body is surrounded by Phagocytes and needs to move in the CND before finding an available Normal cell to engulf it. The time required to find this available Normal cell could be an important factor in the model. Now that we already quantified the cellular interactions dynamics of the CND, one could incorporate these results into a simpler submodel for cellular interactions and couple it to a more elaborate 3-D model similar to those vertex models of epithelial morphogenesis previously developed in [36]. Such a comprehensive model represents the next step in our modeling effort of the CND to explore its spatiotemporal dynamics in a more biophysically accurate way.

Bibliography

[1] Scott, G., 2003, *The Epidermis and the Origin of Cutaneous Structures*, Developmental Biology. Sinauer Associates.

[2] Sadler, T. W., 2010, *Langman's Medical Embryology, 11th edition.*, Lippincott Williams Wilkins

[3] Scott, G., 2010, *Developmental biology, 9th edition.*, USA: Sinauer Associates.

[4] Dudek, R. W., 2009, *High-yield. Embryology, 4th edition*, Lippincott Williams Wilkins

[5] Kumar, R. , 2008, *Textbook of human embryology*, I.K. International.

[6] Mackie GG, Stephens FD, 1975, *Duplex kidneys: a correlation of renal dysplasia with position of the ureteral orifice.*, J Urol, 114:274–280.

[7] C. Mendelsohn., 2009, *Using mouse models to understand normal and abnormal urogenital tract development*, Organogenesis, 5(1):306-14.

[8] K. Stewart M. Bouchard, 2011, *Kidney and urinary tract development: an apoptotic balancing act.*, Pediatr Nephrol, 26:1419–1425.

[9] Stewart, K., and Bouchard, M. , 2014b *Coordinated cell behaviours in early urogenital system morphogenesis*, Seminars in cell developmental biology 36, 13-20.

[10] Batourina, E., Tsai, S., Lambert, S., Sprenkle, P., Viana, R., Dutta, S. et al. , 2005 *Apoptosis induced by vitamin A signaling is crucial for connecting the ureters to the bladder*, Nature Genetics 37, 1082.

[11] Batourina, E., Choi, C., Paragas, N., Bello, N., Hensle, T., Costantini, F.D., Schuchardt, A., Bacallao, R.L., and Mendelsohn, C.L., 2002 *Distal ureter morphogenesis depends on epithelial cell remodeling mediated by vitamin A and Ret*, Nature genetics 32, 109-115.

[12] Kim, S.T., Ahn, S.Y., Swat, W., and Miner, J.H., 2014 *DLG1 influences distal ureter maturation via a non-epithelial cell autonomous mechanism involving reduced retinoic acid signaling, Ret expression, and apoptosis*, Developmental biology 390, 160-169.

[13] Peuckert, C., Aresh, B., Holenya, P., Adams, D., Sreedharan, S., Porthin, A., Andersson, L., Pettersson, H., Wolfl, S., Klein, R., et al., 2016 *Multimodal Eph/Ephrin signaling controls several phases of urogenital development*, Kidney international 90, 373-388.

[14] Roux, M., Bouchard, M., and Kmita, M., 2019 *Multifaceted Hoxa13 function in urogenital development underlies the Hand-Foot-Genital Syndrome* , Human molecular genetics 28, 1671-1681.

[15] Uetani, N., and Bouchard, M., 2009 *Plumbing in the embryo: developmental defects of the urinary tracts*, Clin Genet 75, 307-317.

[16] Stewart, K., Tang, Y. C., Shafer, M. E. R., Graham-Paquin, A.-L., and Bouchard, M. , 2017 *Modulation of apoptotic response by LAR family phosphatases–cIAP1 signaling during urinary tract morphogenesis*,Proceedings of the National Academy of Sciences 114, E9016-E9025.

[17] Yosypiv, I.V., 2012 *Congenital anomalies of the kidney and urinary tract: A genetic disorder?*,In International Journal of Nephrology.

[18] Penberthy, Kristen K., Ignacio J. Juncadella, and Kodi S. Ravichandran , 2014 *Apoptosis and Engulfment by Bronchial Epithelial Cells. Implications for Allergic Airway Inflammation*,Annals of the American Thoracic Society 11.Supplement 5: S259-S262.

[19] Stanford, Jamie C., et al , 2014 *Efferocytosis produces a prometastatic landscape during postpartum mammary gland involution*,The Journal of clinical investigation 124.11: 4737.

[20] Jacobson, M. D., Weil, M., Raff, M. C., 1997, *Programmed cell death in animal development*, Cell, 88(3), 347-354.

[21] Shklover, J., Levy-Adam, F., and Kurant, E., 2015 *Apoptotic Cell Clearance in Development*, Current Topics in Developmental Biology (Steller, H., Ed.), pp 297-334, Academic Press., 924-935.

[22] Arandjelovic, S., and Ravichandran, K. S. , 2015 *Phagocytosis of apoptotic cells in homeostasis*, Current Topics in Developmental Biology (Steller, H., Ed.), Nature immunology 16, 907-917.

[23] He, L., Wang, X., Tang, H.L., and Montell, D.J., 2010 *Tissue elongation requires oscillating contractions of a basal actomyosin network*, Nature cell biology 12, 1133-1142.

[24] Heisenberg, C.P., and Bellaiche, Y., 2013 *Forces in tissue morphogenesis and patterning*, Cell 153, 948-962.

[25] Keller, R., Shook, D., and Skoglund, P., 2008 *The forces that shape embryos: physical aspects of convergent extension by cell intercalation*, Phys Biol 5, 015007.

[26] Murrell, M., Oakes, P.W., Lenz, M., and Gardel, M.L., 2015 *Forcing cells into shape: the mechanics of actomyosin contractility*, Nature reviews Molecular cell biology 16, 486-498.

[27] Petridou, N.I., and Heisenberg, C.P., 2019 *Tissue rheology in embryonic organization*, The EMBO journal 38, e102497.

[28] Sadati, M., Taheri Qazvini, N., Krishnan, R., Park, C.Y., and Fredberg, J.J., 2013 *Collective migration and cell jamming. Differentiation*, Research in biological diversity 86, 121-125.

[29] Yang, X., Bi, D., Czajkowski, M., Merkel, M., Manning, M.L., and Marchetti, M.C., 2017 *Correlating cell shape and cellular stress in motile confluent tissues*, Proceedings of the National Academy of Sciences of the United States of America 114, 12663-12668.

[30] Sun, Z., and Toyama, Y. , 2018 *Three-dimensional forces beyond actomyosin contraction: lessons from fly epithelial deformation*, Curr Opin Genet Dev 51, 96-102

[31] Uetani, N., Bertozzi, K., Chagnon, M. J., Hendriks, W., Tremblay, M. L., Bouchard, M., 2009 *Maturation of ureter-bladder connection in mice is controlled by LAR family receptor protein tyrosine phosphatases*, The Journal of clinical investigation, 119(119 (4)), 924-935.

[32] Tran CL, Jones AD, Donaldson K, 1995 *Mathematical model of phagocytosis and inflammation after the inhalation of quartz at different concentrations*, Scand J Work Environ Health 1995;21(2):50-54

[33] Athanasius F.M. Marée, M. Komba, C. Dyckb, M Łabecki, D. T. Finegood, L. Edelstein-Keshet, 2004 *Quantifying macrophage defects in type 1 diabetes*, Journal of Theoretical Biology 233 (2005) 533–551

[34] Athanasius F.M. Marée, R. Kublik, D. T. Finegood, L. Edelstein-Keshet, 2006 *Modelling the onset of Type 1 diabetes: can impaired macrophage phagocytosis make the difference between health and disease?*, Phil. Trans. R. Soc. A (2006) 364, 1267–1282

[35] Athanasius F.M. Marée, M. Komba, D. T. Finegood, L. Edelstein-Keshet, 2007 *A quantitative comparison of rates of phagocytosis and digestion of apoptotic cells by macrophages from normal (BALB/c) and diabetes-prone (NOD) mice*, J Appl Physiol 104: 157–169, 2008.

[36] A. G. Fletcher, M. Osterfield, R. E. Baker, and S. Y. Shvartsman, 2014 *Vertex models of epithelial morphogenesis*, Biophysical journal 106 (11), 2291-2304

[37] Trudeau, J.D., Dutz, J.P., Arany, E., Hill, D.J., Fieldus, W.E., Finegood, D.T., 2000. *Neonatal beta-cell apoptosis: a trigger for autoimmune diabetes?*, Diabetes 49, 1–7

[38] Mathis, D., Vence, L., Benoist, C., 2001. *β-Cell death during progression to diabetes.*, Nature 414 (6865), 792–798.

[39] Georgiou, H.M., Constantinou, D., Mandel, T.E., 1995. *Prevention of autoimmunity in non-obese diabetic (NOD) mice by neonatal transfer of allogeneic thymic macrophages*, Autoimmunity 21, 89–97.

[40] Shimada, A., Takei, I., Maruyama, T., Kasuga, A., Kasatani, T., Watanabe, K., Asaba, Y., Ishii, T., Tadakuma, T., Habu, S., et al., 1994. *Acceleration of diabetes in young NOD mice with peritoneal macrophages* Diabetes Res. Clin. Practice 24, 69–76.

[41] Alleva, D.G., Pavlovich, R.P., Grant, C., Kaser, S.B., Beller, D.I., 2000. *Aberrant macrophage cytokine production is a conserved feature among autoimmune-prone mouse strains: elevated inter- leukin (IL)-12 and an imbalance in tumor necrosis factor-alpha and IL-10 define a unique cytokine profile in macrophages from young nonobese diabetic mice.* Diabetes 49, 1106–1115.

[42] Jun, H.-S., Yoon, C.-S., Zbytnuik, L., Van Rooijen, N., Yoon, J.-W., 1999. *The role of macrophages in T cell-mediated autoimmune diabetes in nonobese diabetic mice.* J. Exp. Med. 189, 347–358.

[43] O'Brien, B.A., Huang, Y., Geng, X., Dutz, J.P., Finegood, D.T., 2002. *Phagocytosis of apoptotic cells by macrophages from NOD mice is reduced.* Diabetes 51, 2481–2488

[44] Gammack, D., Doering, C.R., Kirschner, D.E., 2004. *Macrophage response to Mycobacterium tuberculosis infection.* J. Math. Biol. 48, 218–242.

[45] Tran, C.L., Jones, A.D., Donaldson, K., 1995. *Mathematical model of phagocytosis and inflammation after the inhalation of quartz at different concentrations.* Scand. J. Work Environ. Health 21, 50–54.

[46] Dapeng Bi et al, 2015. *A density-independent rigidity transition in biological tissues.* Nature Physics. 11, pages1074–1079 (2015).

[47] M.Sandahl, D. M. Hunter, K. E. Strunk, H S. Earp, R. S Cook 2010. *Epithelial cell-directed efferocytosis in the post-partum mammary gland is necessary for tissue homeostasis and future lactation* BMC Dev Biol. 2010; 10: 122

[48] Diabetes Systems Biology, *Quantitative methods for understanding beta-cell dynamics and function.* A. Khadra, H. Jamaleddine and al., Institute of Physics Publishing, 2020

[49] Jamaleddine, H., and Khadra, 2020 A *Immune-cell dynamics in type 1 diabetes.* Diabetes Systems Biology.

[50] A. Khadra, P. Santamaria and L. Edelstein-Keshet. *The Role of Low Avidity T Cells in the Protection Against Type 1 Diabetes: A Modeling Investigation.* Journal of Theoretical Biology, 256, 126-141, 2009.

[51] A. Khadra, P. Santamaria and L. Edelstein-Keshet. *The Pathogenicity of Self-Antigen Decreases at High Levels of Autoantigenicity: A Computational Approach.* International Immunology, 22, 571-582, 2010.

[52] A. Khadra, S. Tsai, P. Santamaria and L. Edelstein-Keshet. *On How Monospecific Memory-Like Autoregulatory CD8+ T Cells Can Blunt Diabetogenic Autoimmunity: A Computational Approach.* Journal of Immunology, 185, 5962-5972, 2010.

[53] A. Khadra, M. Pietropaolo, G.T. Nepom and A. Sherman. *Investigating the Role of T-Cell Avidity and Killing Efficacy in Relation to Type 1 Diabetes Prediction.* PLoS ONE, 6, e14796, 2011.

[54] M. Jaberi-Douraki, M. Pietropaolo and A. Khadra. *Predictive Models of Type 1 Diabetes Progression: Understanding T-Cell Cycles and their Implications on Autoantibody Release.* PLoS ONE, 9, e93326, 2014.

[55] M. Jaberi-Douraki, S.W. Liu, M. Pietropaolo and A. Khadra. *Autoimmune Responses in T1DM: Quantitative Methods to Understand Onset, Progression and Prevention of Disease.* Pediatric Diabetes, 15, 162-174, 2014.

[56] M. Jaberi-Douraki, S. Schnell, M. Pietropaolo and A. Khadra. *Unraveling the Contribution of Pancreatic Beta-Cell Suicide in Autoimmune Type 1 Diabetes.* Journal of Theoretical Biology, 375, 77-87, 2015.

[57] A. Khadra and S. Schnell. *Development, Growth and Maintenance of Beta-Cell Mass: Models are also Part of the Story.* Molecular Aspects of Medicine, Special Issue: Recent Advances in Pancreatic Beta Cell Failure and Diabetes, 42, 42-60, 2015.

[58] M. Jaberi-Douraki, M. Pietropaolo and A. Khadra. *Continuum Model of T-Cell Avidity: Understanding Autoreactive and Regulatory T-Cell Responses in Type 1 Diabetes.* Journal of Theoretical Biology, 383, 93-105, 2015.

[59] Weliky, M., and G. Oster, 1990. *The mechanical basis of cell rearrangement. I. Epithelial morphogenesis during Fundulus epiboly.* Development. 109:373–386.

[60] Edelstein-Keshet, Leah, 2005. *Edelstein-Keshet, Leah. Mathematical models in biology.* Society for Industrial and Applied Mathematics. 109:373–386.

[61] Weliky, M., S. Minsuk, G. Oster and al, 1991. *Notochord morphogenesis in Xenopus laevis: simulation of cell behavior underlying tissue conver- gence and extension.* Development. 113:1231–1244.

[62] T. J. van Ham, D. Kokel, R. T. Peterson. *Apoptotic Cells Are Cleared by Directional Migration and elmo1- Dependent Macrophage Engulfment.* Current Biology, Volume 22, Issue 9, 8 May 2012, Pages 830-836.

[63] D. A. D. Munro, and al., 2019 *Macrophages restrict the nephrogenic field and promote endothelial connections during kidney development* Cell, volume 107, issue 1, eLife 8

[64] T. L. Gumienny, E. Brugnera, K.S Ravichandran and al. *CED-12/ELMO, a Novel Member of the CrkII/Dock180/Rac Pathway, Is Required for Phagocytosis and Cell Migration.* Cell, volume 107, issue 1, P27-41, October 05, 2001.

Appendix: heatmaps of spatiotemporal variables and tables of parameters

For each of WT1, and Control CND ex vivo, we plot the heatmaps of K_A, v and K_{BX} with respect to time on (the vertical axis) and position along the CND (on the horizontal axis) and provide the values of the rate constants K_D K_{EI}, K_{LI}, K_G and K_S (and K_{AX} for the IBMs). The values of f_n and f_e are given by 0.886 and 0.20, respectively. The value of f_{ax} varies between the different time steps when applying the IBM; it is equal to 0.998, 0.996, 0.985, 0.977 and 0.958 for the steps between $t = 0$ h and $t = 3$ h (labeled IBM1), between $t = 3$ h and $t = 6$ h (labeled IBM2), between $t = 6$ h and $t = 12$ h (labeled IBM3), between $t = 12$ h and $t = 24$ h (labeled IBM4) and between $t = 24$ h and $t = 48$ h (labeled IBM5), respectively.

Computations of the "Duration of each process per cell" in Tables 6 and 7

Given K_D, K_{EI}, K_{LI}, K_G, and K_S, one can compute the duration of each process associated with these rate constants (i.e., the dwell time spent in each stage of the Markov models of Figures 2.3 and 2.4). Because the transitions of the Markov model are irreversible, these durations are given by $1/K_D$, $1/K_{EI}$, $1/K_{LI}$, $1/K_G$ and $1/K_S$, respectively.

Computations of the "Duration of each process per cell" in Tables 8, 9, 10, 11 and 12.

For each IBMi ($i = 1, 2, 3, 4, 5$), the rate constants K_D, K_{EI}, K_{LI}, K_G, and K_S, as before, define the duration of each process associated with them as follows: γ_i/K_D, γ_i/K_{EI}, γ_i/K_{LI}, γ_i/K_G and $1/K_S$ days, respectively. For each IBMi, the value of γ_i is given in Section 3.2.3.

Clarification on the heatmaps of IBM1, IBM2 IBM3, IBM4 and IBM5.

For each IBMi ($i = 1, 2, 3, 4, 5$), the length of the CND shrinks from the elongated length of L_{ei} at $t = 0$ to the length $B(L_{e_i})$ at $t = t_i - t_{i-1}$ (see notation in Section 3.2.3).

Varying proliferation

Let WT1-P5.3 and WT1-P17.5 denote the WT1 model with 5.3% ($f_n = 0.947$) and 17.5% ($f_n = 0.825$) proliferation.

Table 4: Values of K_D in WT1, WT1-P5.3 and WT1-P17.5 models.

Model	WT1-P5.3	WT1	WT1-P17.5
K_D $(days^{-1})$	2.50	2.70	2.91

Varying apoptotic gradient

Let WT1-Upregulated and WT1-Downregulated denote the WT1 model with the apoptotic gradient shown in Figure 2.9 shifted up and down by 3.5%, respectively.

Table 5: Values of K_D in WT1, WT1-Upregulated and WT1-Downregulated models.

Model	WT1-Upregulated	WT1	WT1-Downregulated
K_D $(days^{-1})$	2.43	2.70	3.04

Table 6: List of rate constants and their estimated values for WT1.

Symbol	Description	Value	Unit	Duration of associated process per cell
K_D	Digestion rate	2.70	day^{-1}	8.89 hours
K_{EI}	Early internalization rate	32.5	day^{-1}	44.3 minutes
K_{LI}	Late internalization rate	5.12	day^{-1}	4.69 hours
K_G	Degradation rate	6.94	day^{-1}	3.46 hours
K_S	Proliferation rate	24/18	day^{-1}	18 hours

Table 7: List of rate constants and their estimated values for Control.

Symbol	Description	Value	Unit	Duration of associated process per cell
K_D	Digestion rate	2.70	day^{-1}	8.89 hours
K_{EI}	Early internalization rate	32.5	day^{-1}	44.3 minutes
K_{LI}	Late internalization rate	5.12	day^{-1}	4.69 hours
K_G	Degradation rate	6.94	day^{-1}	3.46 hours
K_S	Proliferation rate	24/18	day^{-1}	18 hours

Table 8: List of rate constants and their estimated values for IBM1.

Symbol	Description	Value	Unit	Duration of associated process per cell
K_D	Digestion rate	2.74	day^{-1}	8.89 hours
K_{EI}	Early internalization rate	32.9	day^{-1}	44.3 minutes
K_{LI}	Late internalization rate	5.19	day^{-1}	4.69 hours
K_G	Degradation rate	7.03	day^{-1}	3.46 hours
K_S	Proliferation rate	24/18	day^{-1}	18 hours
K_{AX}	Apical extrusion rate	7.79	day^{-1}	3.08 hours

Table 9: List of rate constants and their estimated values for IBM2.

Symbol	Description	Value	Unit	Duration of associated process per cell
K_D	Digestion rate	2.77	day^{-1}	8.89 hours
K_{EI}	Early internalization rate	33.3	day^{-1}	44.3 minutes
K_{LI}	Late internalization rate	5.25	day^{-1}	4.69 hours
K_G	Degradation rate	7.12	day^{-1}	3.46 hours
K_S	Proliferation rate	24/18	day^{-1}	18 hours
K_{AX}	Apical extrusion rate	7.79	day^{-1}	3.58 hours

Table 10: List of rate constants and their estimated values for IBM3.

Symbol	Description	Value	Unit	Duration of associated process per cell
K_D	Digestion rate	2.99	day^{-1}	8.89 hours
K_{EI}	Early internalization rate	35.9	day^{-1}	44.3 minutes
K_{LI}	Late internalization rate	5.66	day^{-1}	4.69 hours
K_G	Degradation rate	7.67	day^{-1}	3.46 hours
K_S	Proliferation rate	24/18	day^{-1}	18 hours
K_{AX}	Apical extrusion rate	7.79	day^{-1}	3.58 hours

Table 11: List of rate constants and their estimated values for IBM4.

Symbol	Description	Value	Unit	Duration of associated process per cell
K_D	Digestion rate	3.15	day^{-1}	8.89 hours
K_{EI}	Early internalization rate	37.8	day^{-1}	44.3 minutes
K_{LI}	Late internalization rate	5.97	day^{-1}	4.69 hours
K_G	Degradation rate	8.09	day^{-1}	3.46 hours
K_S	Proliferation rate	24/18	day^{-1}	18 hours
K_{AX}	Apical extrusion rate	7.79	day^{-1}	3.58 hours

Table 12: List of rate constants and their estimated values for IBM5.

Symbol	Description	Value	Unit	Duration of associated process per cell
K_D	Digestion rate	3.57	day^{-1}	8.89 hours
K_{EI}	Early internalization rate	42.8	day^{-1}	44.3 minutes
K_{LI}	Late internalization rate	6.76	day^{-1}	4.69 hours
K_G	Degradation rate	9.16	day^{-1}	3.46 hours
K_S	Proliferation rate	24/18	day^{-1}	18 hours
K_{AX}	Apical extrusion rate	7.79	day^{-1}	3.58 hours

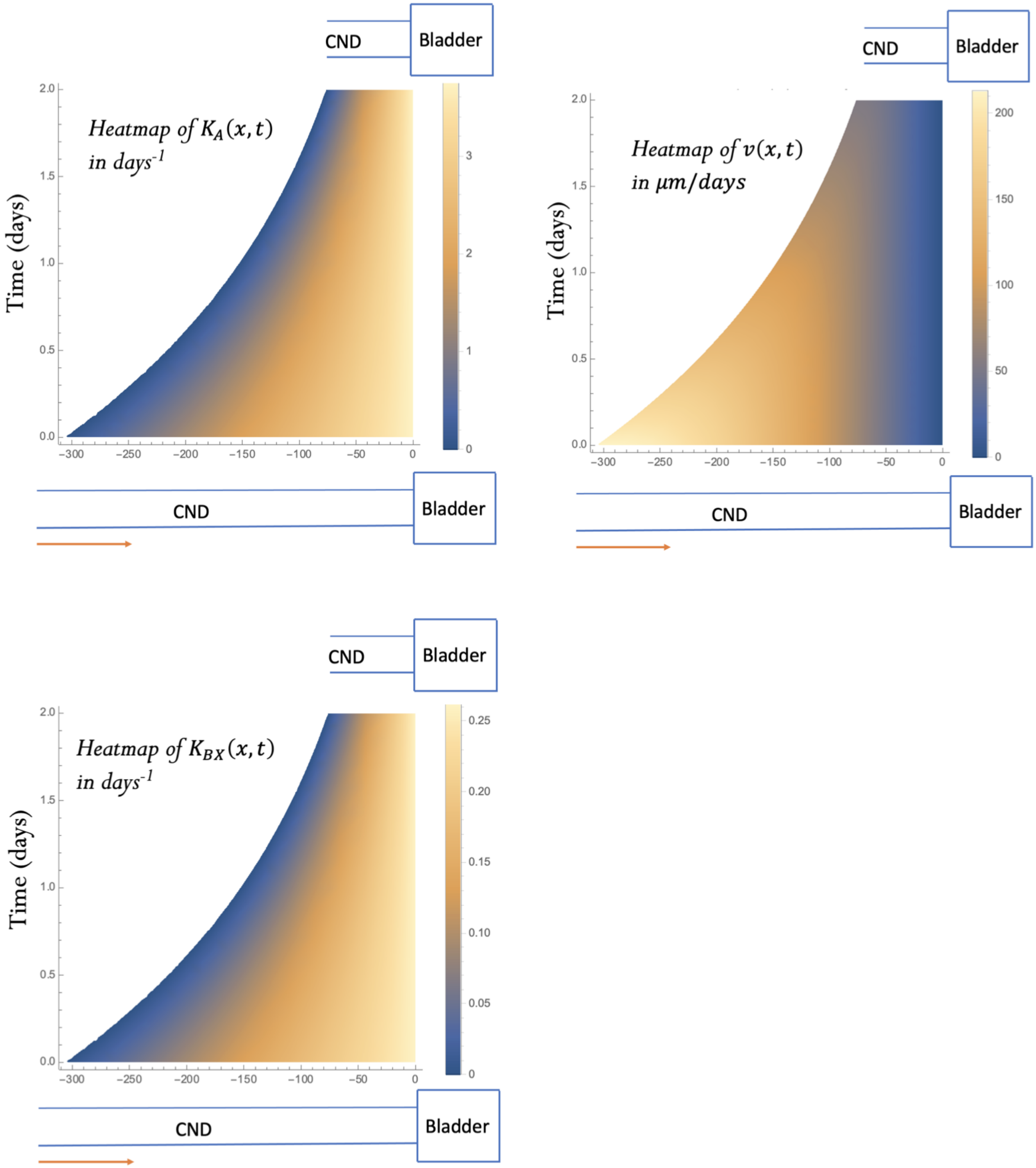

Figure 4.1: Heat maps of K_A, v and K_{BX} associated with WT1.

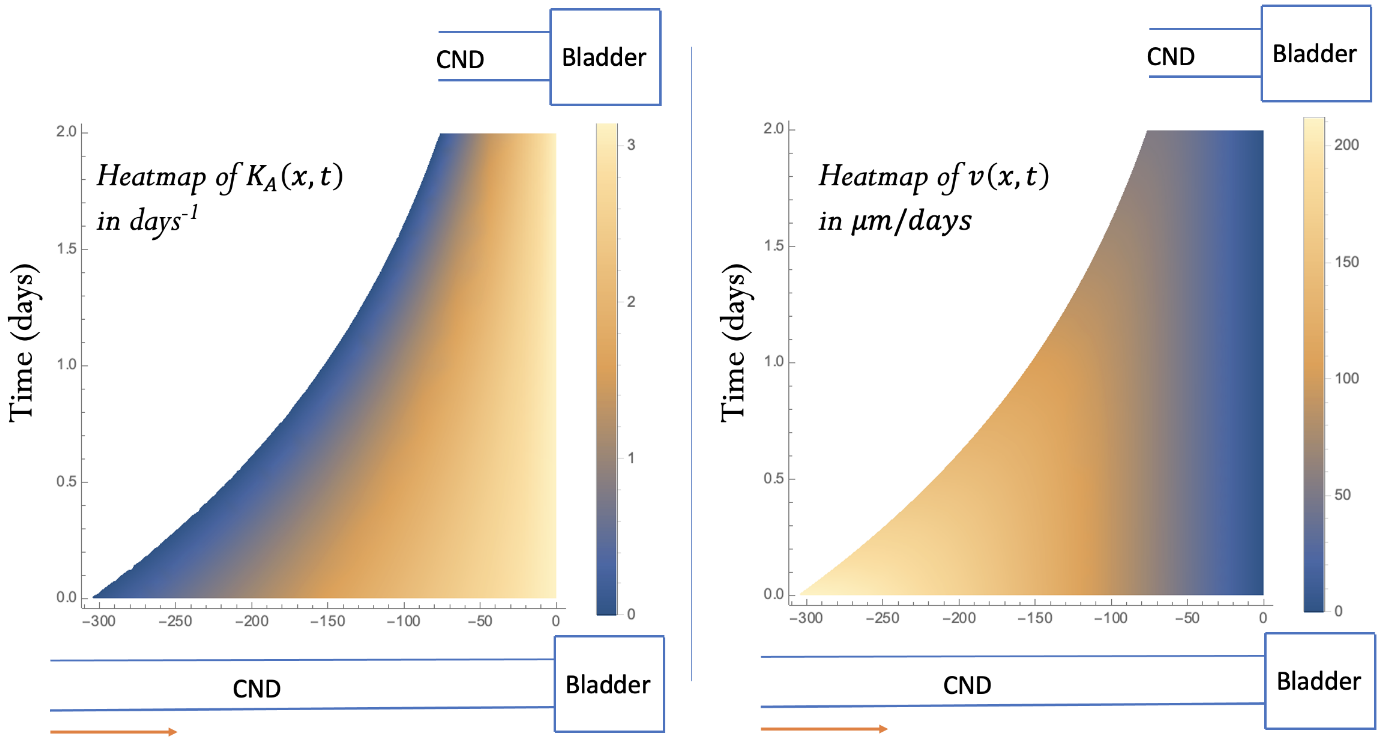

Figure 4.2: Heat maps of K_A and v associated with WT1-P5.3.

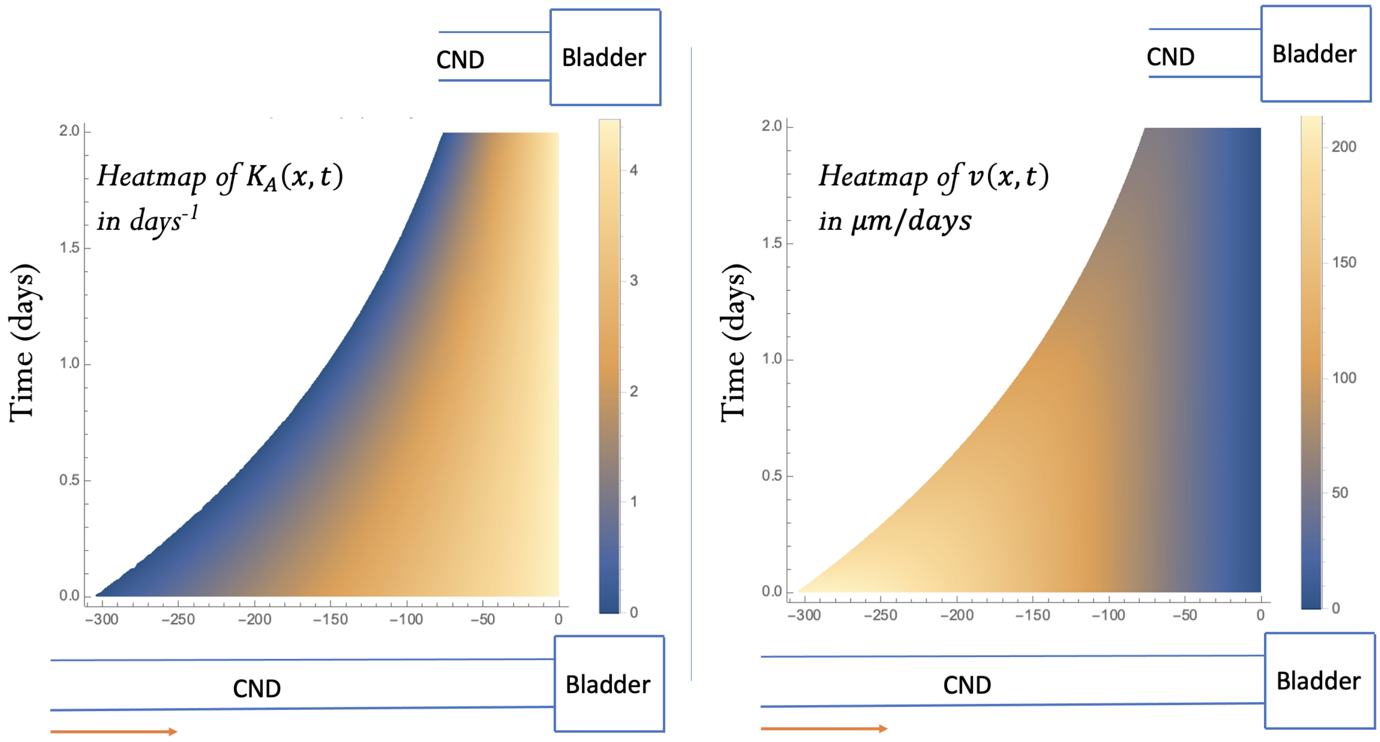

Figure 4.3: Heat maps of K_A and v associated with WT1-P17.5.

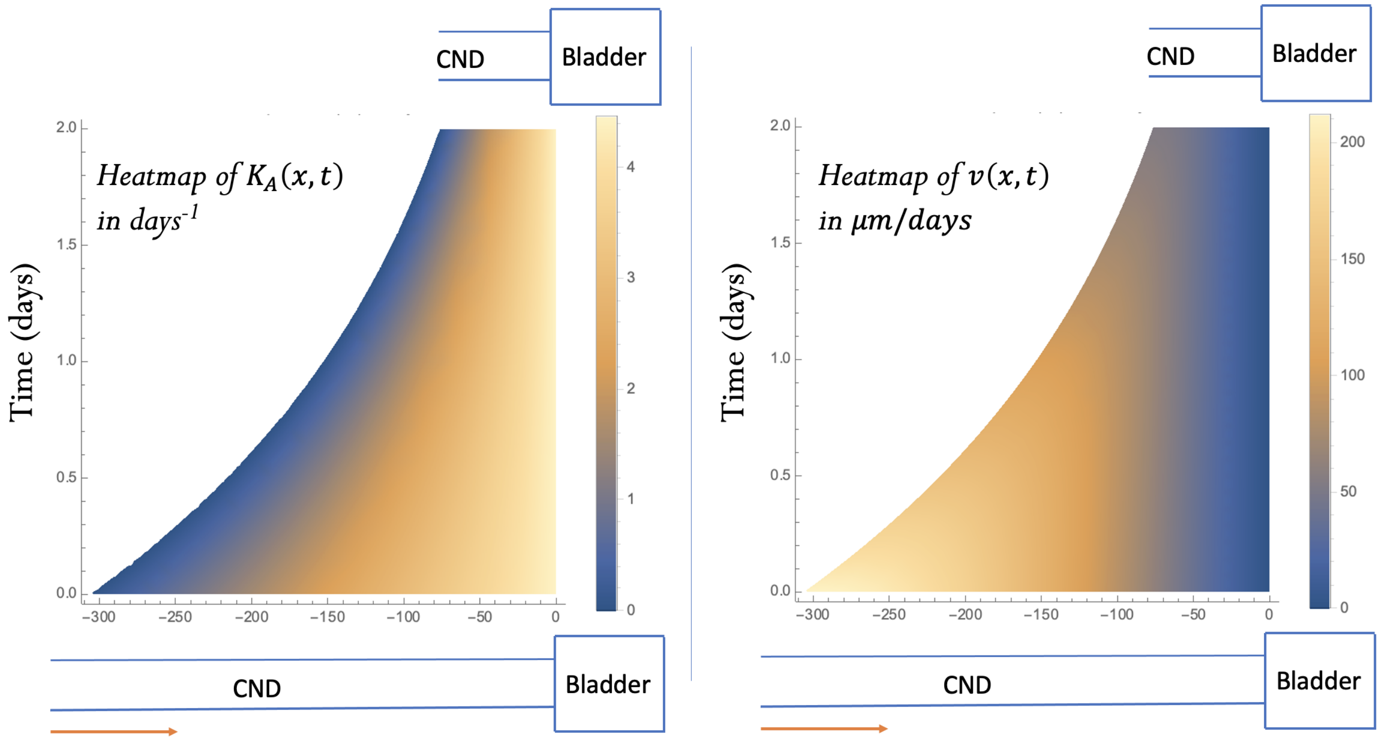

Figure 4.4: Heat maps of K_A and v associated with WT1-UpGrad.

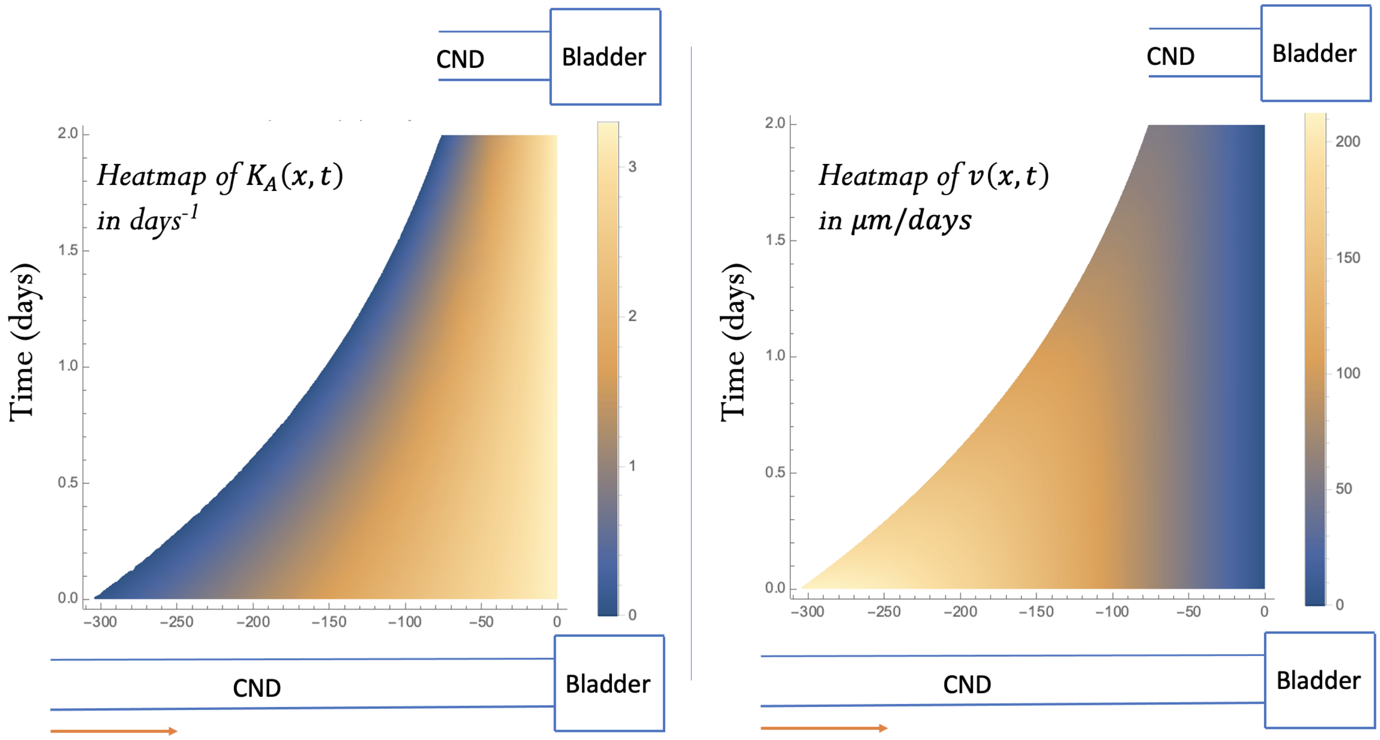

Figure 4.5: Heat maps of K_A and v associated with WT1-DownGrad.

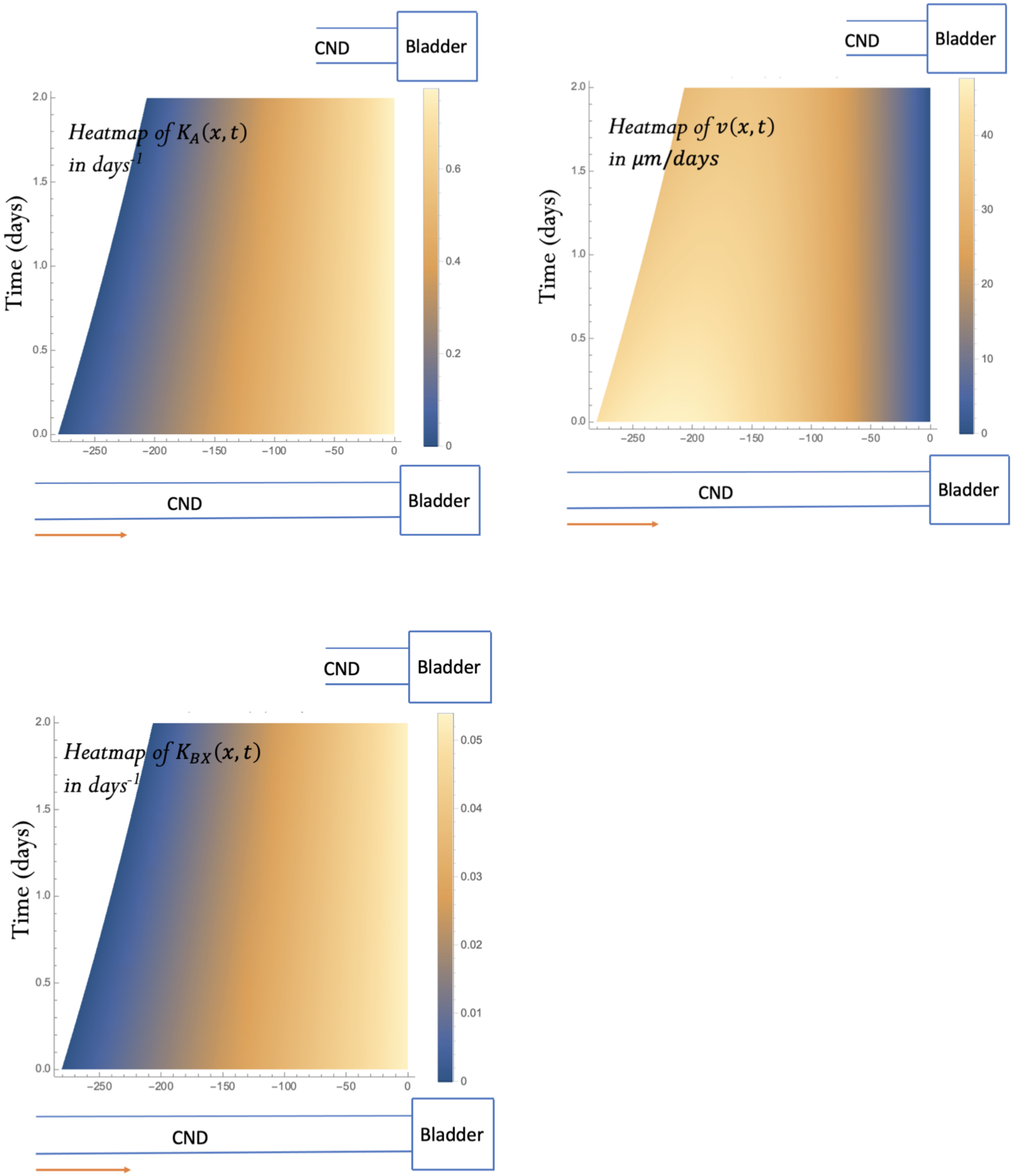

Figure 4.6: Heat maps of K_A, v and K_{BX} associated with Control.

$$
\begin{aligned}
&\Big(-3.60742\times 10^{11} + \mathrm{gf}\,\big(1.07229\times 10^{10} + \mathrm{gf}\,\big(-9.63121\times 10^{7} + 268\,930.\,\mathrm{gf}\big)\big) + \\
&\quad \mathrm{gb}\,\big(9.30833\times 10^{9} + \mathrm{gf}\,\big(-2.63975\times 10^{8} + \big(2.29258\times 10^{6} - 6212.14\,\mathrm{gf}\big)\,\mathrm{gf}\big)\big) + \\
&\quad \mathrm{gb}^{3}\,(202\,365. + \mathrm{gf}\,(-5338.85 + (43.4995 - 0.10992\,\mathrm{gf})\,\mathrm{gf})) + \\
&\quad \mathrm{gb}^{2}\,\big(-7.66748\times 10^{7} + \mathrm{gf}\,\big(2.09289\times 10^{6} + \mathrm{gf}\,(-17\,614.1 + 46.2256\,\mathrm{gf})\big)\big)\Big) \Big/ \\
&\Big(\mathrm{gf}\,\big(-6.17639\times 10^{9} + \big(1.47262\times 10^{8} - 782\,805.\,\mathrm{gf}\big)\,\mathrm{gf}\big) + \\
&\quad \mathrm{gb}^{2}\,\big(1.23042\times 10^{8} + \mathrm{gf}\,\big(-5.30142\times 10^{6} + (70\,499.1 - 287.699\,\mathrm{gf})\,\mathrm{gf}\big)\big) + \\
&\quad \mathrm{gb}^{3}\,(-589\,047. + \mathrm{gf}\,(21\,949.6 + \mathrm{gf}\,(-262.898 + 1.\,\mathrm{gf}))) + \\
&\quad \mathrm{gb}\,\big(-6.17639\times 10^{9} + \mathrm{gf}\,\big(3.69126\times 10^{8} + \mathrm{gf}\,\big(-5.8827\times 10^{6} + 26\,599.8\,\mathrm{gf}\big)\big)\big)\Big)
\end{aligned}
$$

Figure 4.7: The function $f(g_C, g_R)$ in 3.1

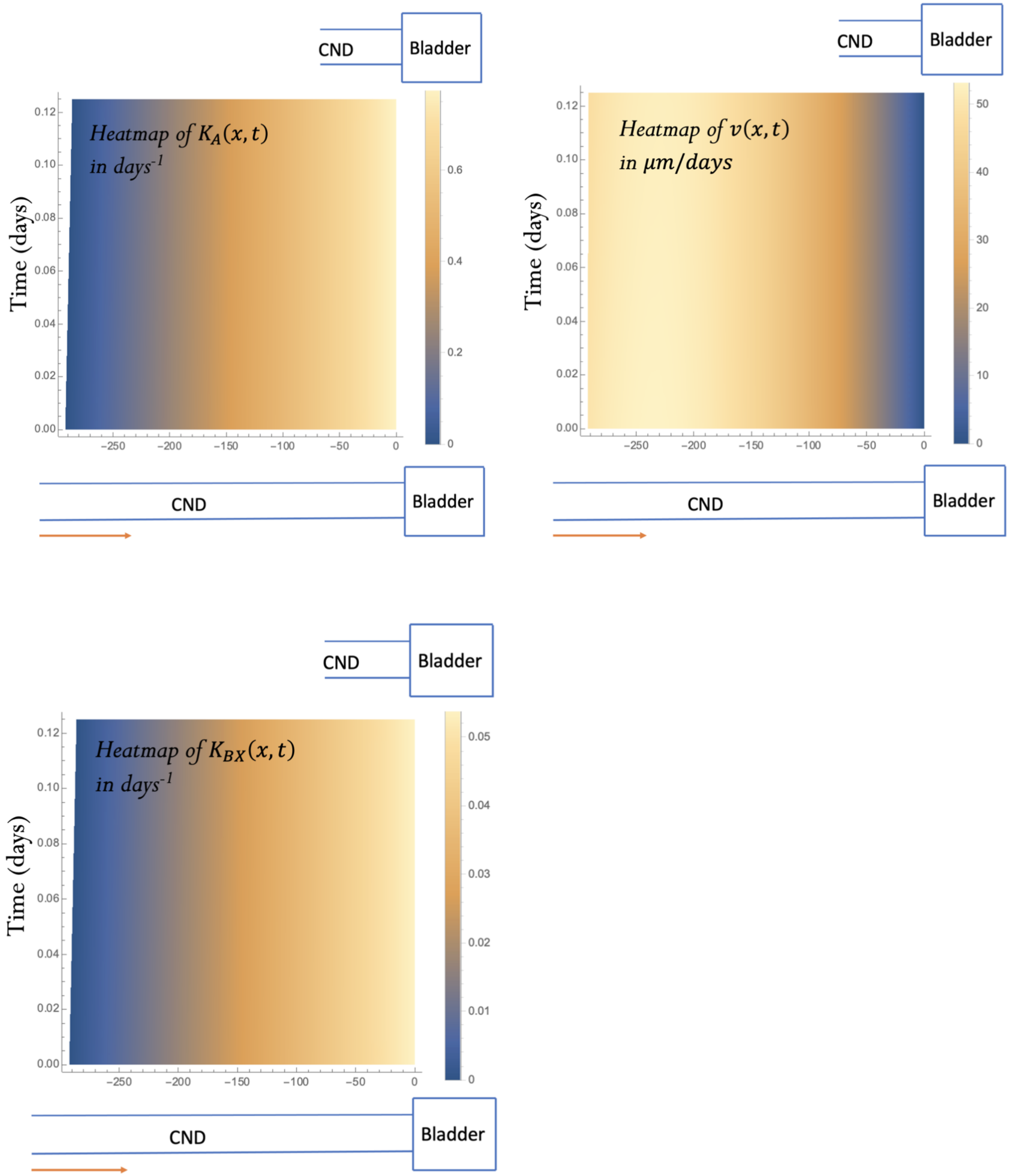

Figure 4.8: Heat maps of K_A, v and K_{BX} associated with IBM1.

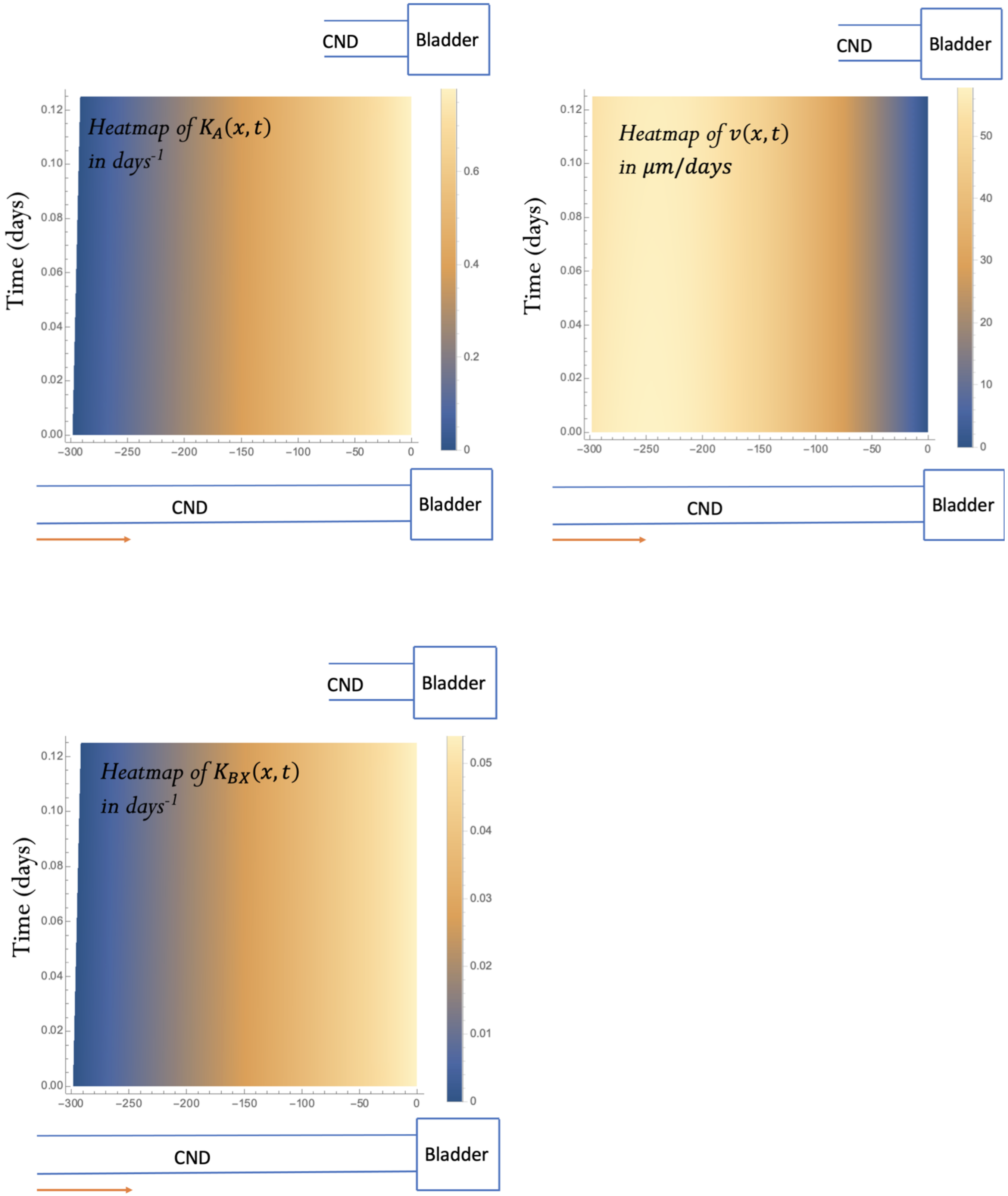

Figure 4.9: Heat maps of K_A, v and K_{BX} associated with IBM2.

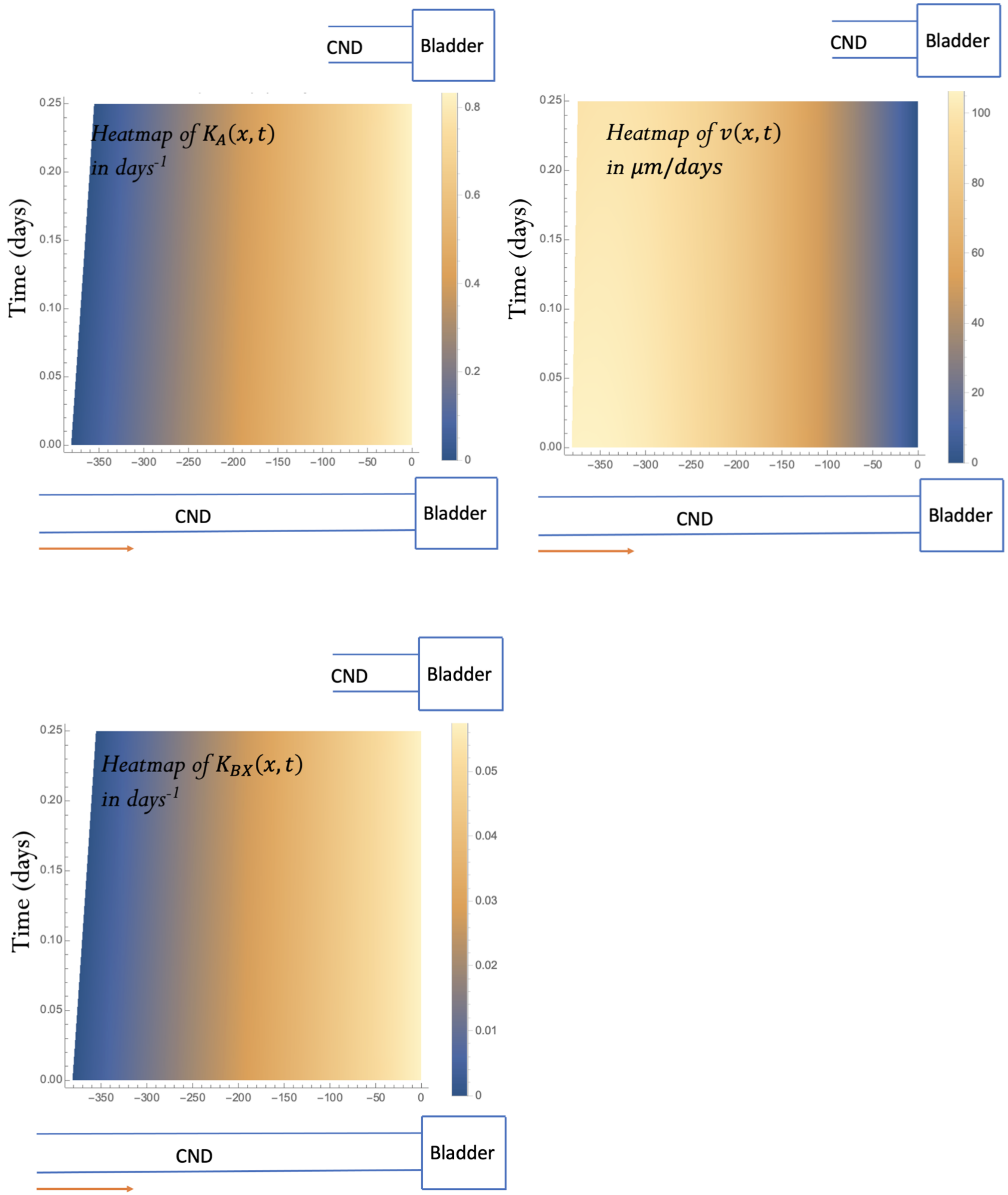

Figure 4.10: Heat maps of K_A, v and K_{BX} associated with IBM3.

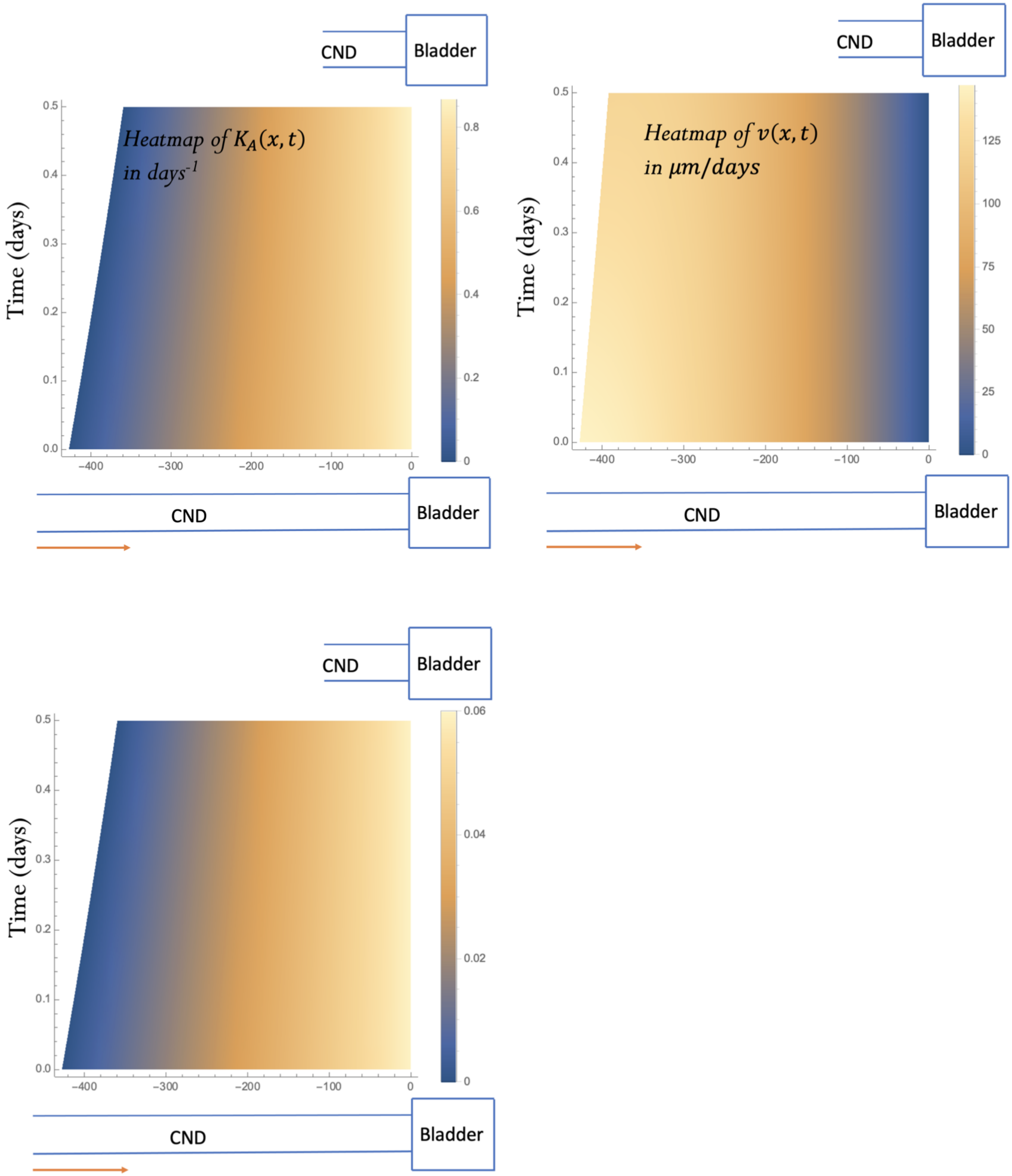

Figure 4.11: Heat maps of K_A, v and K_{BX} associated with IBM4.

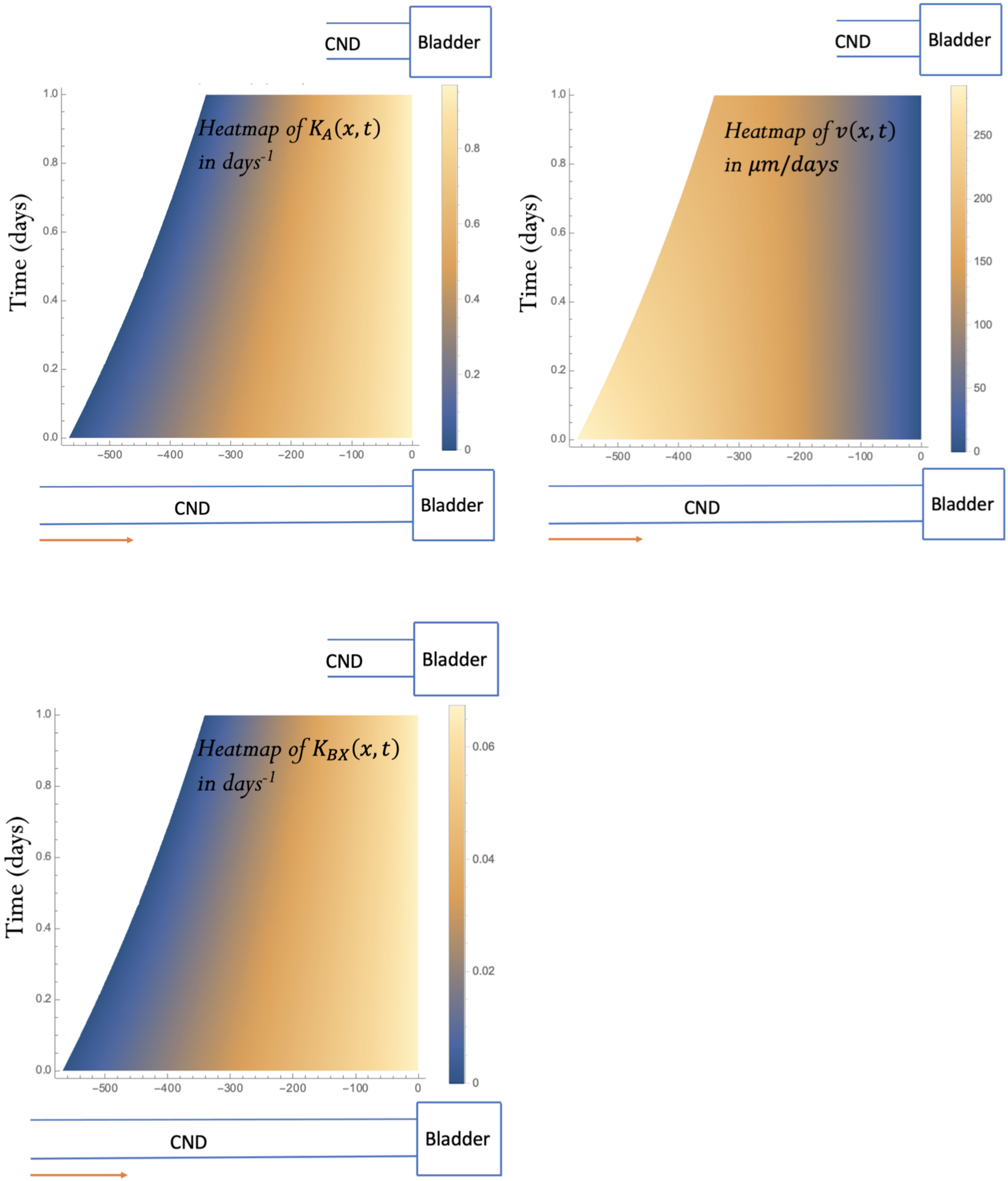

Figure 4.12: Heat maps of K_A, v and K_{BX} associated with IBM5.